



UNIVERSITÀ DEGLI STUDI “ROMA TRE”

DIPARTIMENTO DI MATEMATICA E FISICA
Scuola dottorale in Matematica e Fisica - XXXI Ciclo
Tesi di Dottorato in Fisica

***Investigation of GNSS scintillations under different
configurations of the magnetosphere-ionosphere
coupling***

A thesis submitted for the degree of
Doctor of Philosophy

Author

Giulia D'Angelo

Supervisor

Prof. Elena Pettinelli

Co-Supervisor

Dr. Lucilla Alfonsi

A. A. 2015 - 2017

INTRODUCTION

Problem description and motivation

Over the last two decades, interest in scintillation on trans-ionospheric L-band signals has grown, because of the considerable effects on the performance of the satellite communication and navigation (see, e.g., Fisher and Kunches, 2011; Board, 2008). Experimental evidence clearly shows that when a satellite signal, in a range of frequencies between 100 MHz and 4 GHz, crosses a delimited ionospheric region (in space and time) with an uneven electron density distribution (known as ionospheric irregularity), it is subjected to diffractive and refractive effects (Yeh and Liu, 1982; Kintner et al., 2007; Jayachandran et al., 2017). These effects produce amplitude and phase variations in the ground received signal (Basu et al., 1988; Aarons, 1982, 1997; Aarons and Basu, 1994), which are known as ionospheric scintillation, analogously to what is observed for the brightness of stars in the optical band.

In the case of Global Navigation Satellite Systems (GNSS), such as GPS, GLONASS and the nascent European GALILEO, scintillation may reduce the accuracy of the pseudorange and phase measurements. Consequently, the positioning errors increase and, in extreme cases, the service can become unavailable. In fact, during intense scintillation events, the signal power can drop below the threshold limit, the receiver loses lock to the satellite and GNSS positioning is not possible (see, e.g., Kintner et al., 2009). Therefore, scintillation events may affect the use of modern technology causing economic loss.

Since scintillations are due to both the presence and dynamics of plasma irregularities in the ionosphere, the understanding of the physical mechanisms that regulate the formation and dynamics of such irregularities is crucial to develop reliable prediction models and mitigation techniques to tackle the effect on GNSS-reliant services.

It is known that the formation and dynamics of ionospheric irregularities are closely linked to physical processes originating in the interplanetary medium (Tsunoda, 1988; Kelley, 1989; Fejer and Kelley, 1980; Hunsucker and Hargreaves, 2002). The formation and dynamics of plasma density irregularities in ionosphere are generally influenced by plasma circulation, which is directly controlled by the Interplanetary Magnetic Field (IMF) conditions (Baumjohann e Treumann, 1996). Such irregularities develop at all latitudes, especially in correspondence with maximum solar activity, although they are more frequent in both polar and equatorial regions. Here, the coupling between the IMF and the Earth's magnetic field can give rise to particle precipitation in the high latitude ionosphere and to penetration of solar wind electric field at low latitude ionosphere. These conditions favour development of irregularities (Aarons, 1982; Basu et al., 1988; Wernik et al., 2004; Spogli et al., 2013a). For this reason, the scientific community envisages the need to explain the cause-effect mechanisms that determine the passage from a certain IMF configuration to the ionospheric perturbations. Such necessity is even more urgent at high latitudes, where the presence of cusps and field-aligned currents directly exposes the ionosphere to variations of the solar wind. This configuration results in a strong sensitivity of the polar ionosphere to perturbation phenomena caused

by solar events, which result in complex and strongly variable plasma dynamics that may evolve in a wide variety of spatial and temporal dimensions (Fejer and Kelley, 1980; Tsunoda, 1988; Brekke, 2012).

In recent years, the investigation of the links between external drivers and GNSS scintillations has raised considerable interest in the space physics community. However, the identification of the physical properties of the solar wind-magnetosphere-ionosphere coupling has not yet reached the levels required to develop prediction models and mitigation techniques able to perform a safe support service (Jakowski et al., 2011; Fisher and Kunches, 2011). The physical mechanisms regulating such coupling show a high degree of complexity related to the high variability in the change of the geospace environment conditions including those on the Sun, in the interplanetary medium, and in the magnetosphere-ionosphere-thermosphere system. These collective, often violent, changes in the space environment around the Earth are referred to as “space weather” (Baker, 1998).

Research aims

The understanding of the physical mechanisms regulating the solar wind-magnetosphere-ionosphere coupling motivates the necessity for an original contribution to the current knowledge in the sector. Therefore, this work aims to achieve a broader understanding of the existing link between the external origin geomagnetic field perturbations and the ionospheric scintillations under strong disturbance conditions of the interplanetary medium. In particular, this work supports the acquisition of capabilities for predicting the effects of the perturbed ionosphere on technological systems (Singh et al., 2010; Nagatsuma et al., 2014) thus contributing to studies of “space weather”. Consequently, the topic choice has been motivated both by the need to contribute to the study of physical processes that regulate the highly-ionized upper atmosphere, and by an awareness that the technological systems sensitive to ionospheric changes may have a development only if supported by a deep knowledge of the geospace environment.

The high latitude ionosphere and especially the Antarctica, due to poor observations linked to the difficulty for installing and managing stations in remote areas, which are not easily accessible and sparsely populated, is still not yet deeply investigated (Sojka et al., 1993; Alfonsi et al., 2005; De Franceschi et al., 2006). The mid-latitude ionosphere, on the other hand, has been the subject of numerous studies that highlight its generally quiet nature, more easily modelled (Huang et al., 2005; Tsagouri et al., 2013). Finally, very dense and well-distributed global networks monitor some of the tropical and equatorial ionospheric regions. This allows a good knowledge of the ionospheric dynamics and physical mechanisms causing ionospheric perturbations that, however, are not easy to model (Aarons, 1982; Aarons, 1991; Aarons, 1993; Basu and Basu, 1985).

Starting from the 90s of the last century, many efforts were made to perform a multi-instrumental monitoring of the high-ionized atmosphere to study the ionospheric dynamics at different spatial and temporal scales. These, contributing to the Global Change and emerging space weather studies, allowed the development of empirical models able to explain, with good approximation, the long-term variations of the ionosphere (Rishbeth, 1990; Rishbeth and Roble, 1992, Bremer et al, 2004; Alfonsi et al., 2001; 2002). However, to date, the necessary knowledge to formulate a reliable forecasting of the short and medium-term ionospheric plasma variations has not yet been achieved.

This is particularly true for helio-geophysical disturbances (Lastovicka 2002; Mikhailov and Perrone, 2014; Prikryl et al., 2012, Sieradzki, 2015; Beniguel et al, 2015; Chaggara et al., 2017).

For an in-depth study of this topic, it is necessary to reproduce the concatenation of the events triggering the generation of ionospheric irregularities. The physical conditions that occur in the circumterrestrial medium during the different phase of geomagnetic storms, namely the sudden impulse, the main phase and the recovery phase, can be ascribed to solar drivers using *in-situ* measurements of solar wind plasma (Svalgaard, 1977; Feldstein et al., 1996; Ruohoniemi and Greenwald, 2005; Liu et al., 2015). The geomagnetic field data analyse, provided by both satellite and ground-based observatories, can help to evaluate the evolution of the magnetospheric and ionospheric current systems during storms (Lui et al., 1993; Apatenkov et al., 2007; Villante and Piersanti, 2008; Li et al., 2014; Piersanti and Villante, 2016). Other key elements are provided by the analysis of the irregularities scale sizes in which the ionospheric plasma is fragmented. This information can be derived from TEC (Total Electron Content) data provided by GNSS receivers (Mendillo, 2006) and can be placed in relationship with scintillation occurrence (Alfonsi et al., 2011).

The present PhD project presents an unprecedented combination of diverse data sets to explain GNSS scintillation.

The main objective of this work is to understand how different configurations of the IMF-magnetosphere-ionosphere coupling are translated into different structuring and dynamics of the ionosphere. In this context, the open issues to which this work contributes are identification of those physical properties that if properly reproduced can lead to a forecast, from few minutes to few hours before the event of the disturbance effects induced by the polar ionosphere on GNSS systems. In detail, starting from the scintillations recorded by selected GNSS receivers at ground this project investigates the origin of irregularities: by evaluating the ionospheric background, under different interplanetary conditions; by studying the magnetosphere configuration during the main phase of intense geomagnetic storms; by reconstructing the ionospheric scenarios resulting in the observed scintillations. The work focuses on the study of major storms of the 24th solar cycle and in particular on their main phase that occurred on 2015 March 17th, 2015 June 22nd and 2017 September 08th, respectively. The choice of such case studies was motivated not only by the intensity (that ensured a strong perturbation of the polar ionosphere) but also because those storms, having been caused by different solar phenomena and occurring in different seasons, have given rise to geomagnetic disturbances that are useful for the irregularities characterization under different helio-geophysical conditions. This characterization is essential to contribute to the development of future forecasting models.

The open issues addressed in this work concern:

1. determination of the ionosphere's response time due to magnetosphere's perturbation events;
2. quantification of the ionospheric disturbance intensity in comparison with the intensity of the solar disturbance;
3. identification of the polar region most exposed to the disturbance;
4. identification and quantification of the ionospheric response in term of asymmetry level between the two hemispheres;

5. study of the evolution of ionospheric irregularity dynamics in comparison with solar driver evolution.

The method follows a multi-instrumental and multi-parametric approach that combines information derived from ground-based measurements with those derived from space-based stations. Such approach allows the reconstruction of the spatial-temporal context in which the selected events occurred. This method implies the integration of a broad spectrum of information necessary to characterize the ionospheric disturbances at different time scales (from milliseconds to days) and spatial scales (from millimetres to hundreds meters/kilometres) in accordance with the evolution of the storms drivers. A summary of the addressed aspects is described below with respect to the previous list.

1. Recently, some researchers have chosen to analyse measurements acquired from different instruments in order to determine the ionospheric response times during disturbed conditions (see e.g. De Franceschi et al., 2008; Burston et al., 2009; Astafyeva et al., 2015; Cherniak and Zakharenkova, 2016). Continuing along a similar approach, the observations provided by satellites orbiting the first Lagrangian point (L1), by geostationary satellites, by GNSS constellation (which orbits around 20000 km from the Earth's surface), by magnetospheric and ionospheric satellites and by devices placed on the ground are analysed and interpreted. Thanks to a multi-instrumental and multi-parametric approach, the integration of the different information derived from these instruments allows to reconstruct the ionospheric scenario overcoming some missing measures due for example to ionospheric absorption, instrument saturation, poor coverage ensured by fields of view of the considered instruments.
2. The quantification of the intensity of the ionospheric disturbance in terms of GNSS scintillation in relation to the intensity of the solar disturbance is probably the most crucial issue. The availability of both interplanetary and magnetospheric plasma observations allows quantifying their disturbance level. However, experimental evidence showed that the effects of storm drivers in the ionosphere is often not proportional to the disturbance level recorded in the interplanetary space (Mitchell et al., 2005; Mendillo, 2006). For this reason, understanding physical mechanisms that bind the solar wind-magnetosphere-ionosphere coupling become essential to provide an advancement to current knowledge. This work deals with this aspect showing the heterogeneity of the ionospheric response to the major storms of the 24th solar cycle through multi-instrumental study.
3. A careful analysis and interpretation of measures provided by different instruments allows identifying the ionospheric regions most affected by the storm. For this purpose, a significant amount of data (acquired systematically and continuously) is needed. The advantage of this project is the possibility of having ground based GNSS measurements acquired by networks directly managed by the Istituto Nazionale di Geofisica e Vulcanologia (INGV) or by its scientific partners. The coverage of the investigated sectors allows identifying areas in which the ionosphere proves to be unexpectedly disturbed, underlining, once again, the complexity of the system.
4. The observational coverage of both polar regions allows an improved understanding of the response of the two hemispheres to the same interplanetary disturbance (Prikrýl et al., 2013). This aspect has not yet been fully understood and deserves to be addressed through the multi-instrumental and multi-parametric approach. For this reason, this work considers data acquired

both in the Arctic and in Antarctica showing possible symmetries/asymmetries in the IMF-magnetosphere-ionosphere interaction.

5. A full understanding of the main characteristics, in terms of size and orientation, of the ionospheric irregularities causing disturbances on trans-ionospheric signals has not been reached (Secan et al., 1997; Prikryl et al., 2012). The same can be said for the prediction of origin and evolution of irregularities in space and time, which is not yet sufficiently reliable (Pettigrew et al., 2010). This project is part of this still underdeveloped context and suggests approaches for further ionospheric plasma dynamics.

Thesis structure

The thesis develops on five chapters of which the first three are preparatory to understand the results, which are described in the fourth chapter. The fifth and last chapter presents the discussion of the achieved results, concluding remarks and future perspectives of this work. In detail, the thesis is organized as follows. Chapter 1 summarizes the general overview of the current theoretical understanding of magnetosphere-ionosphere coupling and of physical and observational characteristics, providing a comprehensive, yet concise, picture of the available scientific literature, which represents the starting point of this study and the necessary premise to understand the results. Chapter 2 presents the theory of ionospheric scintillations, providing also a description of the GNSS receivers used and the scintillation parameters that such receivers provide. This chapter also describes the data treatment of the scintillation parameters selected for the investigation. Chapter 3 motivates the choice of a multi-observation approach aimed at advancing understanding of the physical processes that give rise to the formation of ionospheric irregularities causing scintillations in the polar region of both hemispheres. In particular, this chapter provides descriptions of the parameters selected to characterise the ionospheric behaviour under strong perturbation of the magnetosphere-ionosphere system, providing also the motivation and the critical issues related to their choice. Chapter 4 describes the results obtained by applying the analysis presented in the previous chapter on the main phases of three intense geomagnetic storms that occurred during the solar cycle 24. Chapter 5 discusses the main findings achieved through the investigation of the three case studies and draws the conclusions of the work conducted throughout this thesis highlighting both the effectiveness of the adopted method and the contribution to progress beyond the state of the art. This chapter underlines the scientific but also the applicative value, in the space weather sense, of this results.

CONTENTS

Chapter 1	10
Magnetosphere-Ionosphere Coupling at High Latitudes.....	10
1.1 The Sun, Its Activity and The Solar Wind	10
1.2 The Earth's Magnetosphere	12
1.2.1 Magnetospheric current systems	14
1.3 The Earth's Ionosphere.....	18
1.3.1 Latitudinal Variation of the Ionosphere	20
1.3.2 Auroral Electrojets	21
1.4 Causes and Effects of Space-Earth Coupling	22
1.4.1 Solar Wind-Magnetosphere Interactions	23
1.4.2 Large Scale Electrodynamics of The Polar Ionosphere	24
1.4.3 Magnetospheric Dynamics.....	25
1.4.4 Geomagnetic Activity Indices.....	28
1.4.5 Irregularities of The Polar Ionosphere	29
Chapter 2.....	32
The Ionospheric Scintillation	32
2.1 Global Navigation Satellite System (GNSS).....	33
2.2 GNSS Receivers for Ionospheric Studies	35
2.2.1. Scintillation Indices.....	37
2.2.2. Total Electron Content and Its Gradients.....	38
2.3 Method to Treat TEC and Scintillation Data.....	40
Chapter 3.....	43
The Challenge to Trace Back the Physical Mechanisms Causing the Observed Scintillations	43
3.1 The Need to Integrate Ancillary Data.....	43
3.2 Data Ingestion Challenge.....	46
3.3 Possibility of Using Models.....	50
Chapter 4.....	52
Scintillation Events during Three Strong Geomagnetic Storms of the Solar Cycle-24	52
4.1 The 2015 March Storm.....	52
4.1.1 Results.....	52
4.2 The 2015 June Storm.....	64
4.2.1 Results.....	64

4.3	The 2017 September Storm	75
4.3.1	Results.....	76
Chapter 5	85
	Introduction	85
	Discussion	85
5.1	2015 March Storm	85
5.2	2015 June Storm	89
5.3	2017 September Storm	91
5.4	Comparative Analysis of the Three Storms.....	94
5.5	Summary and Conclusions	98
	Future Steps	99

CHAPTER 1

MAGNETOSPHERE-IONOSPHERE COUPLING AT HIGH LATITUDES

This chapter summarizes the current theoretical understanding of the magnetosphere-ionosphere coupling and its physical and observational characteristics. In particular, this chapter forms a synopsis of the general solar-terrestrial connection by describing the Sun, its activity, the solar wind, the magnetosphere and the ionosphere (with particular reference to the polar ionosphere). Furthermore, the interaction between the Sun and the Earth in terms of geomagnetic activity will be described to provide a comprehensive, yet concise, picture of the available scientific literature, which represents the starting point of this study and the necessary premise to understand the results.

1.1 THE SUN, ITS ACTIVITY AND THE SOLAR WIND

The Sun is a plasma sphere, held and compressed by its own gravitational attraction, with a radius of approximately $6,96 \cdot 10^8$ m and a mass of $1,99 \cdot 10^{30}$ kg (Stix, 2004). It consists of hydrogen ($\sim 90\%$) and helium ($\sim 10\%$) along with carbon, nitrogen, oxygen and other elements in similar proportions as on Earth ($\sim 0,1\%$) (see e.g., Kivelson and Russell, 1998; Parks, 1991). The Sun is composed of three internal layers: a deep, dense hot core (where nuclear fusion processes take place), a radiative region and a convective region. Three layers also compose the Sun's atmosphere. The photosphere is the lowest layer of the solar atmosphere in which the Sun's energy is released as visible light. Bright, bubbling granules of plasma and darker, cooler sunspots mark it. Just above the photosphere, there is the chromosphere. The main characteristics of this layer are the density logarithmic decrease that makes the chromosphere normally invisible and a temperature decrease. Finally, there is the corona, an aura of hot plasma ($\sim 10^6$ K) that surrounds the Sun. The exact mechanism by which the corona is heated is still uncertain but seems to be linked to induction by the Sun's magnetic field and MHD (magnetohydrodynamic) waves from below (Schrijver and Zwaan, 2008). The corona extends far into the solar system and has a very complicated structure containing flares, plagues, prominences, filaments and coronal holes all related to the complex magnetic field of the Sun.

Our star, indeed, has a magnetic field with an average strength of $\sim 10^{-4}$ T (see e.g. Parks, 1991), which is thought to be generated in the thin interface layer between the radiative and the convective zones and supported by a dynamo effect due to convective motion taking place in the convective region. The shape of the solar magnetic field is very complicated mainly due to the differential rotation of the Sun. In fact, the (dipolar) magnetic flux tubes, that are expelled from the convective cells are highly twisted and sheared by differential rotation of the Sun, due to the combined effects of advection and diffusion of the magnetic lines (Parker, 2003). This phenomenon is closely connected to the solar activity. Changes in solar magnetic field bring about spectacular phenomena that are visible on the Sun's surface such as sunspots, flares and coronal mass ejections (CMEs).

Sunspots appear as black regions on the solar disk since they are cooler than the surrounding of the solar surface. This is due to the strong magnetic fields, which emerging from the interior inhibits the convective motion. Sunspots do not appear at random over the solar disk but are concentrated in two latitude bands on either side of the equator. Their number varies according to an 11 years period, which corresponds to the activity period of the Sun's magnetic field, known as *solar cycle* (Akasofu

and Chapman, 1972). During a solar cycle, the sunspots originate in the high-latitude photospheric regions and then migrate towards the equator, where they disappear. As a consequence of the solar cycle the shape of magnetic field changes showing a ‘simple’ dipolar structure in correspondence to solar minimum and a complex magnetic structure in correspondence to a maximum. Another important feature of the solar magnetic field are the *coronal holes*, which are regions filled with colder, less dense plasma compared with the surrounding plasma and a magnetic field that opens freely into interplanetary space. They usually cover regions around the Sun’s poles but they also can be found everywhere on the corona.

The magnetic structures that originate during a maximum in the solar activity can cause an explosion on the Sun. Such explosions are known as *solar flares* and occur when the energy stored in twisted magnetic fields (usually above the sunspots) is suddenly released (Kamide and Chian, 2007). Flares are usually classified based on their brightness in X-ray emission according to three categories:

- X-class flares are the most intense events ($\geq 10^{-4} \text{ Wm}^{-2}$) and can trigger planet-wide radio blackouts and long-lasting radiation storms.
- M-class flares which are medium-size events ($10^{-5} - 10^{-4} \text{ Wm}^{-2}$) that can cause brief radio blackouts that affect Earth's polar regions.
- C-class flares which are the smallest events ($10^{-6} - 10^{-5} \text{ Wm}^{-2}$) with few noticeable consequences on Earth.

Such events are often followed by CMEs, which correspond to huge releases of plasma and magnetic field from the solar corona into interplanetary space or beyond (Low, 2001). Such eruptions typically reach Earth in 1-5 days and can influence the performance and reliability of space-borne and ground-based technological systems. Another result of solar magnetic activity are interplanetary shocks (IPs). They are often associated with CMEs and cause abrupt variations in the interplanetary medium characteristics such as temperature, density, IMF strength and plasma velocity. For this reason, they can strongly affect the magnetosphere-ionosphere system.

Most of the energy produced by the Sun reaches the Earth as photons (Akasofu and Chapman, 1972). However, a very highly conductive plasma also escapes in all directions from the corona with a supersonic velocity. This plasma is known as *solar wind*, which forms because of the gas pressure difference between the solar corona and interplanetary space (see e.g. Kivelson and Russell, 1998). The high temperatures of the solar corona induce plasma to stream away from the solar gravitational potential. The solar wind is essentially composed of an equal number (per volume) of electrons and protons ($\sim 95\%$) and a small percentage ($\sim 4\%$) of alpha particles. At 1 astronomical unit (AU), which correspond to the mean Sun-Earth distance, the solar wind’s temperature is $(7,4 - 8) \cdot 10^4 \text{ K}$, its density is roughly $4-5 \text{ cm}^{-3}$ and its average speed is 400 km/s (Lepping et al., 2003).

The solar wind is a highly conducting, non collisional plasma and, to a first approximation, the ideal single fluid MHD model can describe it (Schunk and Nagy, 2009). Hence, it carries a weak magnetic field, which is *frozen into the plasma* forming the Interplanetary Magnetic Field (IMF) that is about $3-4 \text{ nT}$ at 1 AU (Lepping et al., 2003).

The solar wind flows radially outward, but due to the Sun’s rotation, the large scale IMF acquires a spiral form known as *Parker spiral* as shown in Figure 1a. At 1 AU the spiral makes an angle of

approximately 45° to the Sun-Earth line hitting the Earth's magnetosphere in the late morning direction. Furthermore, as the solar wind carries the IMF, the magnetic lines anchored at the Sun assume different polarities in each hemisphere causing a current sheet in the equatorial plane that separates the inward and the outward directed field. Due to the tilt of the solar magnetic dipole, the spiraling current sheet warps into a shape often referred as *ballerina skirt* (Figure 1b). Consequently, an observer on Earth will see alternatively positive and negative magnetic field regions called *sectors*. This property is of great importance to the ionosphere, especially at high latitudes. The IMF affect the ionospheric plasma circulation pattern (see section 1.4.2). Furthermore, when the north-south component of the IMF ($B_{z,IMF}$) is negative, due to magnetic reconnection between the IMF and the geomagnetic field (see section 1.4.1), a remarkable amount of ionizing particles coming from the Sun can access the magnetosphere-ionosphere system.

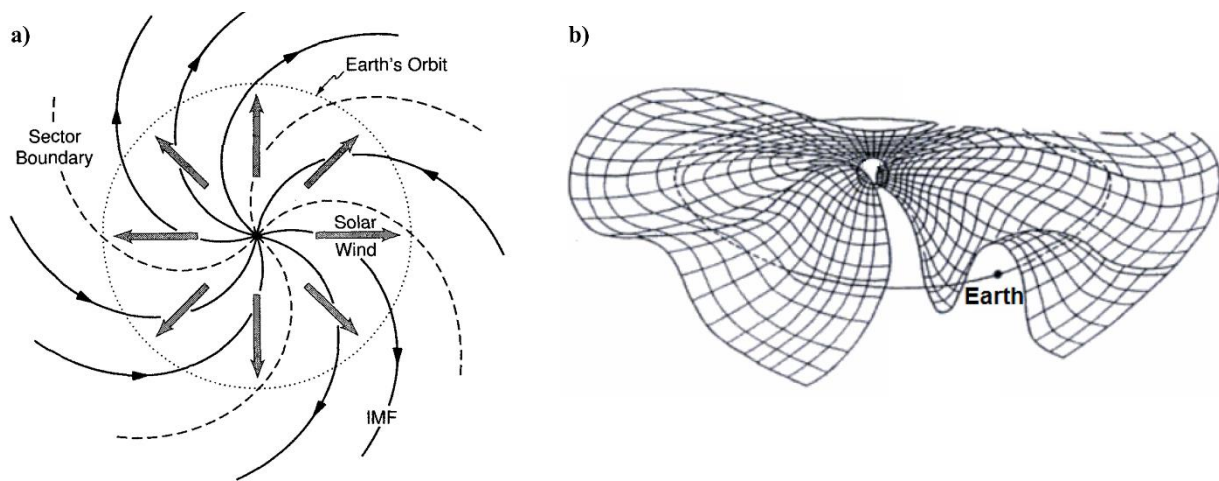


FIGURE 1: a) The Parker spiral of the Interplanetary Magnetic Field in the equatorial plane and its sector structure (taken from Baumjohann and Treumann, 1996). b) Three-dimensional topology of the solar wind current sheet separating oppositely directed field lines, known as *ballerina skirt* (taken from Schunk and Nagy, 2009).

1.2 THE EARTH'S MAGNETOSPHERE

The Earth has its own magnetic field of internal origin that would have a configuration very similar to that of a dipole of moment roughly equal to $8 \cdot 10^{22} \text{ Am}^2$, if it did not interact with the solar wind. The dynamic pressure of the solar wind compresses the Earth's magnetic field on the dayside and stretches it out on the nightside into a long *magnetotail*. Because of the frozen in principle, which implies that the plasma coming from the Sun cannot leave the IMF, the Earth's magnetic field deflects around itself the solar wind. The cavity formed by the Earth's magnetic field in the solar wind is known as *magnetosphere*. Figure 2 shows its schematic representation.

The boundary between the Earth's magnetic field lines and the IMF is called *magnetopause*. Its location can change depending on the IMF strength, the IMF direction and the solar wind pressure. In quiet conditions, it is located at $10 R_E$ where R_E is the Earth's radius of ~ 6380 km.

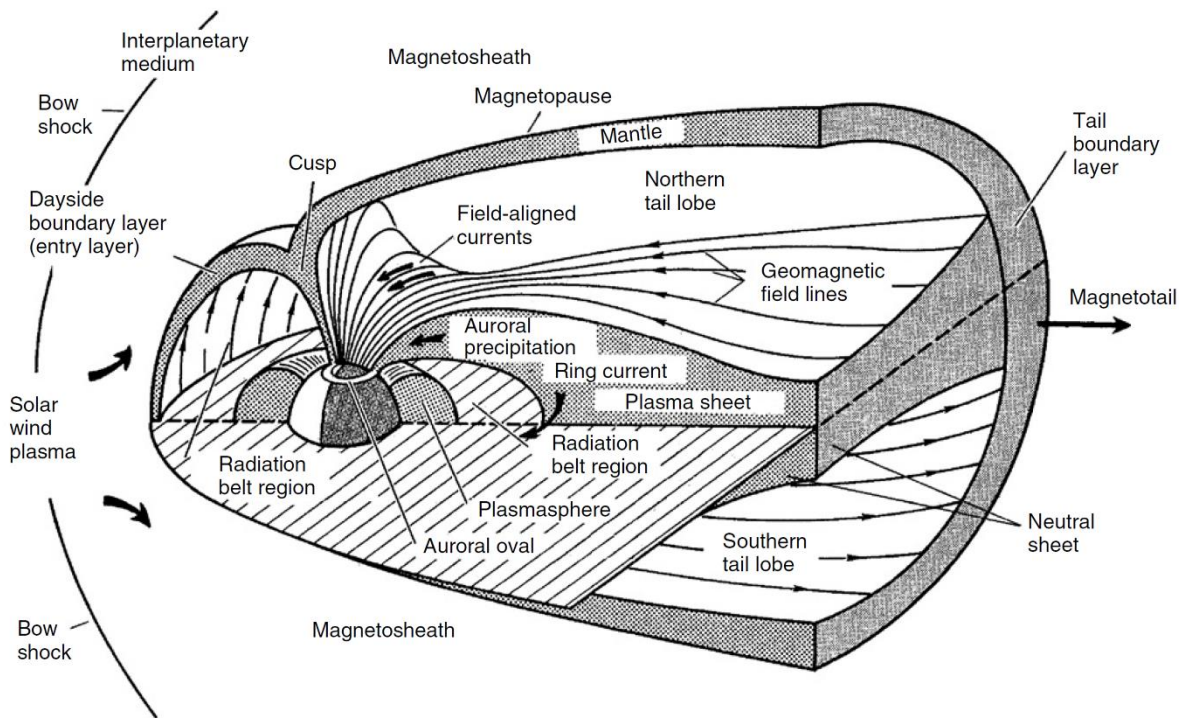


FIGURE 2: A schematic diagram of the Earth's magnetosphere (taken from Kelley, 2009).

The impinging solar wind is super-Alfvénic, so a MHD shock is formed on the dayside, named *bow shock*. Such shock converts some of the solar wind kinetic energy into thermal energy, so the region downstream of the shock is made of denser and hotter plasma than the solar wind and it is called *magnetosheath*. This plasma plays a very important role in maintaining the ionosphere as it contributes to its ionization at night.

The plasma populating the magnetosphere comes from the solar wind and from the ionosphere. It is quite unevenly distributed and grouped in different regions with different densities and temperatures. Proceeding from the inside towards the outside of the magnetosphere the *plasmasphere* is the first region encountered. This region is filled with cold plasma (with energies of ~ 1 eV) and is characterized by closed magnetic field lines. Outer of the plasmasphere there is a region called *radiation belt* in which ions and electrons, trapped on closed field lines, oscillate from one hemisphere to another, due to stronger magnetic field close to the poles (for a more detailed description of this phenomenon see e.g. Baumjohann and Treumann, 1996). Particles populating this region are the most energetic particles in the magnetosphere having energies of ~ 1 MeV and more (see e.g. Kivelson and Russell, 1998). Such particles also contribute to the ionization of the upper atmosphere when precipitate out of the trapping region. In the *magnetotail* plasma is mainly concentrated in a region called *plasma sheet* populated by hot plasma (with energies of $\sim 1-100$ keV and more) originated in part from the solar wind. This region is essentially co-located with the near-earth central region of the magnetotail where the magnetic field reverses direction (see e.g. Hargreaves, 1992). Following the magnetic field lines, particles populating this region can reach the high latitude ionosphere

contributing to its ionization. A more detailed description of the different magnetospheric regions can be found, for example, in Akasofu and Chapman (1972), Sonnerup (1985) or in Proelss (2004).

An important magnetospheric feature, due to the interaction between the solar wind and the Earth's magnetic field, is that some of the Earth's field lines are no longer closed and they directly connect with the IMF (see section 1.4.1). Such lines are located in the polar regions and the area encompassing their ground projection is known as the *polar cap*. The boundary between the open and closed field lines (see section 1.4.1) delineates the *auroral ovals*, whose size depends on solar activity. They are approximately off-centre rings shifted by an average 4° from the magnetic pole toward magnetic midnight (Meng et al, 1977). In addition, on the magnetospheric dayside some field lines distribute along the magnetopause in opposite directions. The regions formed by such magnetic lines are named *polar cusps*. Cusps are funnel-shaped regions filled with magnetosheath plasma, which can enter the magnetosphere without having to cross field-lines. The expected position for the cusps is between $\pm 78^\circ$ of magnetic latitude, but these move to lower latitudes following strong solar activity because of a strong magnetospheric compression. In these regions, particles coming from the Sun enter into the magnetopause producing severe disturbed conditions of the ionosphere-magnetosphere system.

1.2.1 MAGNETOSPHERIC CURRENT SYSTEMS

The Earth's magnetosphere contains complicated current systems whose structure is influenced by the interaction with the solar wind and the IMF. The main magnetospheric currents are described below and illustrated in Figure 3. Ganushkina et al., (2015) provide a more detailed description of the magnetospheric current systems.

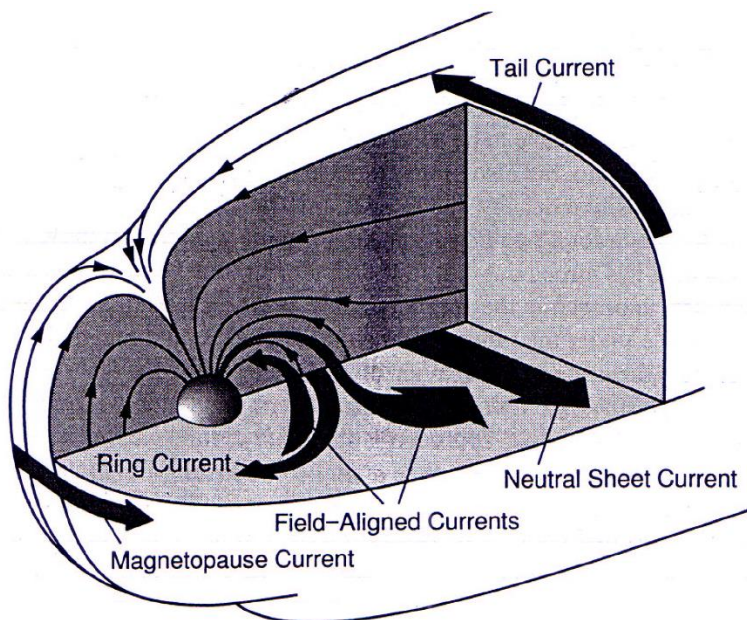


FIGURE 3: Magnetospheric current systems (taken from Baumjohann and Treumann, 1996).

Magnetopause Current

The magnetopause current is generally described as a surface current layer separating the solar wind from the magnetospheric field (Figure 4). This current represents a surface across which the magnetic

field strength jumps from its low interplanetary value to the high magnetospheric field strength. Its task is closing the magnetospheric cavity from external plasma input.

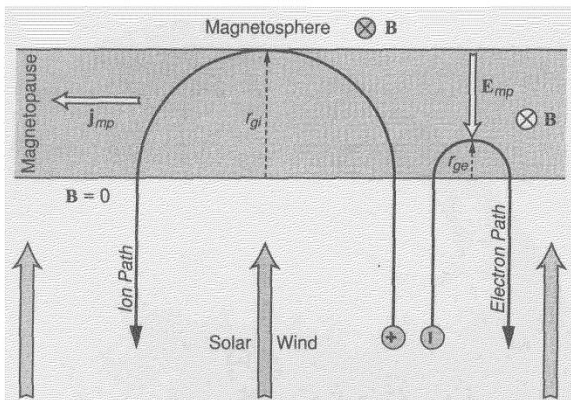


FIGURE 4: Generation scheme of magnetopause current (taken from Baumjohann and Treumann, 1996).

In fact, as it is visible in Figure 4 reflected ions and electrons, hitting the magnetospheric field inside the magnetopause boundary, perform half a gyro-orbit inside the magnetic field before escaping with reversed normal velocity from the magnetopause back into the magnetosheath. The thickness of the solar wind-magnetosphere transition layer under such idealized conditions becomes of the order of the ion gyro-radius. The sense of gyration inside the boundary is opposite for both kinds of particles leading to the generation of a narrow surface current layer. This current provides the additional magnetic field, which compresses the magnetospheric field into the magnetosphere and at the same time annihilates its external part (Baumjohann and Treumann, 1996). The magnetopause current, in the equatorial plane, flows from dawn to dusk and closes in the tail magnetopause, where it splits into northern and southern parts flowing from dusk to dawn. This flow separates the solar wind from the magnetospheric field even if over the poles there is an area of weak magnetic field (or day-side cusp), which allow solar wind particles to enter the magnetosphere (see Figure 3 and section 1.2).

Cross-Tail Current

The down solar wind extension of the magnetosphere into a tail indicates the presence of a current flowing across the plasma sheet (which is the layer separating the two tail lobes) from the dusk to the dawn side (Hargreaves, 1992). As the tail is bounded this requires a tail current in the form of a double solenoid (Figure 5).

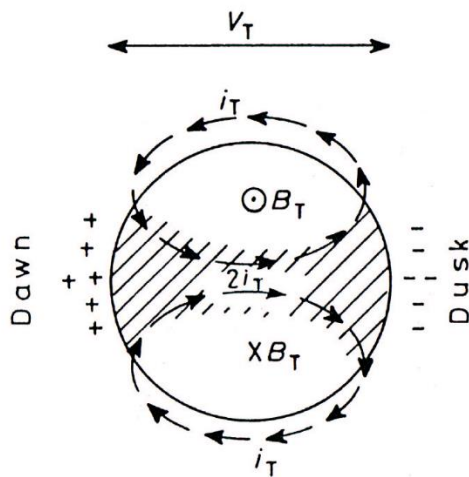


FIGURE 5: Tail current as observed from the Earth (taken from Hargreaves, 1992).

When the solar activity (see section 1.1) is low, the cross-tail current thickness is $\sim 5 R_E$ and has an internal margin named hinging point. This is the separation point between dipolar and stretched field lines in the tail and it is located, during a low solar activity, $\sim 7 R_E$ from the Earth's surface at local midnight.

Ring Current

The ring current flows azimuthally around the Earth from east to west between 4 and 6 R_E (see e.g. Hargreaves, 1992). At this distance almost all atmospheric particles are fully ionized and, hence, subject to the effects of electric and magnetic fields. Here energetic charged particles tend to behave independently rather than as part of a fluid. The behaviour of these particles may be approximated by the superposition of three types of motion gyration about the main field, "bounce" along field lines, and azimuthal drift in rings around the Earth (see e.g. Baumjohann and Treumann, 1996). Gyration is caused by the Lorentz force, which makes charged particles move in circles around magnetic field lines. When particles reach the ends of field lines, they are reflected due the converging geometry of a dipole field. The mirror force that reflects particles is a component of the Lorentz force antiparallel to the motion of the particle when field lines converge. Two effects produce azimuthal drift. They are a decrease in the strength of the main field away from the Earth and a curvature of magnetic field lines. Particles of opposite charge drift in opposite directions because their sense of gyration about the direction of the magnetic field is opposite. In fact, protons gyrate in a left-handed sense with respect to the Earth's rotation axis drifting westward, while electrons gyrate in a right-handed sense and drift eastward. Because particles drift in opposite directions, they produce an electric current in the same direction as the proton drift. The direction of this current is such that its magnetic field acts to oppose the magnetic field of the Earth inside the ring.

Field-Aligned Currents

The field-aligned (FACs) are currents flowing in polar regions following the magnetic field direction. This current system provides the transfer of energy derived from the interaction between the solar wind and the magnetosphere to the ionosphere, allowing also the transfer of convection electric fields and particle precipitation (see e.g. Kamide, 1982; Lysak, 1990; Iijima, 2000; Coxon et al., 2016; Zhu

et al., 2017). FACs, thus, allow the electromagnetic interaction between hot magnetospheric plasma and cold ionospheric plasma (Baumjohann, 1982).

Birkeland (1908), after whom the currents system is named, was the first to propose their existence to explain magnetic disturbances observed in the polar regions. Iijima and Potemra (1976a, b) first deduced the average FAC configuration and catalogued them into Region 1 (the most poleward) and Region 2 (lying equatorward) currents, as shown in Figure 6. They also identified a third dayside current system (cusp currents in Figure 6), poleward of Region 1, which they associated with dayside cusp current and later correlated with the plasma mantle (Iijima, 2000).

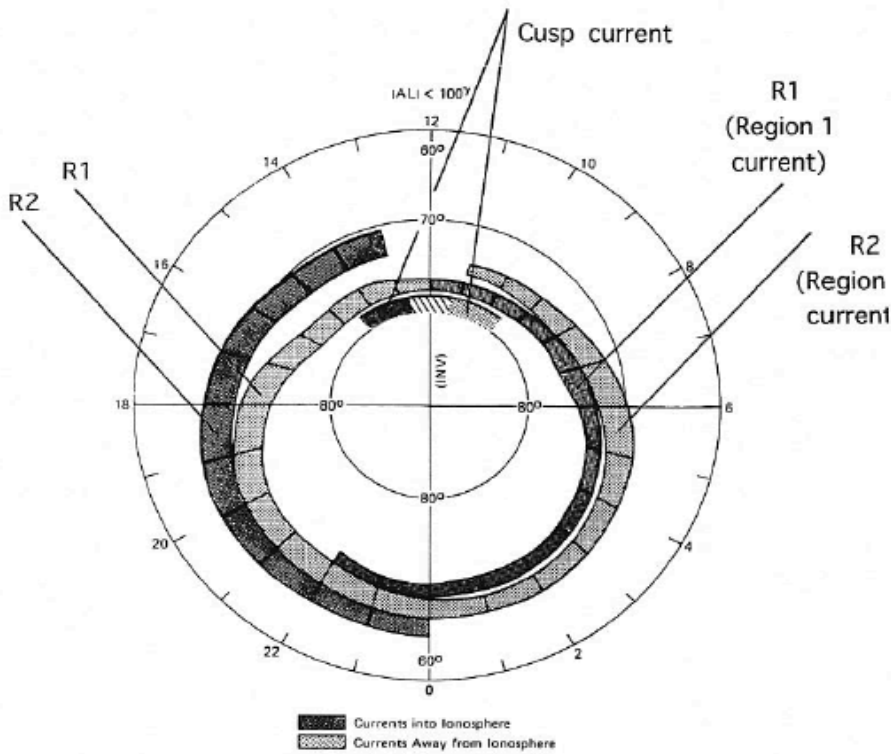


FIGURE 6: Field-aligned currents pattern (taken from Iijima and Potemra, 1976a).

Seen from Figure 6, Region 1 currents flow toward the ionosphere on the dawn-side and out of the ionosphere on the dusk-side, while Region 2 currents, which are defined as opposite in sign, flow in opposite direction. These two current sheets are caused by different physical mechanisms, but they are connected through the ionosphere and form a single circuit (see section 1.3.2). Region 1 currents originate in the interface region between field lines dragged tailward by solar wind and field lines returning to dayside of the Earth. Due to the Lorentz force, this interface is positive charged on the dayside of the Earth and negative on the nightside. Positive charges moving tailward on the dawn-side are deflected earthward toward the interface. In contrast, positive charges moving sunward inside the interface are deflected away from the Earth. In such a way, a positive charge accumulates. On the dusk-side, the deflections are the same but a negative charge accumulates at the interface. As magnetic field lines of the Earth are almost perfect current conductors the effects of the charge separation in the magnetosphere is connected to the ionosphere at the feet of field lines. As the ionosphere conducts current, this can flow from the positive to negative terminals. Thus, currents in Region 1 flow toward the ionosphere on the dawn-side, then crossing the polar ionosphere flow out of the ionosphere on the dusk-side. Region 2 currents are a result of charge separation due to the drift

motion. In fact, as discussed in relation to the ring current in the previous section, electrons drift eastward around the Earth, while positive charges drift westward. These particles preferentially approach the Earth on the nightside due to magnetospheric convection system. Approaching the Earth, negative charges drift around the Earth on the dawn-side while positive charges around the dusk-side. Accordingly, in Region 2 currents flow out of the ionosphere on the dawn-side and toward the ionosphere on the dusk-side. These currents, which are usually present, during disturbed conditions become more intense as well as move equatorward (Iijima and Potemra, 1978).

1.3 THE EARTH'S IONOSPHERE

The ionosphere is the transition region between the fully ionized magnetosphere and the neutral atmosphere, forming the base of the magnetospheric plasma environment. It consists of a mixture of ionized and neutral particles extending from about 50 to 1000 km above the terrestrial surface. Although the charged particles are only a minority, they are able to significantly influence the propagation of radio waves in the high-frequency (HF) band (3–30 MHz). The presence of ionized particles is mainly due to solar radiation in the ultra-violet (UV) spectral range (wavelengths $< 10^{-7}$ m) that photoionises and photodissociates atmospheric neutral particles, such as N_2 , O_2 and O . As the photoionization rate depends on the solar flux, the ionosphere varies with geographic latitude, longitude, time of the day, season and altitude (see e.g. Baumjohann and Treumann, 1996, Hargreaves, 1992). In particular, the ionised population density rises during the day in correspondence with the Sun elevation and decays via recombination at night when the solar UV source vanishes (see e.g. Kelley, 2009). However, a further ionization mechanism exists: the *impact ionization*, which is due to solar and/or magnetospheric energetic particle precipitating into the ionosphere. It is the most important ionization source at high latitudes maintaining the ionosphere during the long lasting polar night and making it highly sensitive to solar activity.

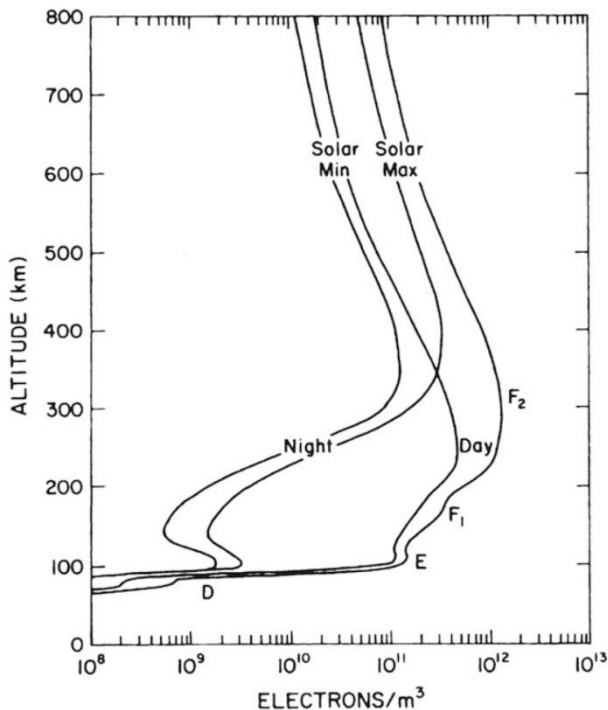


FIGURE 7: Typical mid-latitude ionospheric electron density profiles for a solar activity maximum and minimum at daytime and night-time (taken from Richmond, 1987).

The concentration of ionisable gases reduces with increasing height, while the intensity of the solar radiation increases. Therefore, the concentration of ionized population (hereafter *electron density* because the ionosphere can be considered electrically neutral) passes through a maximum at some given altitude. Furthermore, as the atmospheric composition varies with altitude as well as the response to solar radiation of different atomic species, the electron density presents a trend characterized by relative maxima and minima. These identify different ionospheric regions, which can be defined as follows (Hunsucker and Hargreaves, 2002):

- D region, 60-90 km and electron density $\sim 10^8 - 10^{10} \text{ m}^{-3}$;
- E region, 100-160 km and electron density $\sim 10^{11} \text{ m}^{-3}$;
- F1 region, 160-180 km and electron density $\sim 10^{11} - 10^{12} \text{ m}^{-3}$;
- F2 region, altitude maximum variable around 300 km and electron density of up to several 10^{12} m^{-3} ;

Each of this region has its own maximum plasma frequency (known as critical frequency), which is the highest frequency that can be reflected from the specific ionospheric region (see e.g. Hargreaves, 1992). All these regions are highly variable depending on the solar radiation and solar activity (Figure 7). In particular, the D and F1 regions vanish at night mainly due to recombination processes between ions and electrons, while the E region becomes much weaker. The F2 region tends to persist, though at reduced intensity. In addition, sometimes a thin layer occurs in the ionospheric E region, between 100 and 125 km (Whitehead, 1961; Didebulidze et al., 2015). An anomalous high electron density that often exceeds the ionospheric electron density maximum, which is normally located at about 350 km in the F region, characterizes it. Due to its sudden and unpredictable nature, it is called “sporadic” E layer (*Es*). The *Es* formation mechanisms cannot be explained according to Chapman theory (Pietrella and Bianchi, 2009). Its formation is ruled by the presence of zonal neutral wind (“wind shear” mechanism, see Mathews, 1998). This mechanism involves the horizontal component of the geomagnetic field and a vertical gradient in the zonal wind, which through the drag and the Lorentz force constrain the ions in a thin region in the E layer. This layer appears irregularly both during the day and night.

Consisting of a mixture of neutral and ionized particles, the ionosphere has an electrical conductivity to which coulomb and neutral collisions may contribute (see e.g. Baumjohann and Treumann, 1996). Since the ionosphere is an anisotropic plasma, the electric currents do not only follow the electric field direction. Therefore, it is necessary to use a conductivity tensor in Ohm’s law. In a general case in which $\vec{E} = (E_x, E_y, E_z)$ and $\vec{B} = (0, 0, B_z)$, Ohm’s law can be written as:

$$\begin{pmatrix} J_x \\ J_y \\ J_{\parallel} \end{pmatrix} = \begin{pmatrix} \sigma_p & -\sigma_H & 0 \\ \sigma_H & \sigma_p & 0 \\ 0 & 0 & \sigma_0 \end{pmatrix} \begin{pmatrix} E_x \\ E_y \\ E_{\parallel} \end{pmatrix} \quad (1.1)$$

where J_{\parallel} and E_{\parallel} are the current density and electric field components parallel to the magnetic field \vec{B} respectively. In equation (1.1), σ_p is the *Pedersen conductivity*, σ_H is the *Hall conductivity* and σ_0 is the *ohmic conductivity*. σ_p is parallel to the external electric field \vec{E} and orthogonal to the

magnetic field \vec{B} . *Pedersen currents* mainly flow between 120 and 150 km above the Earth's surface. At these heights, ions are subjected to more intense $\vec{E} \times \vec{B}$ drift than electrons generating a westward current flow parallel to the external electric field \vec{E} and orthogonal to the magnetic field \vec{B} . σ_H is perpendicular both to the external electric field and to the magnetic field. The *Hall currents* flow between about 90 and 120 km, in which only the electrons are subjected to $\vec{E} \times \vec{B}$ drift toward the night side. Such currents are perpendicular both to the external electric field and to the magnetic field. σ_0 is parallel to the magnetic field and characterises heights above 150 km from the Earth's surface. In such a regions, currents flow parallel to the magnetic field because ions and electrons are affected by \vec{B} and can move only due to $\vec{E} \times \vec{B}$ drift, which does not give currents.

Another important feature of the ionosphere, related to its inhomogeneous, anisotropic, and dispersive nature, is that its refractive index depends upon the electromagnetic wave's frequency and it can be expressed as:

$$k^2 = 1 - \frac{X^2}{1 - iZ - \frac{Y_T^2}{2(1 - X - iZ)} \pm \sqrt{\frac{Y_T^4}{4(1 - X - iZ)^2} + Y_L^2}} \quad (1.2)$$

Such equation is known as *Appleton-Hartree equation* in which $X = \frac{f_n}{f}$ is the electronic plasma parameter (where f_n is the electron plasma frequency and f is the frequency of the transmitted wave), $Y = \frac{f_g}{f}$ is the cyclotron plasma parameter (where f_g is the electron gyrofrequency) and $Z = \frac{\nu_c}{2\pi f}$ is the electronic collisions frequency (where ν_c is the electron collision frequency).

According to equation (1.2) the propagation of an electromagnetic wave into the ionosphere is possible for all real k values. Furthermore, the presence of the double sign that appears in the denominator shows the ionospheric birefringence, which involves the split of the electromagnetic wave into two different propagation rays: the *ordinary radius* and the *extraordinary radius*, in analogy with optical birefringence. In the perturbed ionosphere and especially into the F region, this distinction may come to fall. In fact, at these altitudes, the presence of strong perturbation to the ionospheric plasma can give rise to a frequency widening of the reflected trace in an ionogram (see section 3.1), more commonly known as *spread F* (Hunsucker and Hargreaves, 2002).

1.3.1 LATITUDINAL VARIATION OF THE IONOSPHERE

The Earth's ionosphere can be divided into three different regions according to the magnetic latitude that have rather different characteristics. The midlatitude ionosphere, more explored and therefore better understood, has an ionization almost entirely due to solar emission, especially in the UV band of the electromagnetic spectrum. This ionization is lost by means of chemical recombination processes that can involve both the atmospheric neutral constituents and the ionized species. The motion of the ionised particles as well as the balance between production and loss is also connected to the neutral winds that flow into the atmosphere. Such processes also operate at low and high latitude, but additional processes are also important in those regions.

At high latitudes, the Earth's magnetic field is nearly vertical resulting in an ionosphere that is considerably more complex than that in low and middle latitudes. Because of the shape of the magnetic field, the polar ionosphere is significantly affected by the nature of the geophysical environment. In particular, the shape of the magnetic field is such as to connect, through the field lines, the polar ionosphere to the outermost regions of the magnetosphere. In this way, energetic particles of magnetospheric and/or solar origin can reach directly and undisturbed the ionosphere where they determine an increase in ionization. The direct entry of energetic particles (orders of tens of keV) may generate a severe radio waves absorption. This is the case of for *polar cap absorption* (PCA), which is due to the ionization produced by energetic protons (> 10 MeV) emitted by the Sun, usually during a solar flare (see section 1.1). During a PCA event, the ionospheric absorption is very intense and may lead to complete radio waves blackout in the HF band evenly localised over the entire polar cap (Hunsucker and Hargreaves, 2002).

The connection, through the field lines, between the ionosphere and the magnetosphere ensures that the behaviour and dynamics of the ionospheric plasma at high latitudes is a direct consequence of solar wind action. During periods of intense solar activity, the high latitude ionospheric layers (see section 1.3) differ markedly from the regions inhabiting the same altitudes at low and middle latitudes. The constant supply of 1-10 keV energetic electrons causes a considerable increase in the electronic density, which translates into a marked increase in conductivity, making such regions the most excited of the entire ionosphere. Consequently, in the high latitude ionospheric regions, roughly 40% of the energy goes into ionization while the remaining 60% translates into motion of the produced electrons (Hunsucker and Hargreaves, 2002).

1.3.2 AURORAL ELECTROJETS

Auroral Electrojets are two broad sheets of electric current that flow from noon toward midnight in the northern and southern auroral ovals (see section 1.2). The dawn-side current flows westward, creating a decrease in the magnetic field on the surface. The dusk-side current flows eastward and produces an increase in the magnetic field. They carry a total current of about 10^6 A (see e.g. Baumjohann and Treumann, 1996). Although this is the same order of magnitude as the total current carried by the ring current (see section 1.2.1), the auroral electrojets flowing at an altitude of approximately 120 kilometres in the E region (see section 1.3) of the ionosphere, cause the largest ground magnetic disturbance of all current system in the circumterrestrial environment. The disturbance field, usually about 100-1000 nT, can reach 3000 nT during the most violent magnetic storms (see section 4.1). In the E region, the collision rate between positive ions and atmospheric neutral particles is much larger than it is between electrons and neutrals. Higher in the ionosphere there are almost no collisions, while in the lower region there is little ionization. Because of the different collision rates, ions in the E region drift more slowly than electrons and thus create an electric current. At higher altitudes where equal numbers of positive and negative charges drift at the same rate, no current is produced because no net charge is transported. In the E region, positive charges moving backward relative to the drift create a current opposite to the drift.

The ionospheric drift results from magnetospheric convection (see section 1.4). Field lines with "feet" in the auroral ovals drift toward the dayside, so that the electrojet currents are toward the nightside. The electrojet currents flow at right angles to the sheets of ionospheric current connecting the field-aligned currents of Region 1 and Region 2 at the poleward and equatorward boundaries of the auroral

ovals (see section 1.2.1). As these currents are driven by the electric field produced by charge accumulation in the magnetosphere, they flow in the same direction as the electric field. The electrojet currents are thus at right angles to the electric field. Such a current is the Hall current (see section 1.3), which is always present when an electric field is applied to a conductor containing a magnetic field. The left panel in Figure 8 shows this current for the northern hemisphere. According to this figure, the westward electrojet flows in the afternoon sector and terminates in the pre-midnight region in correspondence with the *Harang discontinuity*, which is a region of electric field rotation. The auroral zone electric field is poleward directed in the afternoon and in the early evening sectors, pointing equatorward in the morning and in the post-midnight sectors. In the pre-midnight sector it rotates from north over west to south causing the *Harang discontinuity*. The eastward electrojet flows through the morning and midnight sector typically extending into the evening sector along the edge of the auroral oval where it as well as the eastward one diverges as upward field-aligned current.

The electrical conductivity parallel to the electric field in the Earth's ionosphere is referred to as the Pedersen conductivity (see section 1.3), and it is usually a factor of two less than the Hall conductivity perpendicular to the electric field. Consequently, the electrojet currents are actually stronger than the north-south ionospheric currents connecting the Region 1 and Region 2 currents. The Pedersen currents, shown in the right panel of Figure 8, flow northward in the westward electrojet and equatorward in the eastward one in the northern hemisphere providing a connection between the Region 1 and the Region 2 field-aligned currents. Inside the Harang discontinuity region, the evening and morning side Pedersen current circuits overlap, leading to three sheets of field-aligned currents (Baumjohann and Treumann, 1996).

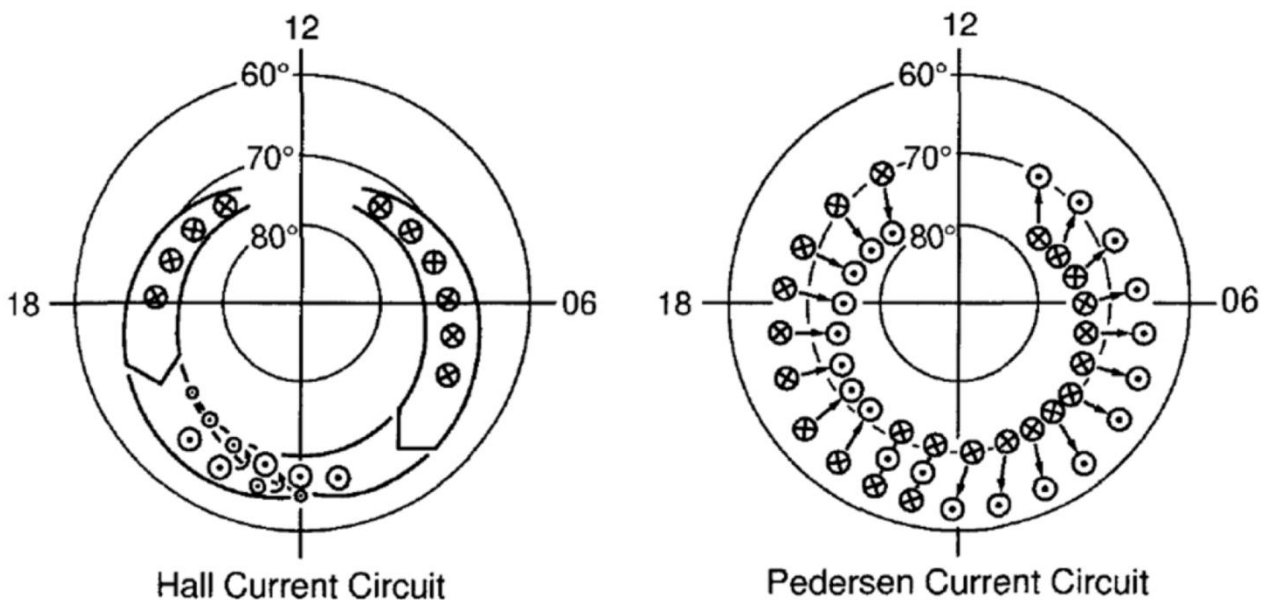


FIGURE 8: Representative scheme of the current systems for north hemisphere making up the auroral electrojets (taken from Baumjohann and Treumann, 1996)

1.4 CAUSES AND EFFECTS OF SPACE-EARTH COUPLING

The interactions between the circumterrestrial plasma including the solar wind are complex. Different models that attempt to explain the energy coupling processes between the solar wind and magnetospheric plasma have been proposed and they can be divided mainly into two different

categories called *magnetic reconnection* or field line merging and viscous-like interactions (see e.g. Dungey, 1961; Axford and Hines, 1961). The first interaction between the IMF and terrestrial field drives a tailward plasma flow across the polar caps and magnetospheric lobes. The viscous-like processes involves transfer of tangential momentum from the magnetosheath plasma through the magnetopause via viscosity generated by micro or macro instabilities, which drives a tailward plasma flow in the low-latitude boundary layers (Eastman et al, 1976). Both processes close the convection cycle with a sunward convection in the inner magnetosphere (see Figure 9).

Since this work is focused on high-latitude coupling processes, only the coupling between the IMF and the Earth's magnetic field, and its consequence on the high-latitude ionosphere-magnetosphere electrodynamics, will be discussed in this section.

1.4.1 SOLAR WIND-MAGNETOSPHERE INTERACTIONS

Since the IMF is *frozen into* the plasma of solar wind (see section 1.1), the IMF and the magnetospheric field are completely separated and no mass, energy or momentum transfer between them can occur. However, when the IMF is directed opposite to the magnetic field of the Earth, magnetic reconnection can occur, allowing plasma from the solar wind to penetrate into the magnetopause. As the Earth magnetic field is directed south-north, it is clear that it is the direction of the vertical component of the IMF, $B_{z,IMF}$, that mainly governs the reconnection process. In particular, when $B_{z,IMF} < 0$ reconnection on the dayside, equatorward of the polar cusp, occur and the magnetosphere is referred to as “open” (Lepping et al., 2003). When, instead, $B_{z,IMF} > 0$ a tailward polar cusp reconnection can occur (see e.g. Crooker, 1992; Chisham et al., 2004). In this case, the magnetosphere is referred to as “closed”.

As seen in Figure 9a, when $B_{z,IMF}$ is southward there are two reconnection points (N) where magnetic lines of different origins merge and allow exchanges of magnetic flux and plasma. When a southward oriented interplanetary magnetic line reaches the subsolar magnetopause, it connects to the Earth's field line and gives rise to two different lines with a fixed end on the ground and with the other extreme on the Sun (usually referred as open). The solar wind pushes these open lines, one for each hemisphere, in an anti-solar direction toward the magnetosphere night side where the open lines meet and reconnect. In this second reconnection point, a closed and stretched configuration occurs as well as an open line that is dragged away by the solar wind. The newly closed line relaxes carrying the plasma flow towards the Earth returning toward the dayside.

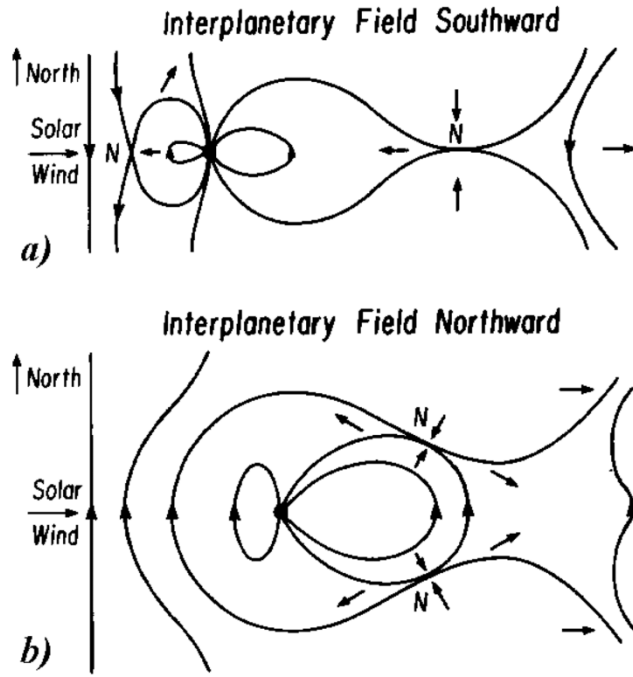


FIGURE 9: Sketch of the field lines in the noon-midnight meridian for the two cases: **a)** when the interplanetary magnetic field is antiparallel to the magnetic field near the nose of the magnetosphere and **b)** when it is parallel (Achilli, 2015).

When, on the other hand, the B_{zIMF} is northward, two reconnection points, one for each hemisphere, appears on the magnetospheric lobes (shown as N in Figure 9b). This configuration allows particles of solar origin to penetrate at high latitudes even in a so-called closed magnetosphere configuration.

1.4.2 LARGE SCALE ELECTRODYNAMICS OF THE POLAR IONOSPHERE

Since the solar wind plasma can be described, in an ideal MHD assumption, as *frozen into* the IMF, in the reference frame of solar wind plasma the electric field is null. However, for an observer on Earth an electric field exists and given by $\vec{E} = -\vec{u}_{sw} \times \vec{B}$, in which $-\vec{u}_{sw}$ is the solar wind velocity. Such electric field is directed from dawn-to-dusk and is perpendicular to \vec{B} . In a “closed” magnetosphere condition (see section 1.4.1), the electric field is excluded from the magnetosphere since the solar wind cannot penetrate through the magnetopause. When reconnection occurs (“open” magnetosphere condition, see section 1.4.1), this electric field maps down along the magnetic field lines to the polar cap ionosphere, causing the plasma to move with the $\vec{E} \times \vec{B}$ drift in the antisunward direction (Schunk and Nagy, 2009). At slightly lower latitudes, the electric field mapping to the ionosphere results directed equatorward on the dawn-side and poleward on the dusk-side implying a sunward plasma motion in the auroral oval.

Such electric fields generate a pair of convection cells governing the plasma circulation in the high latitude ionosphere. The size and orientation of these cells depend on the IMF direction. In particular, this dependence is not only related to the IMF north-south component B_{zIMF} but also due to the east-west component B_{yIMF} . The latter moves the reconnection point on the magnetosphere flanks, which modifies the symmetry of the cells. When $B_{yIMF} > 0$ the cell on the dusk-side is more extended, while for $B_{yIMF} < 0$ the most extended cell is on the dawn-side. Furthermore, when $B_{zIMF} > 0$ the number

of these cells can increase giving rise to a much more complex ionospheric plasma circulation model. Figure 10 shows this ionospheric convection pattern from above the North Pole.

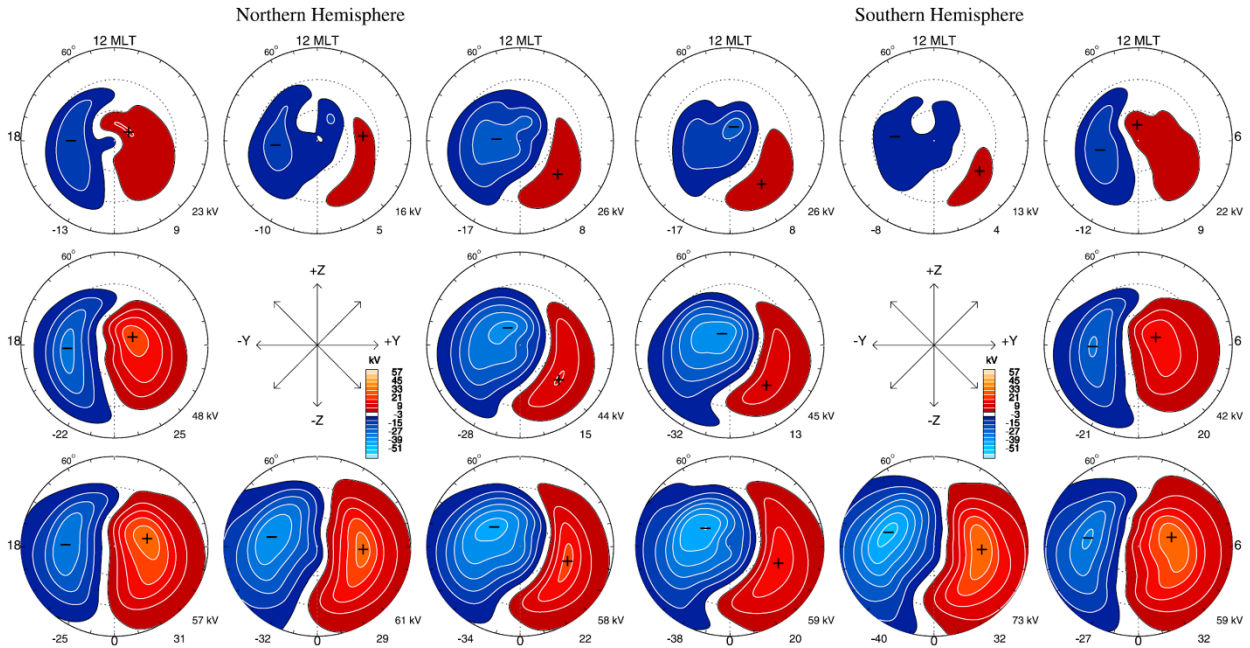


FIGURE 10: Statistical convection patterns sorted by IMF clock angle for $5 \text{ nT} < \mathbf{B}_T < 10 \text{ nT}$, neutral tilt (taken from Pettigrew et al 2010).

1.4.3 MAGNETOSPHERIC DYNAMICS

Before giving a detailed description of magnetospheric dynamics, triggered by the interaction between the magnetosphere and the solar wind, it is important to remember that since the Earth's magnetic field is a vector field, it can be characterized by a vector \mathbf{F} , which is a function of the time and of the observation point.

To represent the magnetic field, it is possible to introduce a reference system with an origin O (observation point) and with the x , y and z axis oriented as in Figure 11, in which the components of the field are defined as follows:

- X = component in the horizontal plane directed towards geographic North;
- Y = component in the horizontal plane directed towards geographic East;
- Z = vertical component defined positive when directed towards the interior of the Earth;
- H = total horizontal component whose intensity is equal to $\sqrt{X^2 + Y^2}$, oriented towards magnetic North;
- F = field total intensity;
- D = magnetic declination: angle between the H direction and the geographic meridian passing through the origin O , assumed positive towards East;

- I = magnetic inclination: angle between the direction of F and the horizontal plane, assumed positive when F is directed towards the interior of the Earth.

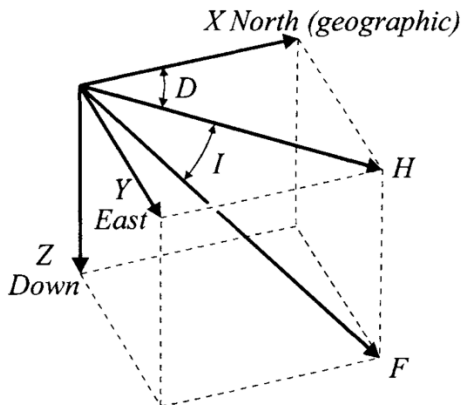


FIGURE 11: Representation of the Earth's magnetic field vector F and its components in a reference system with origin fixed at a point on the Earth's surface (figure taken from Merrill et al., 1996).

Magnetic storms

Magnetic storms are the main result of Sun-Earth interactions. They appear as a clear decrease in the horizontal component of the Earth's magnetic field (from tens nT up to hundred nT) caused by the intensification of the ring current (see section 1.2.1), which in turn is due to a long lasting condition of negative $B_{z,IMF}$. Such condition ensures magnetic reconnection and therefore transfer of energy from the solar wind to the magnetosphere (see section 1.4.1).

Magnetic storms can be classified as moderate or strong. They are defined as strong if the geomagnetic field depression exceeds 100 nT. For the development of strong storms the interplanetary field must be southward for at least 3 hours.

Interplanetary structures that can cause storms are CMEs (see section 1.1), and co-rotating interaction regions of solar wind. The latter originate from the interaction of solar wind fluxes traveling at different speeds. Usually, high-speed solar wind, reaching ≈ 800 km/s (Lepping et al., 2003), is emitted from coronal holes due to the magnetic field geometry characterising them. When fast solar wind interact with slower moving plasma, co-rotational interaction regions (CIR) are created.

Commonly, CMEs give rise to strong storms since they are characterized by a stable and intense (20-100 nT) IMF characterised by strong negative $B_{z,IMF}$ values. Moreover having high-speed they are able to produce a strong electric convection field. In most cases, they are preceded by an interplanetary shock (IPs, see section 1.1) and followed by a region of compressed gas. Co-rotating interaction regions originating from coronal holes (which remain on the Sun for more solar rotations) are related to recurring but moderate storms. In fact, CIRs show unstable and few negative $B_{z,IMF}$ values.

At the beginning a magnetic storm can be characterized by an abrupt increase of the magnetospheric field called *Sudden Impulse* (SI). SI is a field compression due to the arrival of the IP shock associated with an ICME (I for interplanetary) or a co-rotating interacting region. Such compression causes an increase in the magnetopause current (see section 1.2.1) that can be observed as an increase in the horizontal component of the equatorial Earth's field measured on the ground around noon near the

equator. This increase occurs over a few minutes and, if no negative $B_{z,IMF}$ values occur in the high temperature interplanetary structure after that, no storm develop (Villante and Piersanti, 2008).

The period over which the ring current increases, constitutes the *main phase* of the storm. The main phase can last many hours or even 1 day. The strong convection induced by the storm condition leads the magnetic field to return to its pre-storm values through the expulsion of plasmoids from the magnetospheric *tail*. Such process is known as *recovery phase*, which can last several days.

Magnetic substorm

Another important manifestation of the Sun-Earth interaction is the *magnetic substorm*, which consists of a rapid energy release in the magnetotail due to the reconfiguration of the magnetospheric field, called *dipolarization*. The latter is generally interpreted as a sudden decrease in the intensity of the current sheet, which involves the stretching of the innermost field lines (Lui, 1996).

The variability of the north-south component of the IMF allows the input of energy in the magnetosphere during periods in which there is reconnection between the IMF and the Earth's magnetic field. During reconnection periods the solar wind carries the sub-solar reconnected magnetic flow towards the magnetotail (see section 1.4.1) in which the field intensifies and compresses. Usually, such a condition causes plasma tearing instability, which can therefore favour reconnection conditions in the magnetospheric tail (Russell, 1986). Reconnection in the magnetotail generates a closed and stretched field line, which relaxes and shortens carrying plasma with it frozen. This generates a convective plasma motion from the tail towards Earth. Such plasma can reach the ionosphere through the field-aligned currents (see section 1.2.1) intensifying its ionization. In fact, this is one of the processes behind the spectacular phenomenon of the *polar aurorae*. *Polar aurorae* occur also during storms due to the particle precipitation associated with the solar structure hitting the Earth's magnetosphere.

A polar aurora is an emission of visible radiation (0.4-0.7 μm) due to the electronic excitation of neutral atmospheric atoms caused by collisions with energetic particles traveling along the field lines. The distribution of the maximum auroral activity, as a function of the magnetic latitude, identifies annular shape regions known as auroral oval (see section 1.2). The auroral ovals, one for each hemisphere, during periods of quiet or moderate magnetic activity, are found between 67° magnetic latitude in the dayside, and 77° of magnetic latitude in the nightside. In the presence of intense magnetic activity the auroral ovals expand towards the equator, covering larger areas (see Figure 12).

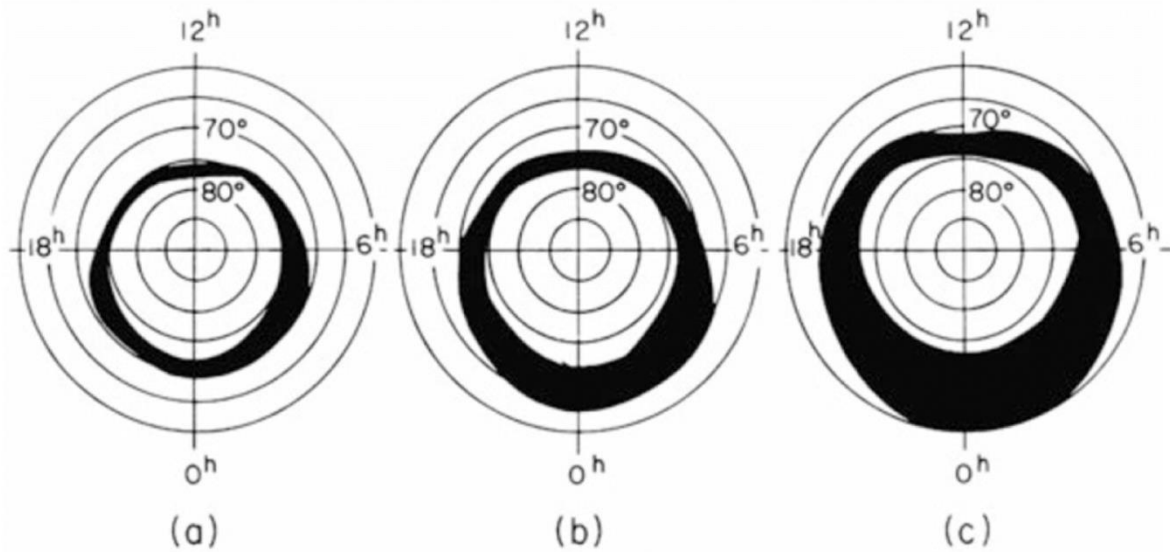


FIGURE 12: Auroral ovals under different electromagnetic disturbance conditions: (a) quiet condition; (b) average disturbed condition; (c) strong disturbed condition (taken from Brekke, 2012).

1.4.4 GEOMAGNETIC ACTIVITY INDICES

To monitor the Earth's magnetic field response (both globally and locally) to perturbations coming from the Sun, *geomagnetic indices* are used (Mayaud, 1980; Perrone and De Franceschi, 1998). These indices, derived by continuous and systematic recordings of the Earth's magnetic field components, allow the description of variations of the magnetic field under quiet and perturbed conditions. They can be easily derived starting from specific parameters correlated with the phenomenon producing the perturbation.

As the aim of this work is to understand the solar wind-magnetosphere-ionosphere coupling physical conditions leading to scintillations on GNSS signals in the high latitude ionosphere, the following indices have been chosen as significant and a brief description is given below.

Auroral indices

The auroral activity indices are designed to provide a global, quantitative measure of the auroral zone magnetic activity. In particular, there are three indices: the *AE* (Auroral Electrojet) index, the *AU* (Auroral Upper) index and the *AL* (Auroral Lower) index.

The *AE* index, introduced by Davis and Sugiura (1966) as a measure of the activity of auroral electrojets, is obtained from the variations of the Earth's magnetic field horizontal component (H , see section 1.4.3) measured by 10-13 stations in the auroral zone of the northern hemisphere. To obtain this index the monthly averages for the 5 quietest days are subtracted from the 1-minute sampling data of each station. Then all the curves are shown in a single chart. The highest values constitute the *AU* index, which therefore represents the maximum positive disturbance of the auroral electrojets. In particular, this is related to the eastward electrojet (see section 1.3.2), which during period of negative $B_{z,IMF}$ intensifies with the field-aligned currents connected with the ring current. The lowest values constitute the *AL* index, which represents the maximum negative disturbance. This is linked to the westward electrojet (see section 1.3.2), which during period of negative $B_{z,IMF}$ intensifies with the field-aligned currents connected with the tail currents system. The *AE* index is thus defined as the

difference between the *AU* and the *AL* indices. The World Data Center for Geomagnetism of Kyoto (<http://wdc.kugi.kyoto-u.ac.jp/>) provides the daily variations of such indices.

Disturbance storm-time (*Dst*) index

The *Dst* index is a measure of the horizontal component of the Earth's magnetic field, providing a monitor of a magnetic storm (see section 1.4.3) on a global scale. The index is obtained from the *H* component measured by 4 almost equally spaced stations placed at low latitude, far from the auroral electrojets. Also in this case, the monthly averages for the 5 quietest days are subtracted from the hourly values of each station and the average of the 4 station data set is then computed. However, since the 4 stations are not equally spaced, this value is divided by the cosines averages of the stations latitudes according to:

$$Dst = \frac{\Delta H}{\cos \varphi} \quad (1.3)$$

The *Dst* is an hourly index, the *SYM-H* index is used for a higher resolution. This index corresponds to 1-minute sampling of the *Dst* index but is derived from 6 stations. The World Data Center for Geomagnetism of Kyoto (<http://wdc.kugi.kyoto-u.ac.jp/>) provides the daily variations of such indices.

Polar Cap indices

The Polar Cap (*PC*) index introduced by Troshichev and Andrezen (1985) is a fifteen-minute index providing a measure of the transpolar ionospheric current intensity. This current is related to the polar cap antisunward ionospheric convection driven by the dawn-dusk electric field, which is generated by the solar wind. The *PC* index is thus characteristic of the polar cap magnetic activity generated by geoeffective solar wind parameters such as the southward component of the IMF (B_{zIMF}), the azimuthal component of the IMF (B_{yIMF}), and the solar wind velocity. Thus, the index constitutes a quantitative estimate of geomagnetic activity at polar latitudes and serves as a proxy for energy that enters the magnetosphere during solar wind-magnetosphere coupling. The index is derived from magnetic data from two stations Thule and Vostok located in the northern (*PCN*) and southern (*PCS*) near-pole regions. The daily variation of such indices can be found at <http://pcindex.org/>.

1.4.5 IRREGULARITIES OF THE POLAR IONOSPHERE

Due to the Earth's magnetic field geometry, the polar ionosphere is considerably more complex than in low and middle latitudes. In fact, solar wind-magnetosphere-ionosphere coupling ensures that the behaviour and dynamics of the ionospheric plasma at high latitudes is largely controlled by solar wind action (see sections 1.3.1, 1.3.2 and 1.4.1-3). This means that due to solar wind variability the polar ionosphere exhibits different convection patterns in which plasma irregularities can form. The latter are plasma regions, delimited in space and time, in which the free electric charge concentration is clearly different from the surrounding environment. Such anomalies appear as local increases or decreases in the ionospheric plasma density and as turbulent plasma fluctuations. The turbulent character of these structures implies their dynamics have a stochastic and multi-scale behaviour that does not allow, in a rigorous treatment, the decoupling of space and time.

The importance of ionospheric irregularities is related to their ability to generate fluctuations in the ionospheric refractive index (see section 1.3) and therefore to their ability to degrade trans-atmospheric signals on which some technological systems rely on. The abrupt variations in the refractive index have significant effects on radio waves that propagate in the ionosphere, especially in the HF, VHF and UHF bands. However, they can affect also the radio propagation in L-band signals, ranging frequencies between 100 MHz and 4 GHz (see Figure 13). They give rise, for example, to refraction, reflection, absorption, time delay phenomena as well as Doppler sudden shifts, and randomly, amplitude and/or phase changes of the radio waves passing through the ionosphere.

Although plasma irregularities are a common feature of the ionosphere at all latitudes, especially in concomitance with maxima in solar activity, these are more frequent in the polar and in equatorial regions (Figure 13, showing the global scintillation (see Chapter 2) activity during solar maximum (left) and solar minimum (right)). In these regions, the magnetic field geometry and the solar irradiance favours the development of irregularities, sometimes even recurring.

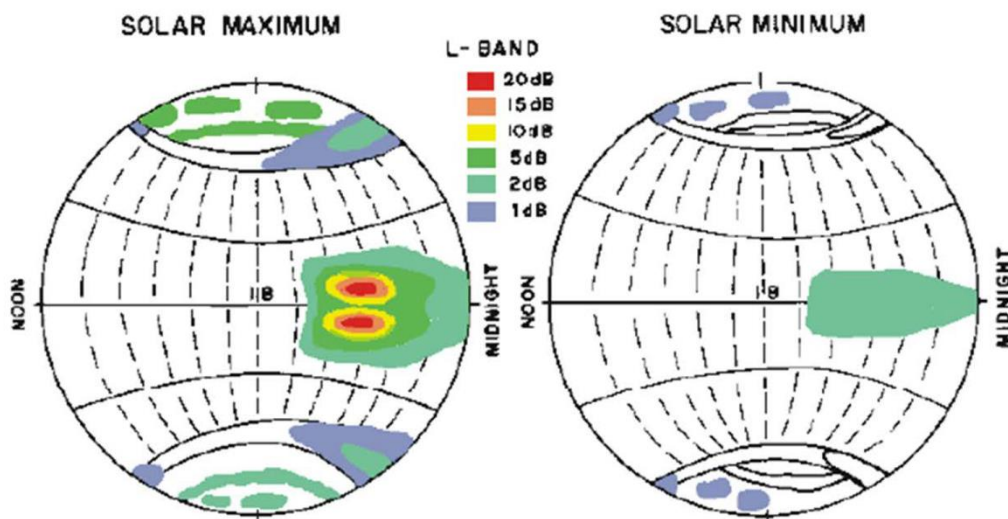


FIGURE 13: Global variation of irregularities causing scintillations during solar maximum and solar minimum. Different colours refer to different noise thresholds on L-band signals (Basu et al., 1988).

At high latitudes, the regions with the highest incidence of irregularity are cusps, auroral ovals and polar caps (Kersley et al., 1988; Basu et al., 1990; MacDougall, 1990a, 1990b). In such regions, due to the complex dynamics driven by the solar wind-magnetosphere-ionosphere coupling, irregularities have spatial scales ranging from tens of kilometres to few meters (see e.g. Dyson et al., 1974; Phelps and Sagalyn, 1976; Kelley et al., 1980; Tsunoda, 1988; Moen et al., 2012).

According to their spatial dimension, it is possible to group such irregularities into two large ensembles. The first includes the *enhancements*, which extend for tens or even hundreds kilometres, and are observable through incoherent scatter radar and other ionospheric techniques. The second includes irregularities extending less than 10 km, which produce radio wave amplitude and phase oscillations on the signals passing through the ionosphere (see section 2.1). However, this distinction cannot be considered extremely rigorous because of the high variability of the plasma dynamics that characterize the polar regions. For example, during the passage of plasma in the cusp regions, a large irregularity may fragment into smaller irregularities as well as small-scale irregularities, following

the plasma motion inside the convective cells (see section 1.4.2), which may cluster to form one or more irregularities of greater dimensions.

Enhancements are ionospheric irregularities with spatial dimensions ranging from 50 to 1000 km (see e.g. Hunsucker and Hargreaves, 2002). They have high electron density, which is comparable to the diurnal mid-latitude ionosphere, even when observed during the polar night. Such irregularities are named *patches* when they occur within the polar cap.

Patches take this name due to their patchy appearance in 630 nm images (Carlson, 2012). They usually appear during the polar night in concomitance with perturbation coming from the Sun for $B_{zIMF} < 0$ (see e.g. Fejer and Kelley, 1980; Tsunoda, 1988; De Franceschi et al., 2008; Tiwari et al., 2012). They have two times (or more) the density of the F region background in which they occur (Crowley, 1996) and extend from 200 to 1000 km. Patches are driven across the dayside polar caps into the nightside with speeds on the order of 300–1000 m/s. In the return flow on the nightside, the patches are called *blobs* (Tsunoda, 1988). Although many different mechanisms for their formation have been proposed, such as changes in the convection pattern (e.g. Anderson et al., 1988; Rodger et al., 1994), transient magnetic reconnection (Lockwood and Carlson, 1992) or reconnection driven pulsed convection (Moen et al., 2006), there is no complete agreement on which is the most effective. It is known that when $B_{zIMF} > 0$ patches form thin strips aligned according to the noon-midnight direction (see e.g. Sandholt et al. 2002), with high electronic density (about 5-8 times greater than the background), which generate a slow drift in the dawn-dusk direction.

Small-scale irregularities (<10 km), on the other hand, seem to be closely linked to plasma dynamics and variations in the solar wind flow. The diffractive effects connected with them seem to occur mainly in correspondence with sudden electron density variations occurring, for example, at the edges of the patches and/or the convective cells (Mitchell et al., 2005; Prikryl et al., 2011, Spogli et al., 2013). Usually they occur in the cusp regions, in the auroral zones and during the night-time. Small-scale irregularities are the cause of ionospheric scintillations and are extensively described in the following section.

CHAPTER 2

THE IONOSPHERIC SCINTILLATION

Similarly to what is observed on the brightness of the stars in the optical band, ionospheric scintillation is defined as a rapid and random fluctuation in the received amplitude and/or phase of radio waves passing through the ionosphere (Yeh and Liu, 1982; Kintner et al., 2007). This phenomenon occurs when a radio frequency signal (typically in a range of frequencies between 100 MHz and 4 GHz) in the form of a plane wave crosses an ionospheric density irregularity (1.4.5). In crossing an irregularity, the plane wave experiences diffractive and refractive effects (see e.g. Kintner et al., 2007). Due to diffraction, produced by ionospheric irregularities near the first Fresnel radius, the impinging plane electromagnetic wave enters the ionosphere with a spatially uniform phase and exits the ionosphere with a spatially irregular phase. These irregular phases may combine either constructively or destructively giving rise to amplitude and phase scintillations. For refraction a plane wave remains a plane wave but the received phase changes because the electromagnetic wave enters a medium of either increased or decreased phase velocity (see e.g. Wernik et al., 2003; Kintner et al., 2007).

Initial studies of ionospheric scintillation were primarily in the VHF and UHF radio bands and focused on scintillations effects on communication signals (see e.g. Whitney and Basu, 1977). With the introduction of L-band communication links on satellites, scintillations were investigated at higher frequencies, including those used by the Global Positioning System (GPS) satellites (see e.g. Basu et al., 1980; Aarons and Basu, 1994). This a cause of growing concern particularly to those new application, which are life-critical such as GPS-aided aviation (Dehel et al., 2001; Conker et al., 2003). Amplitude scintillation directly affects the signal to noise ratio (C/No) of signals in a GPS receiver, as well as the noise levels in code and phase measurements. When sufficiently severe the received GPS signal intensity from a given satellite drops below the receiver tracking threshold, causing loss of lock for that satellite, and hence the need to re-acquire the GPS signal(s). This results in reduced accuracy navigation solutions, data loss and cycle slips. Phase scintillation if sufficiently severe, may stress phase-lock loops in GPS receivers resulting in a loss of phase lock.

Scintillation studies are important to enable the prediction of positioning and communication system degradation. However, since scintillation theory relates the observed signal statistics to statistics of the ionospheric electron density fluctuations (see e.g. Yeh and Liu, 1982; Bhattacharyya et al., 1992; Yeh and Wernik, 1993; Basu and Basu, 1993), scintillation studies can be used to investigate the behaviour of electron density irregularities in the ionosphere. The aim of such studies is to solve the propagation of radio waves in a random media and are based on the phase-screen model, which is the most studied scintillation theory (see e.g. Booker et al., 1950; Bramley, 1977; Rino, 1979a, b; Carrano et al., 2012). In the phase-screen model an ionospheric infinitely thin layer, hosting irregularities, is assumed able to induce phase perturbations in the radio wave. In the weak scattering approximation, only the phase is affected during wave propagation through the irregularity layer due to the random fluctuation in refractive index. After passing through the screen, as the wave propagates to the ground, the induced phase perturbations evolve producing amplitude and phase scintillations according to Huygens's principle.

The spectra of amplitude and phase deviation are given by (Kintner et al., 2007):

$$\begin{aligned}\Phi_I(q) &= \Phi_\phi(q) \sin^2\left(\frac{q^2 r_F^2}{8\pi}\right) \\ \Phi_p(q) &= \Phi_\phi(q) \cos^2\left(\frac{q^2 r_F^2}{8\pi}\right)\end{aligned}\tag{2.1}$$

in which q is the horizontal wave number of the phase fluctuation across the screen, $\Phi_\phi(q)$ is the power spectrum of the wave phase exciting the screen, which is linearly related to the irregularity density spectrum for small changes in phase, $\Phi_I(q)$ and $\Phi_p(q)$ are the Fourier transform of the intensity and phase autocorrelation function, respectively. $r_F = \sqrt{2\lambda d}$ is the radius of the first Fresnel zone in which λ is the incident signal wavelength, while d is the distance from the phase screen to the receiver. In (2.1), describing the spectrum of amplitude deviation, the term $\sin^2\left(\frac{q^2 r_F^2}{8\pi}\right)$, known as the Fresnel filtering function, provides, to first order, an upper limit on the irregularity scale size. In particular, the upper limit of the scale size, known as the Fresnel radius r_F , occurs when the \sin^2 term goes to one or when the argument is equal to $(2n-1)\pi/2$ radian. In the case of GPS signals, transmitted at L1 = 1575.42 MHz frequency, the radius of the first Fresnel zone is about 365 m assuming an irregularity layer altitude of 350 km ($d=350$ km) and a signal ray path elevation of 90° .

Unlike amplitude scintillations, phase scintillations have a maximum at $q=0$ and the next local maxima are when the argument becomes $n\pi$ radians due to the \cos^2 term. Because the one-dimensional phase spectrum at the phase-screen typically has the form $\Phi_\phi(q) \sim q^{-n}$ in which n is of order 2, the majority of the phase fluctuation power is found at small q .

Equation (2.1), relating the radio wave spectra with the spectra of the electron density fluctuation, can be applied only for one-dimensional weak scattering approximation. For strong scattering both phase and amplitude of the incident plane wave are altered in crossing the phase-screen. Consideration of these more complex environments can be found in the work of Rino and Fremouw (1977) and Rino (1979a, b).

2.1 GLOBAL NAVIGATION SATELLITE SYSTEM (GNSS)

Global Navigation Satellite System (GNSS) is a general term describing any satellite constellation that provides positioning, navigation and timing (PNT) services on a global or regional basis. The performance of GNSS is assessed using four criteria: the accuracy, the integrity the continuity and the availability. The accuracy ensures that the differences between a measured and real position, a measured and real speed or a measured and real time are as small as possible. The integrity consists in the system's ability to provide timely warnings to users when the system should not be used for navigation. The continuity is the system's ability to function without interruption; while the availability is the percentage of time in which a signal fulfils the above accuracy, integrity and continuity criteria.

Generally, three segments compose a GNSS system:

- the *space segment* consisting of the satellite constellation. Its orbital features allow receiving signals by at least four satellites at the same time for any time of day and from any point on the Earth's surface.
- The *control segment* consists of the ground station network, whose position is known with great precision. It has the task to monitor the whole system and ensures its operation. In fact, the control segment provides, on a regular basis, the navigational update to each satellite, including the synchronization of the atomic clocks, the adjustment of the ephemeris of each satellite's internal orbital model and other information like inputs on the space weather conditions.
- The *user segment*, which consist of all civilian and military users able to receive GNSS signals determining their coordinates in a suitable reference system.

Each GNSS satellite transmits a carrier wave, the ranging code (i.e. a binary sequence to univocally identify the satellite) and the navigation message, in which the time information (time-of-week and week number) is carried. The GNSS receiver generates its own code and compares it with the transmitted code, in order to measure the difference between the transmission time and the reception time of the signal.

GPS is the first and best known GNSS. GPS was developed in the 1970s by the US Department of Defence (DoD). The space segment of the GPS architecture is a constellation of 24-28 satellites in medium circular Earth orbit with radius of 26,600 km and approximately 55° inclination. They are in six orbital planes whose ascending nodes (angles along the equator from a reference point to the orbit intersection) are equally spaced by 60°. Each satellite of this constellation makes two complete orbits each sidereal day, repeating the same ground track each day. It transmits at exactly two frequencies: L1=1575.42 MHz and L2=1227.6 MHz and the satellite signals are separated by modulating each carrier with a pseudorandom noise (PRN) code unique to each satellite.

In addition to the GPS (currently composing 32 satellites), three other global satellite navigation systems have been developed:

- The Russian GLObal NAVigation Satellite System (GLONASS) is a constellation of 24 satellites located in the middle circular orbit at 19,100 km with a 64.8° inclination and a period of 11 hours and 15 minutes. This constellation is the second navigational system in operation with global coverage providing an alternative to GPS especially in built-up areas where the view to some GPS satellites is obscured by buildings and at high latitudes.
- The European GALILEO has 24 operational satellites plus six spares, at an altitude of about 23.222 km. These are arranged in three orbit planes having 56° inclination and ascending nodes separated by 120° longitude. It is foreseen to be completed and fully operational by 2020;
- The Chinese BeiDou Navigation Satellite System (BDS), which consist of two separate satellite constellations. The first BeiDou system, also known as BeiDou-1, consists of three satellites, which offered limited coverage and navigation services, mainly for users in China and neighbouring regions. The second-generation system, officially called the BeiDou Navigation Satellite System (BDS) and known as COMPASS, became operational in December 2011 with a partial constellation of 10 satellites in orbit offering services to customers in the Asia-Pacific region. In 2015, China started the build-up of the third

generation BDS to consist of 35 satellites and expected to provide global services upon completion in 2020.

In addition to these systems that cover the whole globe, regional navigation satellites systems exist (RNSS), like the Japanese Quasi-Zenith Satellite System (QZSS) and the Indian Regional Navigation Satellite System (IRNSS).

2.2 GNSS RECEIVERS FOR IONOSPHERIC STUDIES

The GNSS satellite signals are excellent for the study and characterization of ionospheric irregularities. This is due to two fundamental reasons. The first is that such signals are continuously available, so they provide simultaneous information about different sectors of the ionosphere. Furthermore, since they are in a range of frequencies between 100 MHz and 4 GHz, their signals are sensitive to phase and amplitude scintillations when they pass through ionospheric irregularities (see e.g. Aarons, 1997; Wernik et al., 2003; Kintner et al., 2007). GNSS measurements have been chosen as the cornerstone of this investigation.

The acquisition of ionospheric measurements deduced from GNSS signals requires the use of special receivers. They are usually single or dual frequency receivers specifically designed to monitor ionospheric scintillation in real time. Such receivers have wide-bandwidth tracking loops to maintain the lock during intervals of strong ionospheric scintillation even if loss of lock on single or multiple satellites can still occur during extreme events, requiring the re-acquisition of the signal(s). Another important feature of such receivers is that they sample the signal at a rate of 50 Hz to calculate the scintillation statistics. Such sampling allows measure of very fast variations of the signal phase and amplitude on the carrier frequency, which generally corresponds to L1 (1575.42 MHz).

The primary purpose of GNSS receivers for ionospheric studies is to collect ionospheric scintillation statistics for all visible satellites and store these binary data logs (named ISMR) on the receiver controller hard disk for post processing. These receivers are also equipped with control software that can be programmed to collect the data logs generated every 1 minute. Alternatively, raw phase and amplitude data at 0.02 s temporal resolution (50 Hz) and code/carrier divergence at 1 s (1 Hz) can be obtained from the receiver. These data can be used to reconstruct the scintillation indices (see section 2.2.1) from raw data. The possibility to program the receiver's control software allows the user to modify the parameters used in the derivation of scintillation indices, such as the de-trending and the filter cut-off parameters (see section 2.3).

The investigation proposed in this work is based on GNSS observations recorded by two kinds of receivers:

- the GPS Ionospheric Scintillation and TEC Monitor (GISTM, Van Dierendonk et al. 1993) system and in particular the GSV4004 model, which consist of an L1/L2 GPS antenna, a dual-frequency GPS receiver (NovAtel's Euro-3M with modified firmware), and a low phase noise oven-controlled crystal oscillator (OCXO), housed in NovAtel's EuroPak-3M enclosure. The OCXO is required for monitoring phase scintillation.
- The Septentrio PolaRxS Ionospheric Scintillation Monitoring Receiver (ISMR), which is a multi-frequency, multi-constellation receiver dedicated to ionospheric monitoring and space weather applications (Bougard et al., 2011, Alfonsi et al., 2016 and references therein). In

particular, the ISMR is able to provide access to ionospheric delay and related measurements from not only the United States GPS system of navigation satellites, but also from the Russian GLONASS and the European Galileo satellites. The PolaRxS incorporates a state-of-the-art triple-frequency receiver engine and an ultra-low noise OXCO frequency reference in a rugged housing.

The selected network for the investigation proposed in this thesis consists of receivers located in both the Arctic and Antarctica. Specifically, Arctic receivers are located at Eureka, Resolute Bay and at Ny-Ålesund stations, while Antarctic receivers are located at Concordia, Mario Zucchelli (Terra Nova Bay), Zhongshan and SANAE stations. They are managed by the Canadian network CHAIN (Canadian High Arctic Ionospheric Network, Jayachandran et al. 2009), INGV (Istituto Nazionale di Geofisica e Vulcanologia; De Franceschi et al., 2006), IGGCAS (Institute of Geology and Geophysics, Chinese Academy of Sciences) and by SANSA (South African National Space Agency).

TABLE 1: Locations, identifiers, geographic and geomagnetic coordinates (CGLat and CGLon) of the GNSS receivers used in this study.

	Location	Station ID	Owner	Latitude	Longitude	CGLat	CGLon
Arctic	Eureka	EURC	CHAIN	79.99 °N	274.10 °E	87.41 °N	342.32 °E
	Resolute Bay	RESC	CHAIN	74.75 °N	265.00 °E	82.45 °N	326.10 °E
	Ny- Ålesund 0	NYA0	INGV	78.92 °N	11.98 °E	76.54 °N	108.79 °E
Antarctica	Concordia	DMC0	INGV	75.10 °S	123.35 °E	89.05 °S	55.27 °E
	Mario Zucchelli	BTN0	INGV	74.41 °S	164.10 °E	79.80 °S	305.12 °E
	Zhongshan	ZSGN	IGGCAS	69.37 °S	76.37 °E	75.59 °S	102.53 °E
	SANAE	SNA0	SANSA	71.67 °S	2.84 °W	61.93 °S	44.73 °E

Table 1 reports geographic and geomagnetic coordinates of the sites, together with the receiver identifiers, locations and station owners. Figure 14 shows the geographic locations of the receivers.



FIGURE 14: Geographic locations of the selected receivers. On the top the locations of Eureka (EURC), Resolute Bay (RESC) and Ny-Ålesund (NYA0) stations. On the bottom the location of Concordia (DMC0), Mario Zucchelli (BTN0), Zhongshan (ZSGN) and SANAE (SNA0) stations.

2.2.1. SCINTILLATION INDICES

The strength of phase and amplitude scintillation on GNSS signals is conventionally quantified by the phase (σ_ϕ) and amplitude (S_4) scintillation indices (Van Dierendonck, 1993). The phase scintillation index (σ_ϕ), which corresponds to the standard deviation of the carrier phase in radians, from which the trend ascribed to the satellite drift has been eliminated, is defined as:

$$\sigma_\phi = \sqrt{\langle \phi^2 \rangle - \langle \phi \rangle^2} \quad (2.2)$$

In equation (2.2), $\langle \rangle$ denotes the expected value while ϕ represents the detrended carrier phase. The standard deviation is computed over periods of 1, 3, 10, 30 and 60 seconds every 60 seconds. This means that for every minute five values are stored in the ISMR (see section 2.2) data log along with the time tag. For the investigation proposed in this thesis, the σ_ϕ of 60 seconds is used as the GNSS phase scintillation index.

The amplitude scintillation index (S_4) is defined as the ratio of the standard deviation of the received signal power to the mean signal power over a time period, which is nominally 60 seconds even if it could be arbitrarily chosen longer or shorter. The total S_4 , which includes the thermal noise effects, is:

$$S_{4tot} = \sqrt{\frac{\langle I^2 \rangle - \langle I \rangle^2}{\langle I \rangle^2}} \quad (2.3)$$

where $\langle \rangle$ denotes the expected value over the selected time period and I is the received signal power. Equation (2.4) describes the correction to the S_4 value due to the thermal noise

$$S_{4corr} = \sqrt{\frac{100}{S/N_0} \left(1 + \frac{500}{19S/N_0} \right)} \quad (2.4)$$

in which S/N_0 is the signal-to-noise ratio. Subtracting the correction from the total S_4 value yields the amplitude scintillation index corrected for the thermal noise given by:

$$S_4 = \sqrt{S_{4tot}^2 - S_{4corr}^2} \quad (2.5)$$

It is important to notice that if the argument under the square root becomes negative, the S_4 value is set to zero. Also in this case, the S_4 of 60 seconds has been selected as the GNSS amplitude scintillation index for this investigation. From equation (2.5) the noise floor is filtered out from the results related to the amplitude scintillations.

Both indices here considered are computed on L1 carrier frequency. In principle they can be derived also from other frequencies as L2C and L5 (the new GPS frequency; see Venkatesh Babu and Lakshmi Narayana, 2012), but this is out of the scope of the present work.

2.2.2. TOTAL ELECTRON CONTENT AND ITS GRADIENTS

Due to the dispersive nature of the ionosphere, it is possible to calculate the Total Electron Content (TEC) starting from the code or carrier phase measurements provided by GNSS receivers on different frequencies. TEC is derived as the total number of free electrons in a cylinder with cross section of 1 m² and height equal to the slant signal path. It is defined as the integral of the electron density along the GNSS signal ray path, according to:

$$TEC = \int_{satellite}^{receiver} N_e ds \quad (2.6)$$

This quantity, measured in Total Electron Content Unit (TECU, where 1 TECU = 10¹⁶ electrons/m²), can be calculated along each slant path according to:

$$TEC = \frac{1}{40.3} \left(\frac{f_1 f_2}{f_1 - f_2} \right) (P_2 - P_1) - \varepsilon \quad (2.7)$$

This equation describes the so-called *geometry-free combination* in which f_1 and f_2 are the two carrier frequencies of the transmitted signal, P_1 and P_2 are the corresponding pseudoranges (satellite-receiver optical path), while ε represents all the frequency-dependent biases induced by the receiver, the satellite and the environment in which the measurement is carried out. As each TEC value obtained

from equation (2.7) is the electron content along the satellite-receiver path, it is called *slant TEC* (*sTEC*). In this way, for each satellite and for each period, TEC measurements take place at different elevation angles and are related to different ionospheric sectors. In order to obtain TEC values independent on the geometry of the GNSS constellation and on the receiver's network, *sTEC* must be converted to *vertical TEC* (*vTEC*). The simplest way to transform *sTEC* into *vTEC* is to assume the ionosphere as a single thin ionized layer, located between 300 and 500 km above the Earth's surface, where the electron density maximizes. According to this assumption, *vTEC* can be obtained by using the transformation:

$$vTEC = sTEC \cos(\chi') \quad (2.8)$$

in which χ' it is the complementary angle to the zenith, as shown in Figure 15.

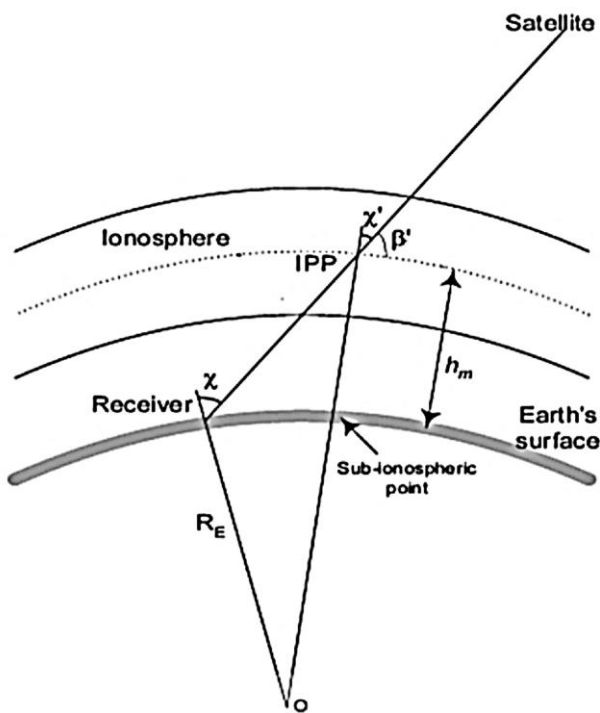


FIGURE 15: Single layer ionospheric model.

As mentioned in sections 2.2 and 2.2.1, the control software integrated into the GNSS receivers for ionospheric studies allows the automatic calculation of the scintillation indices S_4 and σ_ϕ over different time windows (1, 3, 10, 30 and 60 seconds). The receiver is also able to provide and collect TEC and its rate of TEC change (ROT) values computed every 15 seconds from combined L1 and L2 pseudorange and carrier phase measurements, respectively. Specifically, TEC values are obtained, according to equation (2.7), by pseudorange measurements only, while ROT is computed from carrier phase measurements only.

TEC from pseudorange measurements suffer from a larger error compared with those from carrier phase measurements. In principle, this should let the choice fall on the use of the carrier phase for TEC estimation. However, carrier phase measurements have the issue of phase-ambiguity that is

difficult to solve in real-time. This is the main reason why TEC is provided by the receiver from pseudorange measurements. However, phase ambiguity is not a problem for ROT:

$$ROT = \frac{TEC_{t_k}^i - TEC_{t_{k-1}}^i}{t_k - t_{k-1}} \quad (2.9)$$

in which i is the satellite index while t_k is an epoch time. Thus, in equation (2.9), phase ambiguity, frequency-dependent biases and environmental errors (equation (2.7)) cancel out, leading to a more accurate determination of ROT compared with TEC. In addition, since ROT related to the Nyquist period (Zou & Wang 2009), it allows the retrieving of information about the irregularities scale length involved in scintillations. The irregularities scale length corresponding to the Nyquist period is given by the vector sum of the components of the ionospheric projection of the satellite motion and the irregularities drift velocity in the direction perpendicular to the GPS ray path. As at high latitudes, experimental evidence shows that plasma convection velocities span a range between 100 m/s and 1 km/s (Ruohoniemi and Greenwald 2005), the irregularities scale length, sampled by ROT, varies from few to tens of kilometres (Basu et al. 1999). Hence, from a comparison ROT excursions and the scintillations occurrence, and bearing in mind constrain derived from the Fresnel filtering, it is possible to retrieve information about the irregularities scale sizes in which the ionospheric plasma is fragmented (Alfonsi et al., 2011).

2.3 METHOD TO TREAT TEC AND SCINTILLATION DATA

The scintillation statistics acquired by the control software of the selected receivers for the proposed investigation is calculated (with the exception of the TEC and ROT values, see section 2.2.2) for all the available signal frequencies transmitted by the satellites and along the slant path connecting the receiver to the satellite. Hence, in order to study the relationship between TEC, its spatial gradients and ionospheric scintillation it is necessary to reduce the impact of the satellite-receiver geometry on the scintillation measurements. The scintillation indices (see section 2.2.1) are projected to the vertical according to:

$$\sigma_{\phi}^{vert} = \frac{\sigma_{\phi}^{slant}}{F(\alpha_{elev})^a} \quad (2.10)$$

$$S_4^{vert} = \frac{S_4^{slant}}{F(\alpha_{elev})^b} \quad (2.11)$$

where σ_{ϕ}^{slant} and S_4^{slant} are the indices directly provided by the receiver at a given elevation angle along the slant path, while $F(\alpha_{elev})$ is the obliquity factor defined as (Mannucci et al. 1993):

$$F(\alpha_{elev}) = \frac{1}{\sqrt{1 - \left(\frac{R_e \cos \alpha_{elev}}{R_e + H_{IPP}} \right)^2}} \quad (2.12)$$

In equation (2.12), R_e is the Earth's radius and H_{IPP} is the height of the Ionospheric Piercing Point (IPP), which in the present investigation is assumed to be located at 350 km altitude. According to Rino (1979a, 1979b) and as described by Spogli et al. (2009), the exponent a has been chosen equal to 0.5 in (2.10) and the exponent b has been chosen equal to 0.9 in (2.11). For a critical discussion of the use of vertical scintillation indices in weak and strong scattering regimes, see Spogli et al., (2013b).

In order to reduce the impact of non-scintillation related tracking errors (such as multipath) a mask of 20° on the elevation angle of the satellites has been applied on scintillation data used in this work. In fact, although the 50 Hz sampling frequency adopted by GNSS receivers is useful to investigate transient ionospheric effects, it cannot distinguish the scintillations caused by ionospheric irregularities from multipath due to physical obstacles (buildings, trees, etc.) that may be present in the environment surrounding the receiver antenna. However, as shown by D'Angelo et al. (2015), the choice to apply a mask of 20° on the elevation angle of the satellites is not always effective in eliminating all multipath effects even if it is difficult to perform such site characterization in remote sites such as those selected for the investigation proposed in this thesis. On the other hand, the polar regions are usually characterized by very few environmental constraints making the choice of 20° elevation mask a good compromise between the loss of scintillation data and the need multipath effects filtering. Finally, to minimize possible mismeasurements of the scintillation indices following a loss-of-lock event, only data characterized by lock time greater than 240 seconds (Smith et al., 2008) were included in the analysis.

In order to derive scintillation indices using GNSS measurements, it is necessary to remove a long-term trend consisting of the Doppler shift due to satellite receiver relative motion and slowly varying background ionosphere, and some hardware effects such as clock drift. Usually, a sixth-order Butterworth filter with a 0.1 Hz cut-off frequency is used in standard processing to detrend the signal (see e.g., Prikryl et al., 2014). Such cut-off frequency was statistically obtained using wideband satellite measurements (Fremouw et al., 1978) and it is now widely used for the automated calculation of scintillation indices (Van Dierendonck et al., 1993). However, the choice of this cut-off frequency is not unique and should be done carefully. This is because amplitude and phase fluctuations in a received electromagnetic wave may be diffractive or refractive. As the diffraction is stochastic, such scintillations cannot be corrected. On the other hand, since the refraction is deterministic, such scintillations, which are typically produced by ionospheric irregularities at small wave numbers, can be corrected using multi-frequency measurements. Hence, if the choice of this cut-off frequency is not done carefully, the refractive variations are also included (Forte and Radicella, 2002; Mushini et al., 2012). As the value of the cut-off frequency does not affect the determination of the amplitude scintillation index, but it does affect the phase scintillation index very much (see e.g. Forte and Radicella, 2002; Beach, 2006; Mushini et al., 2012) this leads to case of “phase without amplitude scintillation”. This is especially true at high latitude (see e.g. Doherty et al., 2003; Mitchell et al., 2005), where a very high and variable ionospheric drift velocity (~ 100 m/s– 1500 m/s, see e.g., MacDougall and Jayachandran, 2001) exists. Such high and variable ionospheric drift velocity, indeed, directly affect the cut-off frequency as it linearly depends on the relative velocity between the receiver, the ionosphere, and the GPS satellite (e.g., Forte and Radicella, 2002). The choice of the best cut-off to be adopted is crucial for high accuracy positioning. This is beyond the scope of this thesis that is addressed to the scientific understanding of the scintillations events. In this context, the

analysis is made keeping a cut off frequency to 0.1 Hz to highlight the deterministic effects due to changes in the plasma velocity.

The data treatment described in this chapter provides information on the ionospheric irregularities from the scintillation indices. The ionospheric irregularities that cause scintillation can thus be identified and, through the integration of the analysis of ROT, the dynamics of the irregularities can be investigated. As has been mentioned in the section 2.2.2, the choice to adopt ROT is driven by its property to provide information on large-scale irregularities (Zou and Wang, 2009). This parameter is used for the identification of the electron density gradients leading to the observed ionospheric scintillations (Alfonsi et al., 2011). Furthermore, as the ROT definition is formally similar to the TEC first derivative (see equation (2.9)), which provides ROT values expressed in units of total electron content unit over one minute, [TECu/min]) this parameter provides information about the TEC speed variation. For this reason, it is possible to investigate dynamic specific features of ionospheric irregularities into which the ionospheric plasma is fragmented. In this work, ROT values are calculated for each visible GNSS satellite with an elevation angle greater than 20° . In addition, to minimize mismeasurements of ROT following a loss-of-lock event only data characterized by lock time greater than 240 s were included in the analysis.

THE CHALLENGE TO TRACE BACK THE PHYSICAL MECHANISMS CAUSING THE OBSERVED SCINTILLATIONS

This work adopts a multi-observation approach with the aim to understand how different configurations of the solar wind-magnetosphere-ionosphere coupling result in GNSS scintillations at high latitudes. Such an approach, combining information derived from ground-based measurements with those derived from space-based stations, allows a broad spectrum of information in order to characterize ionospheric disturbances at different time scales (from milliseconds to days) and spatial scales (from millimetres to hundreds meters/kilometres) in accordance with the evolution of storm drivers. This allows a reconstruction of the spatial-temporal scenario in which scintillation events occur, with the aim to investigate the cause/effect relationships that regulate the formation and evolution of irregularities causing the observed scintillations. This chapter provides a critical description of the parameters selected to characterise the ionospheric behaviour under strong perturbations of the magnetosphere-ionosphere system, providing also the motivation and the critical issues related to their choice.

3.1 THE NEED TO INTEGRATE ANCILLARY DATA

The choice to adopt a multi-instrumental and multi-observation approach is suggested by the multitude of phenomena contributing in the ionosphere to the formation and evolution of irregularities causing scintillations at high latitude. In such regions the connection, through the magnetic field lines, between the ionosphere and the magnetosphere and the presence of cusps makes the behaviour of the ionospheric plasma a direct consequence of solar wind action and magnetospheric dynamics (see sections 1.3.1, 1.3.2 and 1.4.1-3). For this reason in order to trace the physical mechanisms causing the observed scintillations, it is necessary to reproduce the sequence of events that generate the ionospheric irregularities. Moreover, the adopted method overcomes some of the limitations of GNSS measurements of the ionosphere, such as the information on electron density that can be inferred only as integrated along the satellite-receiver ray path (2.2.2). Such limitations imply the impossibility of retrieving the altitude resolution on the electron content.

The study of the origin and evolution of ionospheric irregularities causing scintillation depends on evaluating the ionospheric background starting from the solar wind conditions, then studying the magnetosphere configuration during the main phases of some intense geomagnetic storms and, finally, reconstructing the ionospheric scenario resulting in the observed scintillations.

In order to achieve this, the proposed characterization of the solar contribution to the ionospheric plasma circulation examines solar wind parameters acquired by the Advanced Composition Explorer (ACE) and WIND spacecraft orbiting at the first Lagrangian point orbit (L1). Both satellites are equipped with a fluxgate magnetometer that measures the local IMF and establish structure and fluctuation characteristics of the IMF at 1 AU upstream of Earth as a function of time (Lepping et al., 1995; Smith et al., 1998). They are also equipped with particle detectors that provide the solar wind plasma electron and ion fluxes as a function of direction and energy (Ogilvie et al., 1995; McComas et al., 1998). Providing every minute detailed knowledge of the solar wind conditions and internal state, these data allow relating solar wind variation to geomagnetic field activity (see e.g. Svalgaard, 1977; Ruohoniemi and Greenwald, 2005; Liu et al., 2015). The National Aeronautics and Space

Administration (NASA) Coordinated Data Analysis Web ([CDAWeb, https://cdaweb.gsfc.nasa.gov/istp_public/](https://cdaweb.gsfc.nasa.gov/istp_public/)) provides such data.

In order to understand how the plasma emitted from the Sun interacts with the Earth space environment plasmas producing irregularities, the Rankine Hugoniot's conditions (see e.g. Tidman and Krall, 1971) are applied to the solar wind data. This led to identify the principal characteristics of an interplanetary shock such as the velocity and the trajectory followed by shock (IPs, see section 1.1). In fact, these conditions, describing the relationship between the plasma conditions on both sides of an IPs wave in a one-dimensional flow in fluids, yielding the evaluation of both the normal to IPs plane and the IPs impact point at magnetopause.

To determine and quantify the magnetosphere deformation associated with the storms drivers, the Earth's magnetic field data provided by fluxgate magnetometers on board of the Geostationary Operational Environmental Satellite system (GOES, Singer et al., 1996) are analysed and interpreted. Such satellites, orbiting about 35,800 km, provide measurements of the space environment magnetic field that controls charged particle dynamics in the outer regions of the magnetosphere allowing both information on the general level of geomagnetic activity and sudden magnetic storms. These measurements are selected to determine the magnetospheric configuration during storms occurrence (see e.g. Lui, 1993; Apatenkov et al., 2007; Villante and Piersanti, 2008). The NASA CDAWeb (https://cdaweb.gsfc.nasa.gov/istp_public/) provides such data.

Ground-based fluxgate magnetometers located both at high and low latitudes, are used in this project because these data provide continue and systematic measure of the Earth's magnetic field components in addition to *geomagnetic indices* (see 1.4.4). Such indices provide an indication of the Earth's magnetic field under quiet and perturbed conditions. In addition, data collected by fluxgate magnetometers co-located with GNSS receivers are used to support the description of the ionospheric area in the field of view of such receivers. The International Real-time Magnetic Observatory Network (INTERMAGNET, <http://www.intermagnet.org/>) provides such data.

The Earth's magnetic field data acquired by the Iridium constellation are analysed and interpreted. The Iridium satellite constellation provides voice and data coverage to satellite phones, pagers and integrated transceivers over the Earth's entire surface (Pizzicaroli, 1998). Magnetometers data from this constellation (of 66 active satellites in low Earth's orbit [~ 780 km] that ensure a global coverage of the Earth) provide measurements of the inner magnetospheric field. Specifically, the magnetometer data are sent from the Iridium Satellite Network Operations Center to the Active Magnetosphere and Planetary Electrodynamics Response Experiment (AMPERE) Science Data Center. Here they are processed to extract the magnetic perturbation signatures associated with the FAC system (see 1.2.1) connecting the ionosphere to the magnetosphere (Anderson et al., 2000). Therefore, AMPERE data are taken into account in this project to investigate the role of FAC in determining ionospheric conditions causing scintillations. The AMPERE Science Data Center (<http://ampere.jhuapl.edu/>) provides such data.

In order to understand the role played by precipitating particles in scintillation production, this study includes the analysis and interpretation of data acquired by National Oceanic and Atmospheric Administration (NOAA) Defence Meteorological Satellite Program (DMSP), Polar-orbiting Operational Environmental Satellites (POES) and by Meteorological Operational (MetOp) satellites. These are all low, polar, earth-orbiting satellites at about 850 km from the Earth's surface. Specifically, DMSP satellites are equipped with the Special Sensor Ultraviolet Spectrographic Imager (SSUSI, Paxton et al., 1992) consisting of sensors intended to provide a quantitative description of the state of the upper atmosphere and the aurora on a global basis. In this work, the data from SSUSI

are used to monitor the evolution of auroral radiance during a geomagnetic storm, with the aim to investigate the link between particle precipitation in the auroral oval and high latitude ionospheric irregularities formation. SSUSI data can be obtained from <https://ssusi.jhuapl.edu/>. The POES and MetOp satellites are equipped with the Total Energy Detector (TED, Evans and Greer, 2004) which acquired the data analysed in this work. In particular, the TED consists of two detectors capable of monitoring the influx of energetic ions and electrons into the atmosphere and the particle radiation environment at the altitude of the satellite. The electron and proton total atmospheric integral energy fluxes are used in this work to verify how the observed scintillation is related to particle precipitation. The NASA CDAWeb (https://cdaweb.gsfc.nasa.gov/istp_public/) provides such data.

In-situ measurements of plasma density in the topside ionosphere provided by Langmuir probes on board the Swarm constellation (Friis-Christensen et al. 2006) are analysed and interpreted to provide a local and global characterization of the ionospheric electron density distribution during geomagnetic storms. This constellation consists of three satellites able to provide high-precision and high-resolution measurements of the strength, direction and variations of the magnetic field and plasma data such as temperature and electron density of the ionosphere. The choice to analyse Swarm data is linked to the geometry of the constellation. The Swarm satellites are located at two different polar orbits, two flying side by side at an altitude of 460 km (Swarm A and C) and a third at an altitude of 530 km (Swarm B). This allows an investigation of ionospheric plasma density distribution at different altitudes and in different geomagnetic sectors, providing a characterization of ionospheric conditions before, during and after solar perturbations. Swarm data are available from the European Space Agency (ESA) Earth Online service (<https://earth.esa.int/web/guest/swarm/data-access>).

Ionospheric irregularities are first identified from TEC and scintillation parameters (see sections 2.2.1 and 2.2.2), then the ionospheric information from GNSS measurements is integrated with observations provided by ionosondes and backscatter radars. In particular, the study includes vertical radio-sounding data products (known as *ionograms*) provided by the Vertical Incidence Pulsed Ionospheric Radar (VIPIR, Bullett et al., 2016), co-located with the Mario Zucchelli (Terra Nova Bay) GNSS station. The ionosonde transmits vertically upward frequencies typically from 0.5 to 30 MHz and measures the time delay of the reflected ionospheric echoes. This yields vertical reflection frequencies of the different ionospheric layers (see section 1.3) and the virtual altitudes of such layers. The information from these parameters are used to understand the local ionospheric vertical structure induced by storm drivers, also inferring the ionospheric plasma perturbation state and the possible presence of irregularities. Through a scientific collaboration with the INGV, the Korean Polar Research Institute provided VIPIR *ionograms* used in the present investigation.

Furthermore, in order to characterise the high latitude ionosphere dynamics in which irregularities causing scintillations form and drift, including its spatial evolution, in connection with the conditions both of the Earth's magnetosphere and the interplanetary medium, measurements of horizontal plasma velocities supplied by the Super Dual Auroral Radar Network (SuperDARN,) are also examined. SuperDARN is an international scientific consortium that operates and maintains high frequency (HF), over-the-horizon radars for conducting research in ionosphere and space physics (Greenwald et al., 1995). SuperDARN is designed to map ionospheric plasma convection over the auroral and polar cap regions according to observational fields of view shown in Figure 16. To achieve plasma convection, 2-D Doppler velocity vectors are estimated from pairs of radars with overlapping fields of view. In normal mode, each beam is formed under computer control by a phasing matrix, to scan over 16 sequential beam directions. This provides an overall azimuth coverage of $\sim 50^\circ$. A multi-pulse transmit sequence enables SuperDARN radars to measure Doppler velocities up to 2 km/s over distances of ≤ 3500 km. The resulting autocorrelation function for every range gate is

used to estimate 2-D Doppler velocity, the scattered signal power and the width of the Doppler power spectrum for each range where there are significant returns (spectral width). The cause of various magnitudes of spectral width can be attributed to diffusion and dynamics of ionospheric plasma irregularities (Ponomarenko and Waters 2006); on the other hand, at high latitude, the ionospheric scintillations recorded on the phase can appear when the GNSS signals pass through regions in which plasma dynamics is more complex (see e.g. Mitchell et al., 2005). Therefore, spectral width measurements are taken into account and analysed in order to support the identification of regions most likely to give rise scintillations. Moreover, measurements of Doppler velocities are considered in order to link the local and global evolution of the auroral and polar cap dynamics during storms. The British Antarctic Survey provides SuperDARN data via ftp, upon registration (<https://www.bas.ac.uk/project/superdarn/#data>).

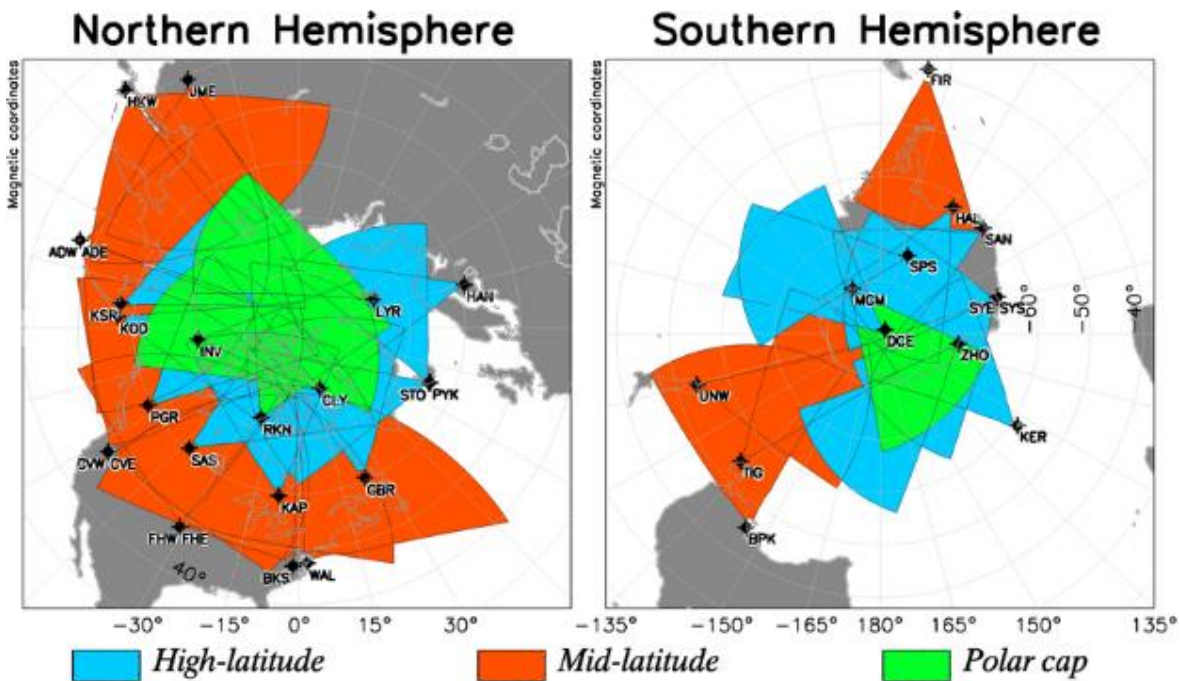


Figure 16: Fields of view geometry of the SuperDARN network radars. On the left, the observational geometry of radars located in the northern hemisphere. On the right, the observational geometry of radars located in the southern hemisphere. The colour code refers to the position in magnetic latitude of each radar.

3.2 DATA INGESTION CHALLENGE

As mentioned in section 3.1 the multi-observation approach is useful for providing a detailed description of the ionospheric scenario in which irregularities causing scintillation are formed and move. Furthermore, combining a broad spectrum of information, such approach provides for the measurements' lack compensation due to both instrumental limits and the physical nature of the investigated phenomenon (such as, for example, the absence of reflected echoes during strong ionospheric absorption events or the poor coverage ensured by fields of view of considered instruments). On the other hand, the integration of different data, that differentiate for sampling frequency and/or because acquired at different heights from the Earth's surface, constitutes a great challenge. The challenge lies in the appropriate choice of a priori assumptions both on the measures to be compared and on the time intervals covered by these measures. Although these assumptions are necessary to investigate the cause/effect relationships regulating the formation and evolution of irregularities at high latitude, they do not prove to be always sufficient to describe the ionosphere's evolution in space and time. On the other hand, description point by point of the ionospheric evolution

under conditions of strong helio-geophysical disturbance is bound by limitations of the instruments currently in use for the investigation of circumterrestrial plasmas. In such a frame, the assumptions adopted in this work aims at providing the best possible ionospheric characterization within instrumental limitations, the physical nature of the investigated phenomenology and the constraints imposed by the integration of multi-observational data.

Therefore, the analysis of case studies selected for this work is carried out through a capillary survey that can be summarized in the following fundamental steps:

1. Characterization of the interplanetary perturbations and assessment of the geomagnetic response at high and low latitudes.
2. Evaluation of the normal to IPs plane and estimation of the IPs impact point at the magnetopause.
3. Reconstruction of the magnetospheric field line geometry reconfiguration following the interplanetary perturbation arrival.
4. Evaluation and quantification of the FACs system evolution during disturbed periods.
5. Investigation of the scintillation parameters (σ_ϕ , S_4 and ROT) variations.
6. Reconstruction of the ionospheric scenario in which irregularities causing the observed scintillations form and evolve in space and time, through the integration of observations from satellites, radars and ground-based magnetometers.

For the characterization in point 1, the UT time series of the IMF amplitude ($|B|_{\text{IMF}}$), and its components ($B_{x,\text{IMF}}$, $B_{y,\text{IMF}}$, $B_{z,\text{IMF}}$), the solar wind density (ρ_{SW}), proton temperature (T), velocity (V_{SW}) and dynamic pressure (P) are analysed for each case study. These series, acquired by ACE and WIND spacecraft, are then compared with the SYM-H index, the auroral oval (AU and AL) indices and the polar cap (PCN and PCS) indices calculated from the Earth's magnetic field measurements recorded by ground-based magnetometers. For all the described quantities, a sampling time of one minute is used both to identify their variations and to provide a comparison with the variations in point 5 above. This characterization aimed both at identifying the disturbance level of the environment in which irregularities occur, and is searching for a cause-effect relationship between the interplanetary disturbance type and the ionospheric irregularity associated with the observed scintillations. The evaluation of the normal to IPs plane is accomplished by applying the Rankine Hugoniot conditions to solar wind data. Since this investigation involves a comparative evaluation of the high latitude ionospheric response in both hemispheres, the evaluation of the normal to IPs plane and the consequent estimation of the IPs impact point at the magnetopause allows a determination of which hemisphere is most exposed to the perturbation coming from the Sun.

The characterization for point 3 is pursued to investigate the magnetospheric field lines geometry reconfiguration following the interplanetary perturbation impact geometry. It is derived from the analysis and interpretation of the UT variations of Earth's magnetic field components acquired by fluxgate magnetometers on board the GOES satellites. This investigation allows a quantification of the magnetosphere's erosion and/or compression in the dayside and its elongation in the nightside at the arrival of the interplanetary perturbation, allowing a determination of the Earth's field reconfiguration due to the interplanetary perturbation. It also permits an estimation of the possible asymmetry level between the two magnetospheric tail lobes following the interplanetary perturbation impact at a point far from the geomagnetic equator.

The fourth step of the analysis consists of the characterization of the FACs system. In the FAC maps, the Altitude Adjusted Corrected GeoMagnetic (AACGM; Baker and Wing, 1989) coordinates (MLat, MLon) and Magnetic Local Time (MLT) are used as the reference frame. They cover the ranges 00–

24 Magnetic Local Time (MLT) and 50°–90° Magnetic Latitudes (MLat) for both hemispheres allowing the FACs system dynamics to be related to magnetospheric dynamics and with the storm driver variations. Moreover, the graphical representation of the FACs system helps estimate the IPs impact point at the magnetopause. In fact, the comparative investigation of the variation (in time and space) of the FACs in both hemispheres allows an understanding of if and which of the two hemispheres is firstly exposed to the perturbation. It is important to emphasise that, since the time sampling with which the AMPERE Science Data Center supplies the FACs current density data is 10 minutes, the maps examined in this work summarize the variation of the current density in the same time interval.

The investigation of the scintillation parameters at step 5 of the analysis is performed for each GNSS station (Table 1), by studying the UT variations of the scintillation indices (σ_ϕ and S_4) and the ROT (sections 2.2.1 and 2.2.2). In particular, the UT variations recorded by the northern GNSS receivers are compared with those recorded by the southern GNSS receivers that, in quiet geomagnetic conditions, look approximately at the same ionospheric regions. The station pairs considered are: EURC-DMC0 and RESC-BTN0 that, under quiet geomagnetic conditions, map for most of the day at the polar caps, and NYA0-ZSGN, which under the same quiet conditions map to polar cusps/auroral regions. The SNA0 receiver, maps to sub-auroral regions under quiet geomagnetic conditions. The choice to sort the stations according to ionospheric region allows an interhemispheric comparison of the ionospheric response in terms of scintillation occurrence. By comparing the variations recorded by the receivers located in the same hemisphere, it is possible to investigate the ionospheric response in different geomagnetic sectors. To obtain the UT variations of the scintillation parameters, the data acquired from each GNSS station are processed according to the method described in the previous chapter (section 2.3). The study considers a sampling per minute to compare the UT variations of the scintillation parameters with the UT variations of the parameters selected according to step 1 of the analysis. This comparison allows describing the observed scintillations in relation with the variations of both the interplanetary medium and the Earth's magnetic field. The additional information derived from the analysis of the UT variation of ROT is used according to the empirical method introduced by Alfonsi et al. (2011) to deduce the scale size of the irregularities triggering scintillation. This is what was hypothesised by Alfonsi et al. (2011): since the scintillation on the phase of the signal can be produced by a wide range of spatial scales of ionospheric irregularities, an ionospheric region, characterised by strong heterogeneity of scales or that presents a strong homogeneity around more active scales, identifies a sector in which the scintillation occurrence probability is high.

In order to support the reconstruction of ionospheric features detected by ROT and scintillation parameters, information from GNSS measurements with concurrent supporting information provided by ground-based and space-borne observations are combined (step 5 of the analysis). Namely:

- To provide an overall representation of high-latitude ionospheric irregularities causing observed scintillations, polar-view maps displaying simultaneously: SuperDARN observations, Swarm electron density measurements and the projection of the GNSS tracks experiencing scintillation are generated for each hemisphere. Such maps, covering the ranges 00–24 MLT and 50°–90° MLat of both hemispheres, allow the observed scintillations, the electron density variation recorded by Swarm satellites and the local variations of the ionospheric plasma dynamics (inferred by the SuperDARN spectral width measurements) to be compared with magnetospheric dynamics. Spectral width measurements are considered because they support the identification of ionospheric regions characterized by different plasma regimes (see e.g. Woodfield et al. 2002, Chisham and Freeman, 2004, Ponomarenko

and Water 2006, Ponomarenko et al., 2007). As such regions are most likely to give rise ionospheric scintillations on GNSS phase signals (see e.g. Doherty et al., 2003; Mitchell et al., 2005), the comparison between spectral with measurements and phase scintillations allows investigating physical mechanisms causing corruption on GNSS signals. The integration of different data into the polar-view maps implies the choice of appropriate a priori assumptions linked both to the sampling frequencies of these measures and to their acquisition height. The first assumption taken into account is to consider the ionospheric vertical variation as constant between the average height at which SuperDARN measurements are taken, and the Swarm satellite heights. Since the investigation in this work covers periods in which the magnetosphere-ionosphere system experiences large disturbances, this assumption is not so forced. In fact, at the arrival of a large interplanetary perturbation, a considerable increase in the current density of the FACs system occurs (which can be confirmed by the maps at step 4 of the analysis). Hence, it is reasonable to consider a slight variation of the ionosphere between the heights covered by the measurements under examination. This assumption is also in agreement with the choice to fix the H_{IPP} at 350 km in equation (2.12), describing the obliquity factor ($F(\alpha_{elev})$) in the scintillation indices projection to the vertical. The second assumption assumed in the construction of the maps concerns the temporal resolution of the measurements. The temporal choice takes into account the scintillation recorded by the GNSS receivers of the selected network (in Table 1) during the passage of the Swarm satellites over an area covering 50° to 90° of magnetic latitude in both hemispheres. Even if such assumption does not allow correlating, in a univocal way from a temporal point of view, the observed scintillation with the electron density variations recorded by the Swarm satellites, it permits obtaining a local characterization of the ionospheric plasma conditions likely triggering the scintillation events. In addition, since the SuperDARN measurements are provided with a 2-minute time resolution, only measurements acquired in the 2 minutes coinciding with the Swarm satellite transit time over the magnetic pole are shown on the maps. In this case, the ionospheric dynamics depicted by the SuperDARN measurements is considered as representative of the entire period covered by the traces of the Swarm satellites. Although this is a quite forced assumption, especially during strong helio-geophysical disturbance periods, thanks to the comparative investigation of maps describing ionospheric conditions in different time intervals, it is possible to provide an overall representation of the high-latitude ionospheric scenario in which scintillations occur. Furthermore, since the fields of view of the selected GNSS receivers cover, in both hemispheres, an ionospheric portion within about 70° MLat, the multi-observational integration enclosed in the polar-view maps ensures that the electron density variations recorded by the Swarm satellites in such area are simultaneous with the ionospheric scenario provided by SuperDARN measurements. In this way, the multi-observational integration ensures that the observed scintillations are the result of such scenario.

- To monitor the evolution of the auroral radiance during a geomagnetic storm and to investigate the link between precipitating particles in the auroral oval and high latitude ionospheric irregularities formation, the data are shown as polar-view maps in AACGM reference system, covering the ranges 00–24 MLT and 50° – 90° MLat of both hemisphere. These maps compare the auroral radiance measurements provided by DMSP constellation satellites and the scintillations recorded by the receivers of the selected GNSS network (Table 1). In particular, such maps show for each hemisphere the scintillations recorded in the time taken by the DMSP satellites to cover the selected MLat range. As mentioned previously, the assumption is to consider the ionospheric vertical variation as constant between 350 km and

the height to which the observations of the DMSP constellation's satellites are acquired. This assumption is realistic under the same hypothesis discussed in the previous point.

- To provide an estimation of the average variability of the electron density measured through the polar caps by the Swarm satellites at different times of day, the electron density root mean square (*rms*), calculated for each time series related to a polar crossing of each Swarm satellite (above $|50^\circ|$ magnetic latitude) is analysed. The *rms*, being an indicator of the electron density variability, could give a measure of the ionospheric plasma variability induced by storm drivers. In particular, this information is obtained by comparing the *rms* variations with variations in IMF at step 1 of the analysis. Given the Swarm constellation's geometry, it is also possible to investigate the role played by storm drivers in triggering electron density variations at different heights. The interhemispheric comparison of *rms* variations allows quantifying the symmetry/asymmetry of both the ionospheric electron density and variability before and after the arrival of an interplanetary perturbation. Furthermore, the comparison between the *rms* variations and the variations of the scintillation parameters (at point 5) allows deducing the role of the electron density variations in scintillation production.
- To support the description of interhemispheric symmetries/asymmetries caused by the impact geometry of an IPs, the total atmospheric integral energy flux of particles precipitating in the ionosphere is investigated as a function of magnetic latitude. In particular, such flux is obtained by adding the total electron and proton atmospheric integral energy fluxes. These fluxes, measured approximately at about 850 km by POES and MetOp constellation satellites, are provided by the NASA CDAWeb integrated at 120 km from the Earth's surface. In such a way, they provide information about the effect of particles precipitation on changes in the ionospheric plasma dynamics in the E-layer.
- To provide a local characterization of the ionospheric irregularities causing scintillation, ionograms acquired by the VIPIR ionosonde are analysed. From the analysis of an ionogram it is possible to obtain numerous parameters that have a significant role in the study of ionospheric physics. The most important are the critical frequencies (see section 1.3) of ionospheric layers (which are frequencies, directly proportional to the electron density of ionospheric layers, for which the reflection of the incident electromagnetic wave is maximum) and the virtual heights of the same layers. By comparing the information derived from these parameters with those obtained from the multi-parameter survey and from variations of the scintillation parameters detected by the GNSS receivers co-located with the selected ionosondes, it is possible to understand the local ionospheric vertical structure induced by storms. From such comparisons, it is possible to infer the ionospheric plasma perturbation state and the presence of irregularities.
- To support the description of the response of the ionospheric area within the field of view of the GNSS receivers, the UT variations of Earth's magnetic field components recorded by ground-based fluxgate magnetometers, co-located with GNSS receivers, are analysed and interpreted. In particular, being such magnetometers data provided at 1-minute sampling time, it is possible to compare their variations with those of IMF and solar wind parameters.

The multi-parametric investigation is used to reconstruct the magnetosphere-ionosphere coupling before and after solar perturbations arrivals. This provides the local and global reconstruction of the spatial-temporal context in which the observed scintillation events occur, allowing an investigation of the cause/effect relationships that regulate the formation and evolution of irregularities at high latitude.

3.3 POSSIBILITY OF USING MODELS

To support the global characterization of the ionosphere-magnetosphere dynamics under conditions of strong helio-geophysical disturbance, this work makes use of models. Model data, under appropriate hypotheses, compensate for the lack of information due to instrumental limits and physical nature of the investigated phenomenon. This work leverages predictions from two models: the Tsyganenko and Sitnov (2005) magnetospheric field model (TS04) and the ionospheric electrostatic potential model, as provided by SuperDARN (Cousins and Shepherd, 2010). Namely:

- TS04 is a semiempirical-dynamical data based model of the inner magnetospheric field under various conditions. It approximates the magnetospheric field as a sum of contributions from all major external current systems, each of which evolves in time according to its own mode of response to solar wind driving, saturation threshold, and relaxation timescale (Tsyganenko and Sitnov 2005). The current systems involved in the TS04 model are the Chapman-Ferraro current, the tail current, the symmetrical ring current, the partial ring current, the field-aligned currents, and the interconnection current (i.e., the current due to a partial penetration of the IMF inside the model magnetosphere). By comparing magnetospheric field observations, provided by satellites, with the prediction of this model, it is possible to obtain a reasonable picture of the magnetosphere shape (in terms of individual currents and global geometry) at the arrival of perturbations coming from the Sun. This model supports the description of magnetospheric dynamics in terms of interhemispheric symmetries/asymmetries.
- The ionospheric electrostatic potential model reconstructs the isocontours of the ionospheric potential by means of a statistical model of average convection as a function of external driver conditions (above all, the interplanetary magnetic field and the solar wind speed), constrained on the actual data where they are available (e.g. Cousins and Shepherd, 2010). These are provided by SuperDARN in the form of convection maps. Although they only provide an average picture of the high latitude ionosphere dynamics, they can be useful to link the local and global evolution of polar caps dynamics especially in those regions in which the number of the observed echoes is not null. This is the reason why spectral width measurements are plotted on convection maps. Such maps are also compared with the observed scintillation and the electron density variation recorded by Swarm satellites in order to retrieve the ionospheric scenario in which irregularities causing scintillation appear and evolve.
- The ionospheric electrostatic potential model reconstructs the isocontours of the ionospheric potential by means of a statistical model of average convection as a function of external driver conditions (above all, the interplanetary magnetic field and the solar wind speed), constrained on the actual data where they are available (e.g. Cousins and Shepherd, 2010). These are provided by SuperDARN in the form of convection maps. Although they only provide an average picture of the high latitude ionosphere dynamics, they can be useful to link the local and global evolution of polar caps dynamics especially in those regions in which the number of the observed echoes is not negligible. Therefore, the spectral width associated with each velocity measurement has been displayed in the maps with a twofold purpose. On one hand, to point out the presence of echoes from SuperDARN in the scintillation regions. This can reasonably argue that the potential contours reconstructed there are not artefacts of the model. On the other hand, the magnitude of the spectral width, supporting the identification of ionospheric regions characterized by different plasma regimes, can give hints on the nature of the irregularities. Such maps are also compared with the observed scintillation and the electron density variation recorded by Swarm satellites in order to retrieve the ionospheric scenario in which irregularities causing scintillation appear and evolve.

SCINTILLATION EVENTS DURING THREE STRONG GEOMAGNETIC STORMS OF THE SOLAR CYCLE-24

This chapter discusses the results obtained by applying the multi-observational method (sections 3.2 and 3.3) to the main phases of three intense geomagnetic storms, which occurred during solar cycle 24. The selected case studies occurred on: March 2015, June 2015 and September 2017. In particular, the investigation described in this chapter focuses on the interplanetary medium conditions that occurred on 2015 March 17, on 2015 June 22 and on 2017 September 8.

Beside their intensity, the peculiarity of such storms lies in their occurrence during the spring and fall equinoxes, and during the summer (winter, for the southern hemisphere) solstice. These storms were triggered by the superposition of many solar events. The analysis investigates the induced interhemispheric symmetries/asymmetries of the magnetosphere-ionosphere system in terms of its pre-existing symmetries/asymmetries and the role played by different solar events in the formation of ionospheric irregularities causing scintillations.

4.1 THE 2015 MARCH STORM

The main phase of the St. Patrick's geomagnetic storm occurred on 2015 March 17. The storm, studied by several authors (see e.g. Cherniak et al. 2015; Kamide and Kusano 2015; Liu et al. 2016 and references therein), was caused by two interacting ICMEs (Liu et al. 2015) preceded by an IP and characterised by a long period with negative values of the IMF B_z component. This produced a strong disturbance of the Earth's magnetic field causing intense particle precipitation and enhancement in substorm activity with a subsequent and conspicuous development of plasma density irregularities (Wu et al. 2016, Cherniak et al. 2015, Cherniak and Zakharenkova 2015). This storm constituted a powerful test bench for probing the physical conditions in which irregularities appear and evolve.

4.1.1 RESULTS

Figure 17 shows, from top to bottom, the UT variations of the IMF amplitude ($|B|_{\text{IMF}}$), IMF B_x component ($B_{x,\text{IMF}}$), IMF B_y component ($B_{y,\text{IMF}}$), IMF B_z component ($B_{z,\text{IMF}}$), solar wind density (ρ_{SW}), proton temperature (T), velocity (V_{SW}) and dynamic pressure (P), acquired by WIND on 2015 March 17. It also shows the UT variations of the SYM-H index, auroral oval (AU and AL) and polar cap (PCN and PCS) indices. The shaded regions indicate the two ICME intervals and the black dashed vertical line marks the corresponding shock arrival at WIND. At ~04:00 UT WIND detected an IP, as visible from the sharp change in solar wind density (ρ_{SW} , from $\sim 17 \text{ cm}^{-3}$ to $\sim 78 \text{ cm}^{-3}$, panel e), speed (V_{SW} , from 400 km/s to $\sim 520 \text{ km/s}$, panel g), temperature (T , from $\sim 10^4 \text{ °K}$ to $\sim 10^5 \text{ °K}$, panel f), dynamic pressure (P , from $\sim 5 \text{ nPa}$ to $\sim 28 \text{ nPa}$, panel h) and IMF amplitude ($|B|_{\text{IMF}}$, from $\sim 9 \text{ nT}$ to $\sim 26 \text{ nT}$, panel a).

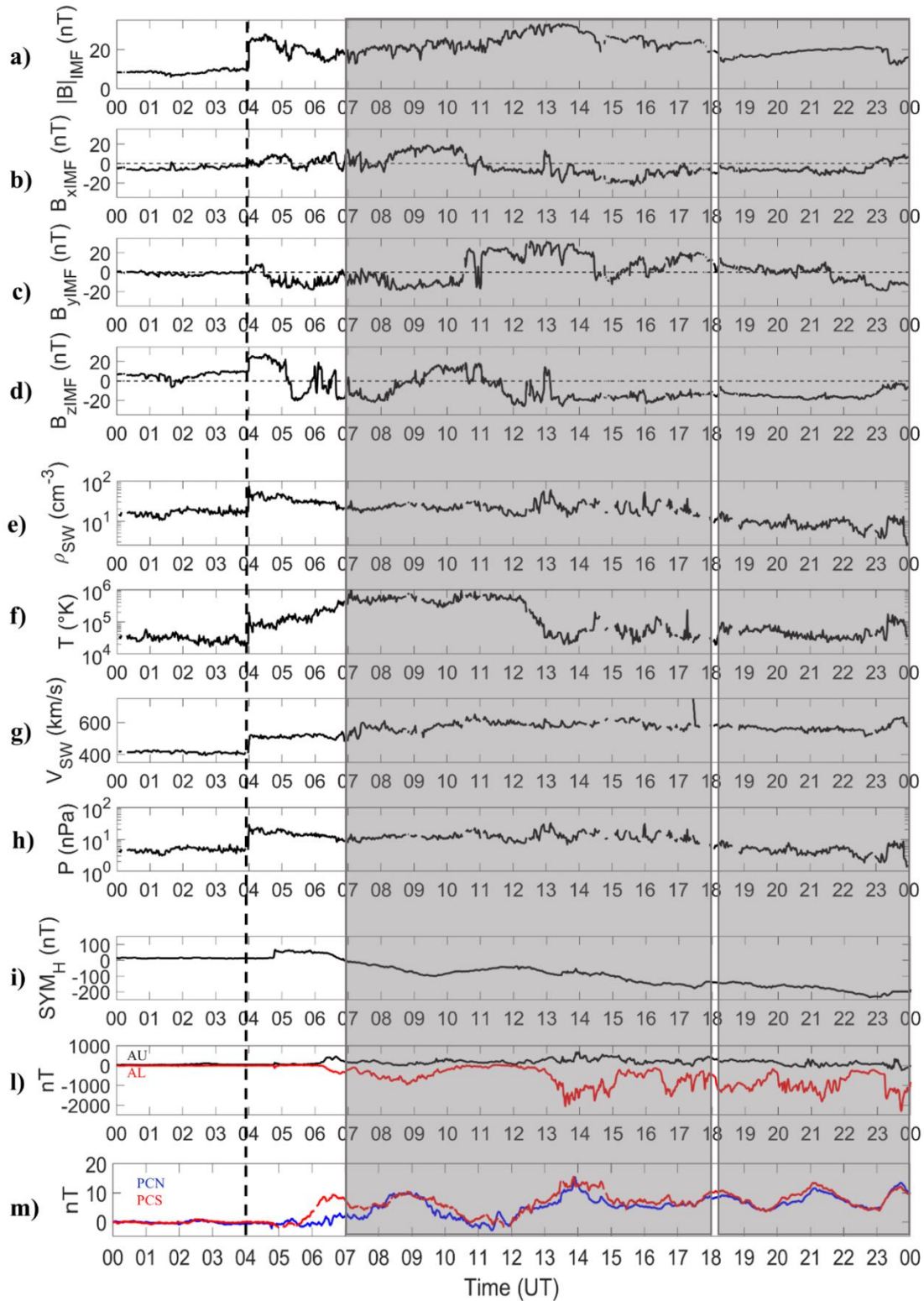


FIGURE 17: The solar wind (SW) observations (WIND spacecraft) and the geomagnetic response at low and high latitudes on 2015 March 17. From top to bottom: (a) the IMF amplitude $|B|_{\text{IMF}}$; (b) IMF $B_{x,\text{IMF}}$ component; (c) IMF $B_{y,\text{IMF}}$ component; (d) IMF $B_{z,\text{IMF}}$ component; (e) SW density ρ_{SW} ; (f) SW proton temperature T_{SW} ; (g) SW velocity V_{SW} ; (h) SW dynamic pressure P ; (i) SYM-H index; (l) AU (black line) and AL (red line) indices; (m) Polar Cap North (PCN, blue) and Polar Cap South (PCS, red). The shaded regions indicate the two ICME intervals and the black dashed vertical line marks the corresponding shock arrival at WIND.

As can be seen in panel d, during the ICMEs intervals the North-South component of the IMF ($B_{z,\text{IMF}}$) was consistently southward (at about -20 nT), except for a brief period between 09:00 and 11:00 UT.

This resulted in intense particle precipitation and enhancement in substorm activity producing a severe geomagnetic storm lasting for most of the second half of the day. In fact, the SYM-H index (panel i) shows a short drop to a minimum of ~ -245 nT observed at $\sim 23:00$ UT. The upper and lower auroral electrojet current indices (AU and AL: black and red line in panel l) also show, from $\sim 06:00$ UT until the end of the day, a strong level of current intensity of the eastward and westward northern auroral electrojets, respectively. At the same time, the Polar Cap indices show a significant increase in magnetic activity of the two polar caps (panel m), showing also a greater intensification of magnetic activity in the southern hemisphere following the IPs arrival.

In order to evaluate how the first ICME impacts the Earth's magnetosphere, an estimation of the direction of the IPs normal is obtained by applying the Rankine Hugoniot's conditions to WIND data. The resulting IPs parameters are $\theta=68.4^\circ$, $\phi=169.5^\circ$ and $V_{IPs}=560$ km/s, where θ and ϕ are the shock normal latitude and longitude in the Geocentric Solar Ecliptic (GSE) plane respectively, and V_{IPs} is the estimated IPs speed. The coordinates of the shock impact at the magnetopause were estimated to be $X_{impGSE} = 14.2R_E$, $Y_{impGSE} = 3.9R_E$. The shock, therefore, impacts the magnetopause at 13:01 LT, mainly in the southern hemisphere. These results are in accordance with the IPs parameters provided by the *Database of interplanetary shocks* of the University of Helsinki (<http://ipshocks.fi/>) and with the results of Wu et al. (2016).

The reconstruction of the shape of the Earth's magnetosphere at the arrival of the first ICME is achieved by analysing the magnetospheric field observations, provided by the GOES 15 satellite.

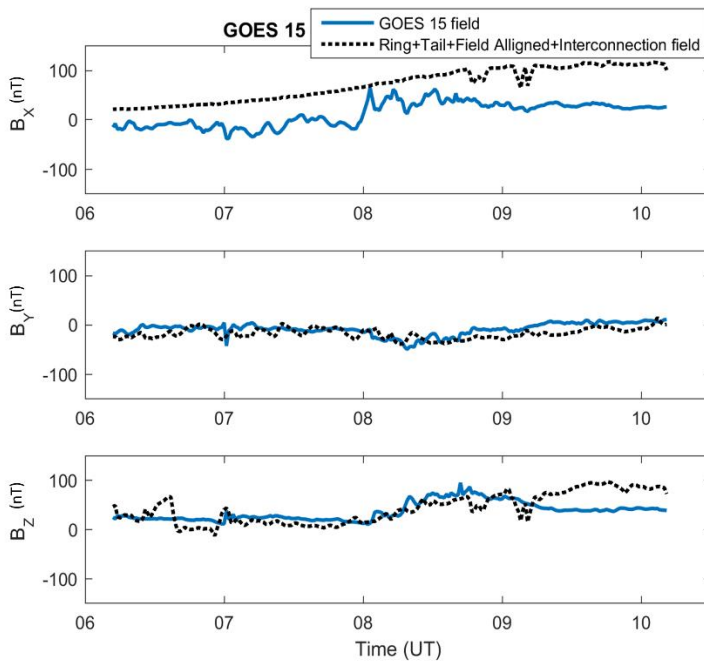


FIGURE 18: The comparison between magnetospheric observations, provided by GOES 15 geosynchronous spacecraft (blue solid lines), and a modified Tsyanenko and Sitnov, (2005) model (dashed lines). The black dashed lines represent the modelled field composed of the contributions due to the tail current, the interconnection field current, the field aligned currents and the ring current. From top to bottom: the x component of magnetospheric field (B_x); the y component of the magnetospheric field (B_y); the z component of the magnetospheric field (B_z).

Figure 18 shows GOES 15 observations (blue solid line) and the prevision of a modified TS04 model (black dashed line) between 06:00 UT and 10:30 UT of the 2015 March 17. The time range is chosen

because it coincides with the first recorded intensification of the Earth magnetic field activity following the shock impact (see panels i, l, m of the Figure 17). This range also covers the arrival of the first ICME (Figure 17). In particular, the magnetospheric observations at the ICME arrival ($\sim 08:00$ UT) show a simultaneous enhancement of both the X and the Z (~ 55 nT) components of the field, although the increase of the Z component is less abrupt and broader than the increase of the X component. This is in accordance with a tail loading during the positive switch of $B_{z,IMF}$ (Figure 17d) (Rostoker and Eastman 1987; Feldstein et al. 1996; Doxas et al. 2004; Ohtani and Uozumi 2014). Keeping in mind that the GOES satellite was around local midnight, such enhancements suggest an anti-dipolarization of the magnetotail field (Apatenkov et al. 2007; Li et al. 2014; Schmid et al. 2011; Villante and Piersanti 2008, 2009), that stretches the night side magnetospheric field lines (Lui et al. 2001; Villante et al. 2005; Piersanti et al. 2012, Piersanti and Villante, 2016). In order to confirm the anti-dipolarization, the magnetospheric observations were compared with the prediction of a modified TS04 model (hereafter TS04*; black dashed line in Figure 2). The TS04* considers the shift of the magnetotail hinging point (HT) from $7 R_E$ to $6 R_E$ and a current sheet's thickness (dT) of about 20%. In addition, as GOES 15 is located at around local midnight, TS04* approximates the magnetospheric field as a sum of contributions from only the ring currents, the field-aligned currents, the interconnection currents and the tail current. The good agreement between the magnetospheric field observations and the TS04* previsions confirms that the configuration of the magnetotail after the passage of the first ICME was characterized by strong anti-dipolarized field lines.

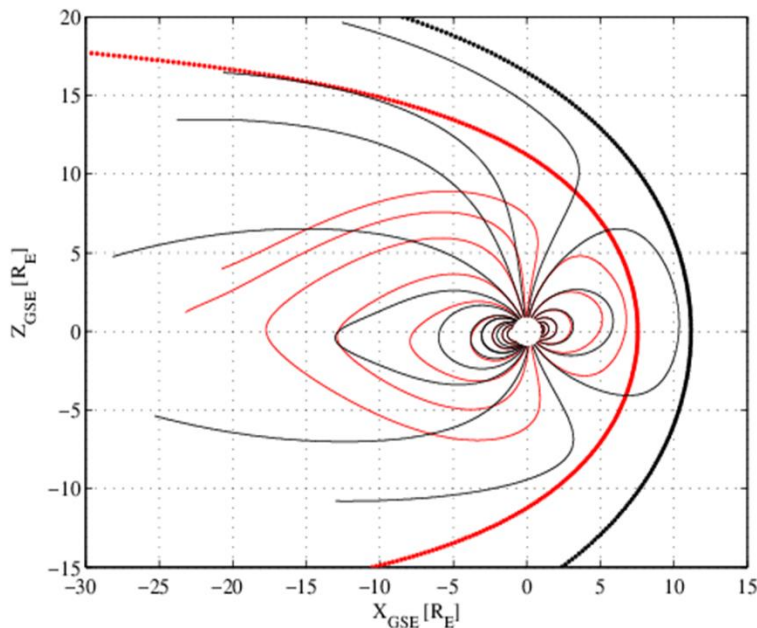


FIGURE 19: Magnetospheric field lines configuration before (black) and after (red) the IPs arrival. Black and red thick lines identify, respectively, the magnetopause before and after the IPs arrival.

Figure 19 shows the global magnetospheric field line configuration before (black lines) and after (red lines) the IP shock arrival, evaluated by TS04* model. The black and red thick lines identify, respectively, the magnetopause before and after the IP shock arrival. The IPs arrival caused a strong compression of the field lines in the dayside and stretching in the nightside, with a lowering of both lobes of the tail. Such IPs geometry, coupled with the particular configuration assumed by the night-side magnetosphere at ICME arrival and the negative value of the dipole tilt angle ($\sim -6.19^\circ$), caused

the southern hemisphere to be more exposed to the impact of the solar perturbations with respect to the northern hemisphere (Villante et. al, 2008; Alberti et al. 2016; Piersanti et al. 2012).

Figure 20 shows the polar-view maps of the FACs density in the northern (top maps) and the southern (bottom maps) hemisphere derived from IRIDIUM satellite observations between 04:40 UT and 05:00 UT on 2015 March 17. Such time range encloses ten minutes before and after the time of the IPs impact on the magnetopause. These maps show that before the IPs arrival (04:40 UT), the current density is roughly the same in the two hemispheres (top and bottom maps on the left). While, starting from 04:50 UT (IPs impact time), an intensification of the cusp currents (between 70° and 80° MLat) is observed in both hemisphere, with higher values in the southern hemisphere (see bottom maps at 04:50 UT and 05:00 UT). In addition, after the IPs arrival, currents flowing out of the ionosphere (red currents) appear more intense than the currents flowing toward the ionosphere. This is in agreement with the positive values of $B_{z,IMF}$ observed at the IPs arrival (see panel d in Figure 17). The positive $B_{z,IMF}$ condition at the IPS arrival causing a strong compression of the magnetosphere, led the plasma to escape from the ionosphere.

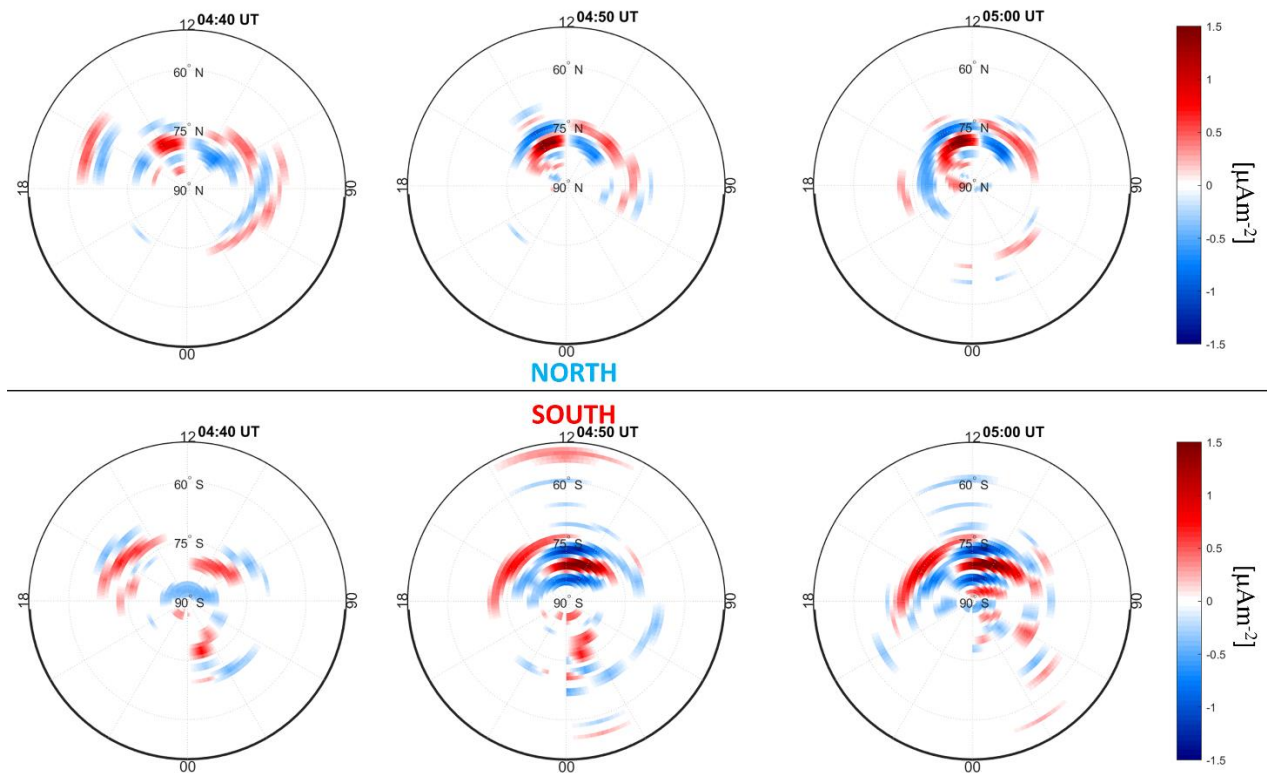


FIGURE 20: Polar-view maps displaying the current density of the FACs system in northern (top maps) and southern (bottom maps) hemisphere measured between 04:40 UT and 05:00 UT on 2015 March 17.

Figure 21 shows the time profile of σ_ϕ recorded at EURC and DMC0 (panel a), RESC and BTN0 (panel b), NYA0 and ZSGN (panel c) on 2015 March 17. The black horizontal lines indicate the 0.25 radians σ_ϕ threshold, chosen to identify moderate to strong levels of phase scintillations (see e.g., Spogli et al. 2009). Different colours refer to different satellites in view. The black dashed vertical line identifies the IPs impact time at the magnetopause, while the shaded regions indicate the intervals of the two ICMEs and highlight the scintillation events.

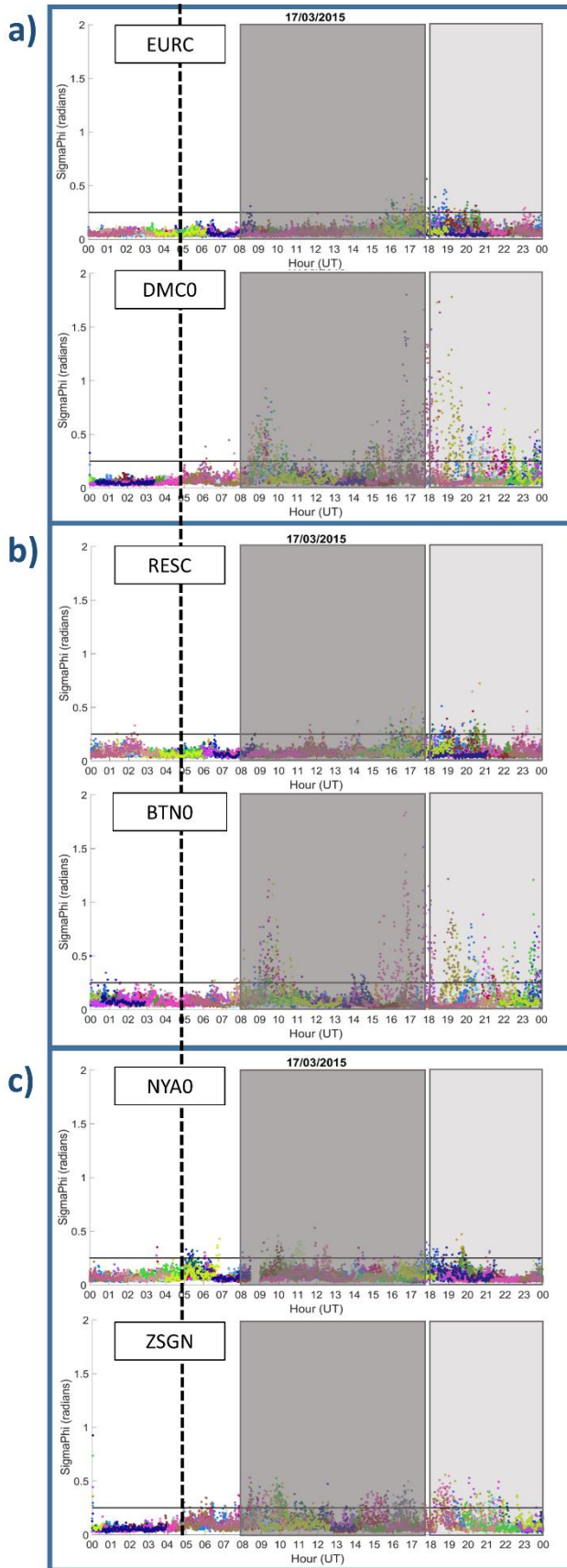


FIGURE 21: Time profiles of σ_ϕ , recorded by EURC and DMC0 (a), RESC and BTNO (b), NYA0 and ZSGN (c) receivers on 2015 March 17. Different colours refer to different satellites in view. The shaded regions indicate the two ICME intervals, while the black dashed vertical line identifies the IP's impact time at the magnetopause. The black horizontal lines characterize the 0.25 radians threshold, which defines the transition from weak (below the line) to strong (above the line) phase scintillation levels.

It is worth noticing that scintillation events principally occur during the first and second ICME arrivals (Liu et al. 2015). Furthermore, during the entire day highly intense and long lasting scintillation activity affects the Antarctic ionosphere (bottom figures in panels a, b). In the cusp the effect is still present even if weaker (panel c). The intensity of the ionospheric response at the different stations revealed by the scintillations appears closely related to the different geomagnetic sectors in the field of view of the selected GNSS receivers. Polar cap stations, DMC0 and BTN0, recorded intense scintillation events between 08:00 and 11:00 UT, with a maximum intensity respectively of ~ 0.95 radians and of ~ 1.25 radians at $\sim 09:30$ UT (bottom plots in panels a and b, respectively). They also recorded a second, much more intense scintillation series starting from 13:30 and up to 24:00 UT, with a maximum intensity of ~ 1.8 radians between 16:00 and 17:00 UT. The DMC0 station (bottom plot in panel a) recorded, at $\sim 19:00$ UT, another very intense scintillation event with a maximum intensity of ~ 1.8 radians. On the other hand, ZSGN (bottom plot in panel c) recorded scintillations roughly at the same hour of the day, but the maximum σ_ϕ intensity level is ~ 0.55 radians, reached at $\sim 08:30$, $10:00$ and $18:30$ UT.

In the Northern Hemisphere, the polar cap stations, EURC and RESC (top plots in panels a and b respectively), recorded a weak scintillation event at $\sim 08:30$ UT on only one satellite in view, with an intensity of about 0.3 radians and 0.25 radians, respectively. The station RESC (top plot in panel b) recorded another weak scintillation event at $\sim 11:50$ UT with an intensity of about 0.3 radians, which involved several satellites in view. The station EURC (top plot in panel a) also recorded scintillations between 15:30 and 20:45 UT, with a maximum intensity of ~ 0.55 radians at $\sim 18:00$ UT, while RESC recorded scintillations mainly concentrated between 15:30 and 21:00 UT, with a maximum intensity of ~ 0.75 radians at $\sim 20:30$ UT. The NYA0 receiver, observing mainly the cusp region, recorded two scintillation series during the day (top plot in panel c). The first occurred between 08:00 and 12:45 UT, with a maximum intensity of ~ 0.55 radians at $\sim 12:00$ UT with a data gap roughly between 08:30 and 09:00 UT. The second occurred between 17:15 and 21:30 UT, with a maximum intensity of ~ 0.50 radians a few minutes before 20:00 UT. The NYA0 receiver recorded another weak scintillation event of ~ 0.35 radians at $\sim 14:15$ UT.

Figure 22 shows the ROT for the same stations and in the same time interval as above. As in Figure 21, the shaded regions identify the ROT behaviour recorded during the first and the second ICME intervals, respectively. It is interesting to note that, in all panels of Figure 22, the most intense and abrupt ROT excursions occur during the two ICME intervals. Furthermore, they occur in correspondence with the scintillation events shown in Figure 21. The ROT excursions recorded during the day by the southern receivers (bottom plots in panel a, b, c of Figure 22) appear to be stronger and longer lasting, as compared to those recorded by the northern receivers. The ROT intensity is weakly dependent on the geomagnetic sectors.

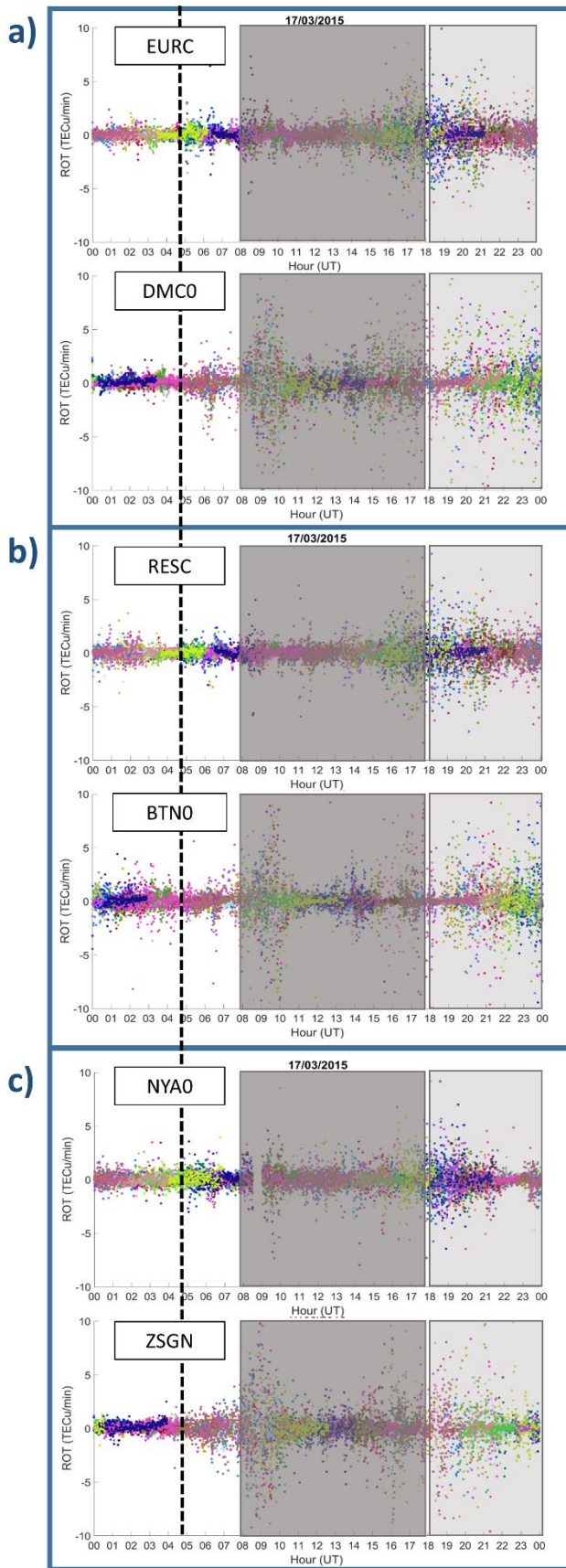


FIGURE 22: Time profiles of Rate of TEC (ROT), recorded by EURC and DMC0 (a), RESC and BTNO (b), NYAO and ZSGN (c) receivers on 2015 March 17. Different colours refer to different satellites in view. The shaded regions indicate the two ICME intervals, while the black dashed vertical line identifies the IPs impact time at the magnetopause.

Figure 23 shows polar-view maps, covering 00:00–24:00 MLT and $|50^\circ|$ – $|90^\circ|$ MLat for northern (top) and southern (bottom) hemispheres. Each map displays an overview of the ionospheric convection patterns (ionospheric electrostatic potential reconstructed from SuperDARN, red/blue isocontours mean positive/negative values of the potential) in the time interval between 08:00–10:00 UT, corresponding to the first significant scintillation peak recorded on March 17 (Figure 21).

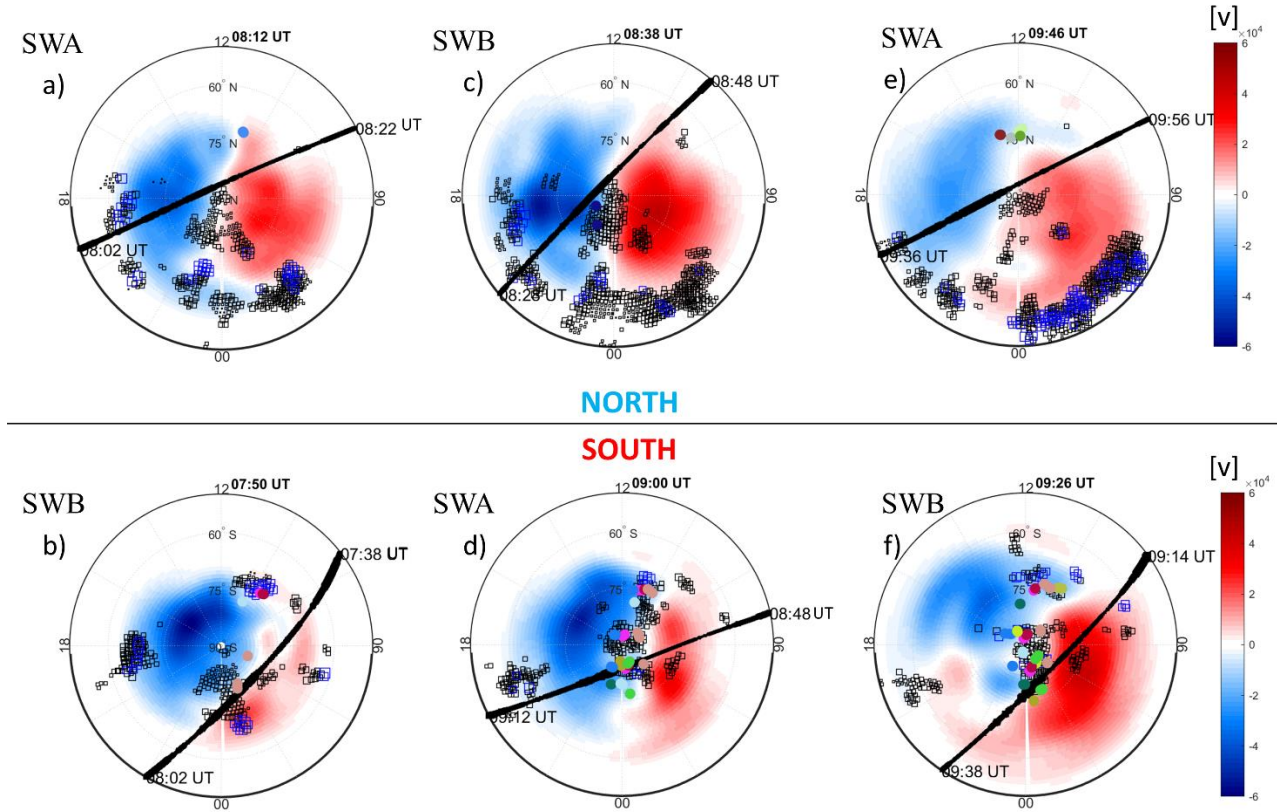


FIGURE 23: Polar-view maps in AACGM coordinates for the northern (top) and southern hemispheres (bottom) between 08:00–10:00 UT of 2015 March 17. Each map shows: isocontours of the ionospheric potential (red=positive, blue=negative potential), recorded in the two minutes following the time shown at the top of each map; SuperDARN measurements of spectral widths less than 200 m/s (black squares) and larger than 200 m/s (blue squares); the electron density (black line) recorded along the orbits of Swarm A (SWA) and B (SWB) satellites; phase scintillations greater than 0.25 radians (coloured dots) recorded simultaneously along the Swarm tracks. In each map, which covers 00:00–24:00 MLT and $|50^\circ|$ – $|90^\circ|$ MLat, magnetic noon/midnight is at the top/bottom.

Each map shows the intensity profile of electron density (black line, whose thickness represents the electron density variation) recorded by Swarm A (SWA) or B (SWB). The projection of ionospheric scintillation, simultaneously recorded by Eureka, Resolute Bay and Ny-Ålesund stations in the northern hemisphere (top panels) and by Concordia, Mario Zucchelli (Terra Nova Bay) and Zhongshan stations in the southern hemisphere (bottom panels) is identified by coloured dots. The SuperDARN observations of spectral width values greater than 200 m/s are highlighted by means of blue squares, while the values less than 200 m/s are represented by black squares. The spectral width larger than 200 m/s is selected as a threshold to distinguish between different plasma regimes in the ionosphere. Such arbitrary threshold is often found in the literature, for separating the ionospheric regions that map on open field lines on the dayside (e.g. the cusp, or the low latitude boundary layer), from regions that map further southward in the oval, on closed field lines (Woodfield et al. 2002). On the night side, large values of spectral width are usually associated with regions characterized by a

wider dispersion of the plasma velocity distribution, e.g. in the presence of vortex structures or plasma shears (e.g. Woodfield et al. 2002, Chisham and Freeman, 2004). The SuperDARN data were collected during the two minute interval following the time reported at the top of each map.

It is interesting to note (Figure 23) that scintillations mainly occurred at cusps, well identified by the reconstruction of the convection configuration given by SuperDARN data, and in the ionospheric region between the two convection cells in both hemispheres. This region has been often identified to host the ionospheric irregularities causing scintillations (see, e.g., De Franceschi et al 2008; Mitchell et al 2005; Moen et al. 2013). In the southern hemisphere (panels b, d and f, respectively) scintillations seem to spread over a wider area of the ionosphere with respect to the northern hemisphere (panels a, c and e, respectively). In the southern hemisphere scintillations appear both in correspondence with steep gradients of electron density (identified by the enhanced thickness of the Swarm trace) and large spectral width values (blue squares). The latter are mainly concentrated in the polar cap and in the cusp regions of the southern hemisphere, and in the night side of the auroral oval of the northern hemisphere. The reconstruction of the electric potential is mainly driven by spectral width measurements, ensuring a realistic description of the related pattern in the maps. The overall convection patterns, in both hemispheres, are consistent with a scenario characterized by a negative $B_{z,IMF}$ (Heppner and Maynard 1987; Weimer 2005; Ruohoniemi and Greenwald 2005; Pettigrew et al. 2010; Haaland et al. 2007), with the convection cells tilted towards noon by the effect of a mainly null $B_{y,IMF}$ (panels c and d in Figure 17).

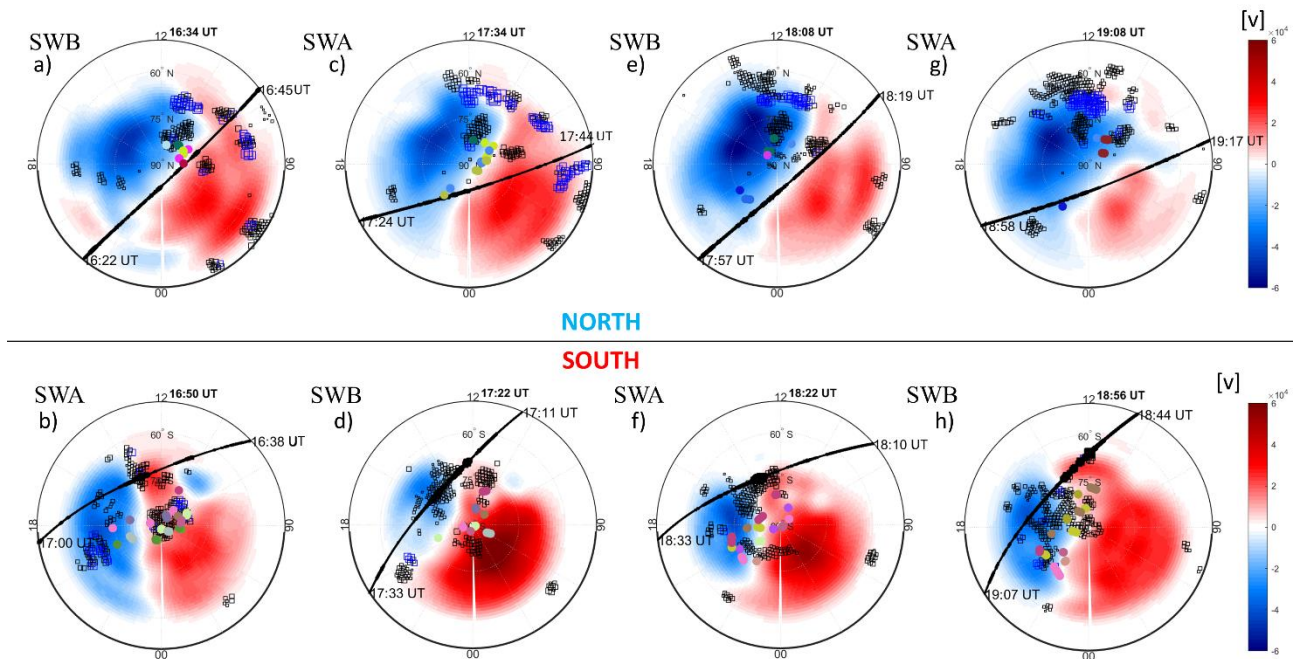


FIGURE 24: Polar-view maps in AACGM coordinates for the northern (top) and southern hemispheres (bottom) between 16:00-20:00 UT of 2015 March 17. Each map shows: the isocontours of the ionospheric potential (red=positive, blue=negative potential), recorded in the two minutes following the time shown at the top of each map; SuperDARN measurements of spectral widths less than 200 m/s (black squares) and larger than 200 m/s (blue squares); the electron density (black line) recorded along the orbits of Swarm A (SWA) and B (SWB) satellites; phase scintillations greater than 0.25 radians (coloured dots) recorded simultaneously along the Swarm tracks. In each map, which covers 00:00-24:00 MLT and $|50^\circ|$ - $|90^\circ|$ MLat, the magnetic noon/midnight is at the top/bottom.

As for Figure 23, Figure 24 shows the polar-view maps for northern (top) and southern (bottom) hemispheres in the time interval 16:00 to 20:00 UT (i.e. when the second significant scintillation peak occurred, see Figure 21). Such figure shows results very similar to Figure 23. In fact, in both hemispheres, scintillations mainly occurred in the ionospheric region between the two convection cells together with high spectral width values (blue squares). The latter are observed mainly in the cusp in the northern hemisphere, while they are recorded mainly at the polar cap and at lower latitudes in the evening sector of the southern hemisphere. Moreover, the scintillation affecting the northern hemisphere appears in correspondence with electron density gradients (identified by the enhanced thickness of the Swarm trace in panels a, c, e and g). These appear steeper in the southern hemisphere compared with the northern hemisphere (panels b, d, f and h). The overall convection patterns, in this case, are coherent with a scenario dominated by $B_{z,IMF}$ predominantly negative, with convection cells tilted towards dawn in both hemispheres by the effect of a mainly positive $B_{y,IMF}$ (panels c and d in Figure 17).

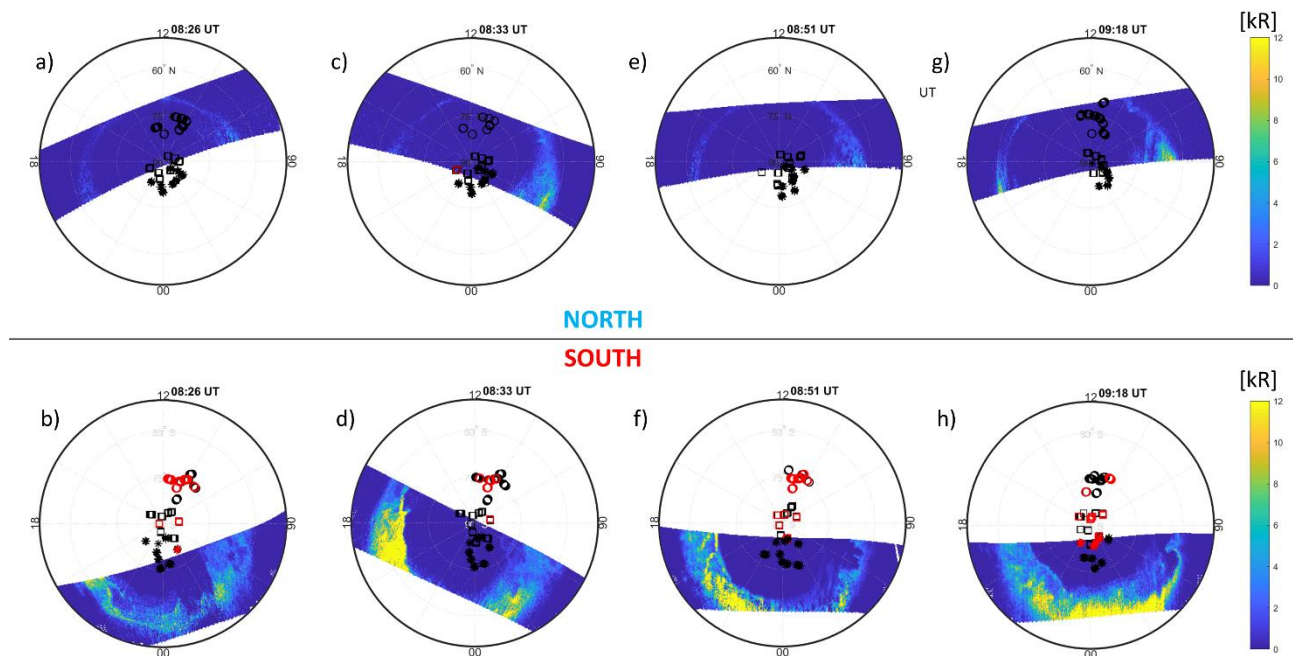


FIGURE 25: Polar-view maps in AACGM coordinates for the northern (top) and southern hemispheres (bottom) for data recorded between 08:00-10:00 UT of 2015 March 17. Each map shows for each hemisphere the auroral radiance as measured by DMSP satellites and the phase scintillations both greater than 0.25 radians (red symbols) and less than 0.25 radians (black symbols), recorded simultaneously along the DMSP tracks. For the northern maps, circles indicate scintillations recorded by NYAO, squares indicate scintillations recorded by EURC, while stars identify scintillations recorded by RESC. For the southern maps, circles indicate scintillations recorded by ZSGN, squares indicate scintillations recorded by DMC0, while stars identify scintillations recorded by BTN0. In each map, which covers 00:00-24:00 MLT and $|50^\circ|$ - $|90^\circ|$ MLat, the magnetic noon/midnight is at the top/bottom.

Figure 25 shows polar-view maps, covering all MLT (00:00–24:00) and the $|50^\circ|$ - $|90^\circ|$ MLat sector for northern (top) and southern (bottom) hemispheres. Each map displays the auroral radiance as measured by DMSP satellites in the time interval between 08:00-10:00 UT, corresponding to the first significant scintillation peak recorded on March 17 (Figure 21). In order to understand if the particles precipitating in the auroral oval may have caused the observed scintillations, the maps also show phase scintillations greater than 0.25 radians (red symbols) and less than 0.25 radians (black symbols),

recorded simultaneously along the DMSP tracks. In particular, each map shows the projection of ionospheric scintillations, simultaneously recorded by the Eureka, Resolute Bay and Ny-Ålesund stations in the northern hemisphere (top panels) and by Concordia, Mario Zucchelli (Terra Nova Bay) and Zhongshan stations in the southern hemisphere (bottom panels). The choice to include scintillation values lower than 0.25 radians allows the identification of the field of view of each GNSS receiver along the DMSP track. This enables a comparative analysis to show the correlation between scintillation occurrence and particles precipitation into the auroral oval. Such maps show that in the interval 08:00-10:00 UT the fields of view of the selected receivers were unable to cover the auroral region in both hemispheres. For this reason, it is not possible to correlate the observed scintillation to particle precipitation into the auroral oval.

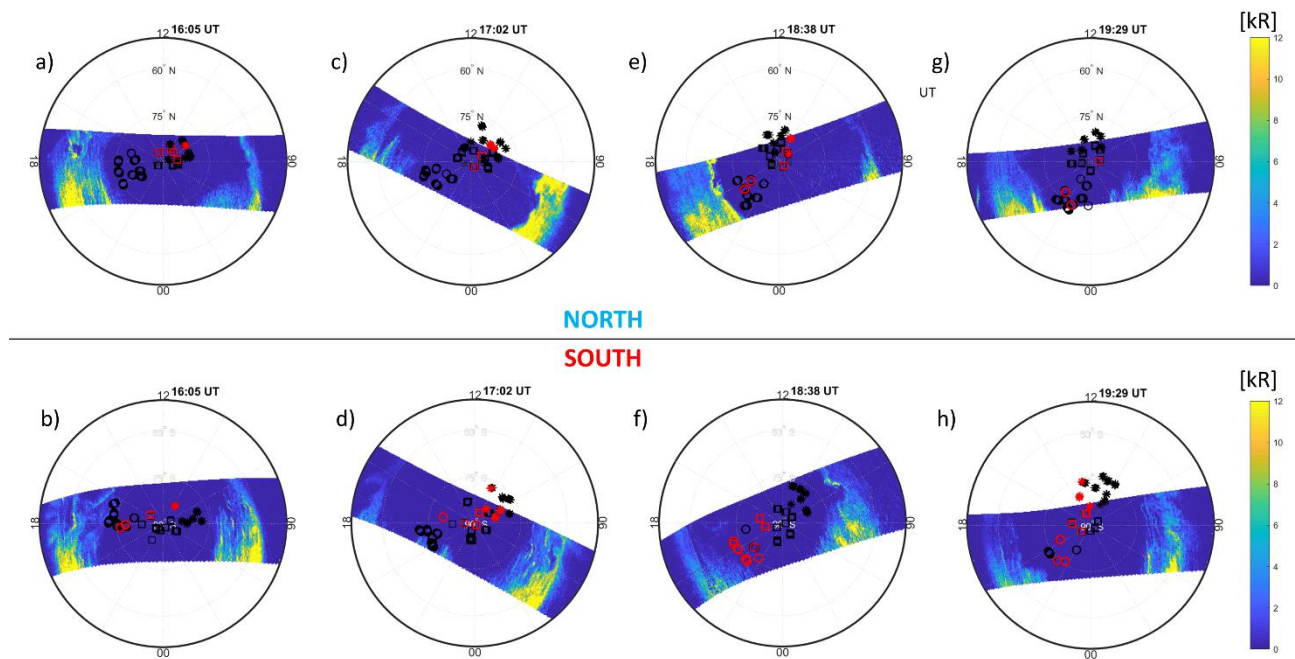


FIGURE 26: Polar-view maps in AACGM coordinates for the northern (top) and southern hemispheres (bottom) between 16:00-20:00 UT of 2015 March 17. Each map shows for each hemisphere the auroral radiance as measured by DMSP satellites and the phase scintillations both greater than 0.25 radians (red symbols) and less than 0.25 radians (black symbols), recorded simultaneously along the DMSP tracks. In particular, in the northern maps, circles identify scintillations recorded by NYA0, squares identify scintillations recorded by EURC, while stars identify scintillations recorded by RESC. In the southern maps, circles identify scintillations recorded by ZSGN, squares identify scintillations recorded by DMC0, while stars identify scintillations recorded by BTN0. Each map covers 00:00-24:00 MLT and $|50^\circ|$ - $|90^\circ|$ MLat, the magnetic noon/midnight is at the top/bottom.

As for Figure 25, Figure 26 shows polar-view maps of the auroral radiance as measured by DMSP satellites in the time interval 16:00-20:00 UT, corresponding to the second scintillation peak recorded on March 17 (Figure 21). Also in this case, the fields of view of the selected receivers were unable to cover the auroral region in both hemispheres. For this reason, it is not possible to verify whether the particles precipitating into the auroral oval caused the observed scintillation.

Figure 27 shows the time profile of the *rms* of the ionospheric *in-situ* electron density measured by Swarm A (SWA, circles) and Swarm B (SWB, stars) during March 17, at high latitudes within 50° of magnetic latitude.

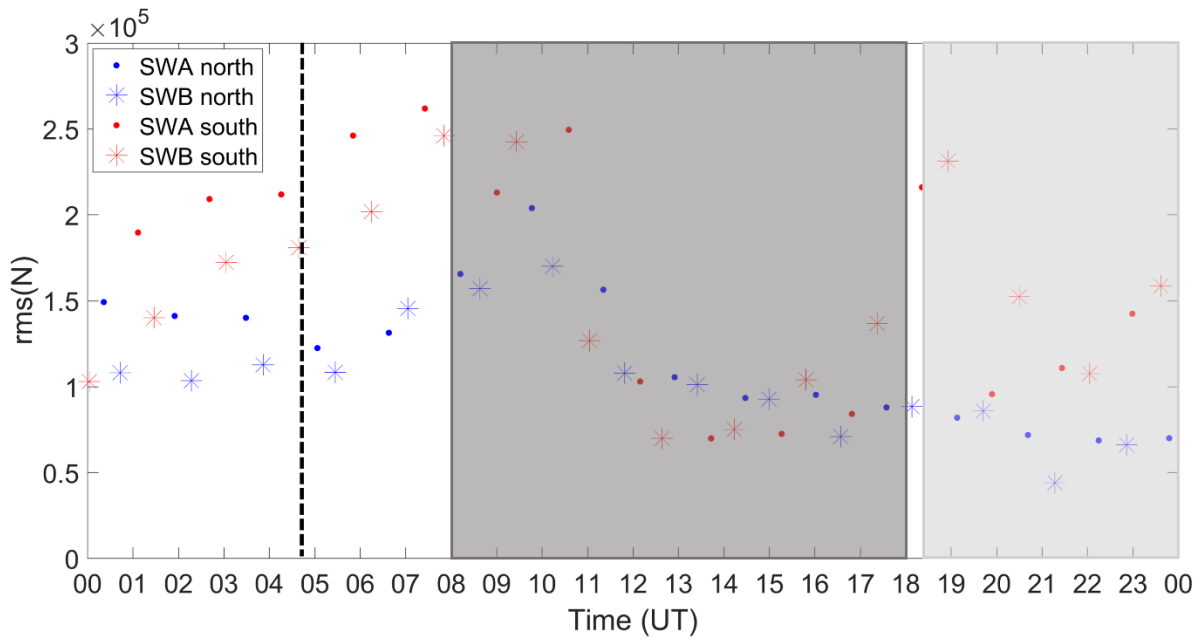


FIGURE 27: Electron density root mean square (rms) calculated from measurements acquired by Swarm A (circles) and Swarm B (stars) during 2015 March 17. Blue series refers to measurements in the northern hemisphere, while red series refers to measurements in the southern hemisphere. The Magnetic Latitude ranges between $|50^\circ|$ and $|90^\circ|$. The dashed vertical line marks the IPs arrival at the magnetopause and the shaded areas evidence the ICMEs arrivals.

In the southern hemisphere (red), the rms values are larger than in the northern hemisphere (blue), especially at the arrival of the IPs (black dashed line) and the ICMEs (shaded areas). Nevertheless, rms values in the southern (red) and in the northern hemisphere (blue) are comparable before the arrival of solar perturbations, between 00:00 and 04:50 UT, and in conjunction with the positive switch of the z component of the IMF between 10:00 and 16:00 UT ($B_{z,IMF}$ Figure 17d). Furthermore, between 00:00 and 13:00 UT, Swarm A measured, in the southern hemisphere, rms values (red circles) larger than those measured by Swarm B (red stars), except between 08:00 and 10:00 UT, when the opposite is observed. Starting from 15:00 UT, the Swarm B rms values are larger than those measured by Swarm A. In the northern hemisphere, even if before 04:00 UT the Swarm A rms values (blue circles) were larger than the Swarm B values (blue stars), the two satellites recorded roughly comparable values until the end of the day.

4.2 THE 2015 JUNE STORM

The event that occurred from 21 to 24 June 2015 was one of the most intense geomagnetic storms of the 24th solar cycle. Beside its intensity, the peculiarity of the storm lies in its occurrence during the summer solstice and the superposition of several solar events. It was caused by a series of three interplanetary shocks hitting the Earth's magnetosphere at 16:45 UT on June 21, at 05:45 UT on June 22 and at 18:30 UT on June 22, 2015, respectively. In contrast to the 2015 St. Patrick's storm that was caused by multiple ICMEs, all the June shocks resulted from single ejecta (Liu et al., 2015). For this reason, this storm constituted a powerful test bench to study the role of different solar drivers in scintillation production.

4.2.1 RESULTS

Figure 28 shows, from top to bottom, the UT variations of the IMF amplitude ($|B|_{IMF}$), the IMF B_x component ($B_{x,IMF}$), the IMF B_y component ($B_{y,IMF}$), the IMF B_z component ($B_{z,IMF}$), the solar wind

density (ρ_{sw}), proton temperature (T), velocity (V_{sw}) and dynamic pressure (P), acquired by WIND from 21 to 24 June 2015. It also shows the UT variations of the SYM-H index, the auroral oval (AU and AL) and the polar cap (PCN and PCS) indices recorded in the same days. The shaded region indicates the ICME interval and the dashed vertical lines mark the shocks arrivals at WIND.

As reported by several authors (see e.g. Astafyeva et al., 2017; Piersanti et al., 2017; Cherniak and Zakharenkova, 2017) and also shown in Figure 28, the first shock (black dashed line), accompanied by sharp changes in the solar wind density (panel e), temperature (panel f) and speed (panel g), compressed the Earth's magnetosphere and caused a sudden increase of SYM-H of ~ 40 nT (panel i). In addition, the north-south component of the IMF ($B_{z,IMF}$) remained mostly positive at the shock arrival (panel d), and no substorm activity followed (panel l). Only the PCN index (blue, panel m) showed an enhancement in the magnetic activity of the northern polar cap following the arrival of the first shock.

The second shock (red dashed line) was accompanied by a small solar wind density increase (panel e), causing an enhancement in SYM-H of ~ 20 nT (panel i). At the shock's arrival, the $B_{z,IMF}$ turned negative (panel d) causing a sharp enhancement of auroral activity, as visible in panel l. Then, $B_{z,IMF}$ fluctuated around zero until the arrival of the third shock (panel d) and a smaller decrease in the SYM-H index was observed (~ -40 nT, panel i). The last shock (green dashed line), accompanied by a large and sudden increase in solar wind and IMF components, caused a large and sudden increase in SYM-H up to ~ 88 nT at 18:37 UT (e.g., storm sudden commencement, panel i). The ejecta following this shock was characterized by a large negative $B_{z,IMF}$ (-39 nT, panel d), that caused a decrease of the SYM-H index to -208 nT (on June 23, panel i) and, consequently, strong auroral and polar activity (panels l and m, respectively). Such conditions led to unusual responses of the ionosphere-thermosphere system in both interhemispheric asymmetries and latitudinal differences.

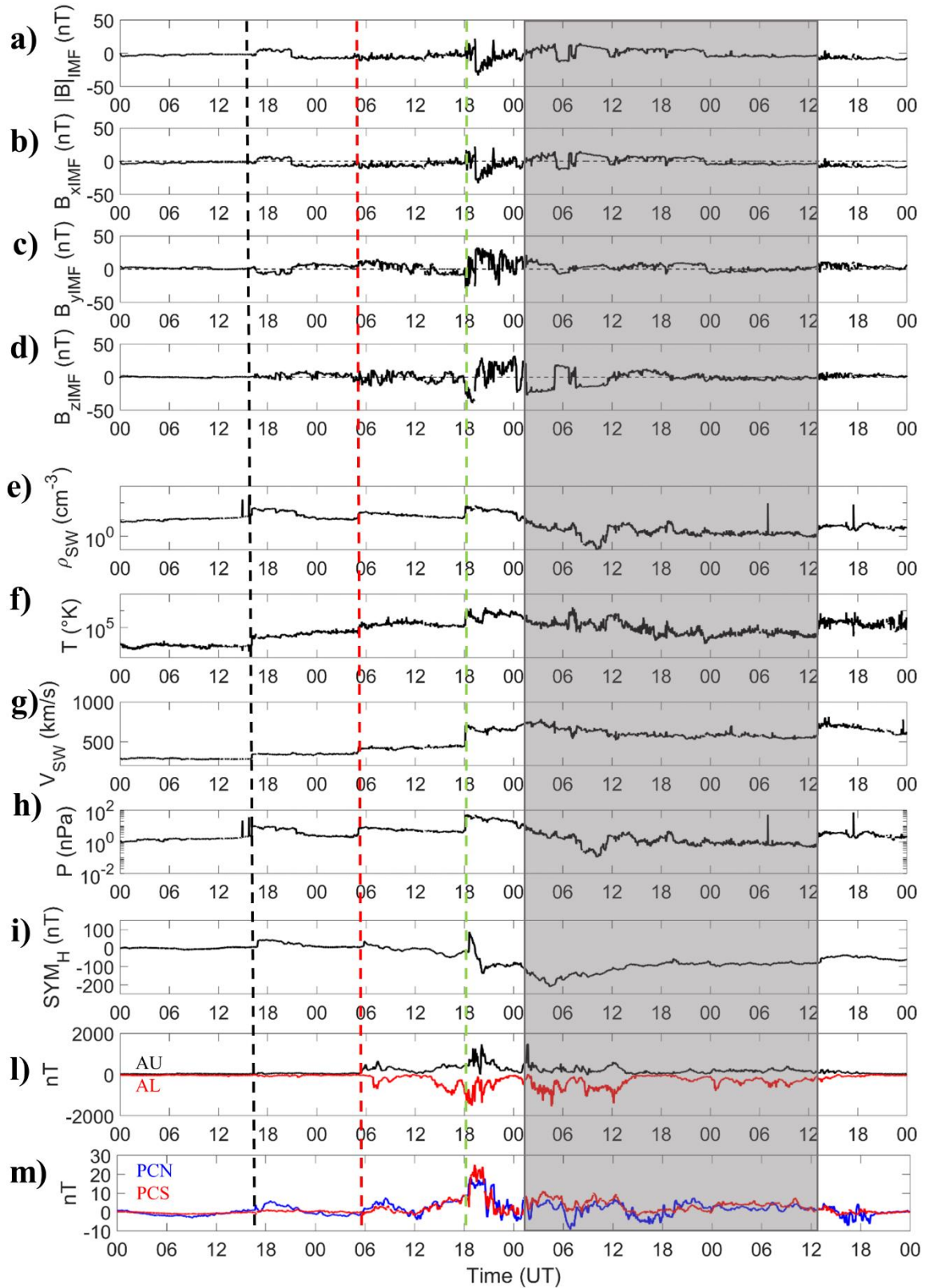


FIGURE 28: Solar wind (SW) observations (WIND spacecraft) and the geomagnetic response at low and high latitudes for 2015 June 21-24. From top to bottom: (a) IMF amplitude $|B|_{\text{IMF}}$; (b) IMF $B_{x,\text{IMF}}$ component; (c) IMF $B_{y,\text{IMF}}$ component; (d) IMF $B_{z,\text{IMF}}$ component; (e) SW density ρ_{SW} ; (f) SW proton temperature T_{SW} ; (g) SW velocity V_{SW} ; (h) SW dynamic pressure P ; (i) SYM-H index; (l) AU (black line) and AL (red line) indices; (m) Polar Cap North (PCN, blue) and Polar Cap South (PCS, red). The shaded region indicates the ICME interval and the dashed vertical lines mark the three shock arrivals at WIND (black the first, red the second, green the third, respectively).

The multi-instrumental studies by Prikryl and co-authors (2011, 2013 and 2015), highlighted how the main asymmetries are due to the IMF dawn–dusk component, being responsible for the cusp location, and of the main orientation of plasma convection within the polar cap. The combination of both effects results in a different occurrence of plasma patches between the two hemispheres, causing significant differences in the scintillation patterns over both high-Arctic regions and Antarctica. However, the solstice conditions, under which the 2015 June storm occurred, make the explanation of the inter-hemispheric asymmetry and latitudinal development very challenging, as reported in recent literature (Astafyeva et al., 2016; Mansilla, 2017; Cherniak and Zakharenkova, 2017). In fact, Mansilla (2017), which performed a global study of the ionospheric Total Electron Content (TEC) from high to low latitudes during this storm, observed asymmetries of the TEC response in both hemispheres. He observed a TEC increase in the southern hemisphere well correlated with the increase of the O/N₂ ratio. Correspondingly, he observed a decrease in the northern hemisphere, not associated with a decrease in O/N₂ ratio. In addition, Astafyeva et al. (2016) analysed variations of the ionospheric vertical TEC and electron density in the topside ionosphere during the initial and main phases of the storm. They observed a pronounced hemispheric asymmetry in the night time topside ionosphere. Specifically, in the northern hemisphere (summer), they observed an extreme enhancement in ionospheric vertical TEC and electron density attributed to the combination among the prompt penetration electric fields (which is driven by the leakage of high-latitude convection electric fields to low latitudes (e.g., Huang et al. 2005; Kikuchi et al. 2008)), the disturbance dynamo and the storm-time thermospheric circulation. Cherniak and Zakharenkova (2017), investigated the ionospheric irregularities using a chain of Global Navigation Satellite System (GNSS) receivers located in both hemispheres from middle to high latitudes and found a correlation between the occurrence of ionospheric irregularities and the variations of the AE and the SYM-H indices.

To provide further insights about the physical mechanisms leading to irregularity formation and their effect on GNSS satellites, this study focuses on June 22, when the bulk of the storm-driven ionospheric disturbances were observed.

In order to reconstruct the shape of the Earth’s magnetosphere following the impacts of the two shocks on June 22, the shock normal orientations were estimated by applying the Rankine Hugoniot’s conditions on solar wind data. The resulting parameters for both shocks are reported in Table 2.

TABLE 2: Interplanetary shocks parameters. Table a (red) shows the resulting parameters of the first shock, while table b (green) lists the parameters of the second shock.

a) First IPs parameters		b) Second IPs parameters	
IP shock’s normal latitude (GSE):	$\theta = 150.4^\circ$	IP shock’s normal latitude (GSE):	$\theta = 173.6^\circ$
IP shock’s normal longitude (GSE):	$\phi = 112.2^\circ$	IP shock’s normal longitude (GSE):	$\phi = 99.8^\circ$
IP shock’s speed:	$V_{IP} = 450 \text{ km/s}$	IP shock’s speed:	$V_{IP} = 767 \text{ km/s}$
IP shock’s impact point at magnetopause:	$X_{imp_{GSE}} = 10.7 R_E$ $Y_{imp_{GSE}} = 1.8 R_E$	IP shock’s impact point at magnetopause:	$X_{imp_{GSE}} = 8.9 R_E$ $Y_{imp_{GSE}} = 6.9 R_E$

Table 2a (red) lists the first shock parameters, while Table 2b (green) lists the second shock parameters. According to these parameters, the shocks lied almost in the ecliptic plane and hit the magnetopause almost at noon (Villante et. al, 2008; Alberti et al. 2016; Piersanti et al. 2016).

Figure 29 shows the configuration of the magnetospheric field in the noon/midnight plane before (black lines) and after the first (red) and the second (green) shock on June 22, evaluated by a modified version of the TS04 model. In this case-study, the TS04 model was modified taking into account the intensification of the ring current as described by Piersanti et al. (2017). As shown in Figure 29, the impact of the first shock did not lead to a significant reconfiguration of the magnetospheric field. The second shock impact causes an extreme compression of the field on the dayside and stretching on the nightside, with significant southward lowering of the dayside magnetosphere and a northward raising of both lobes of the tail.

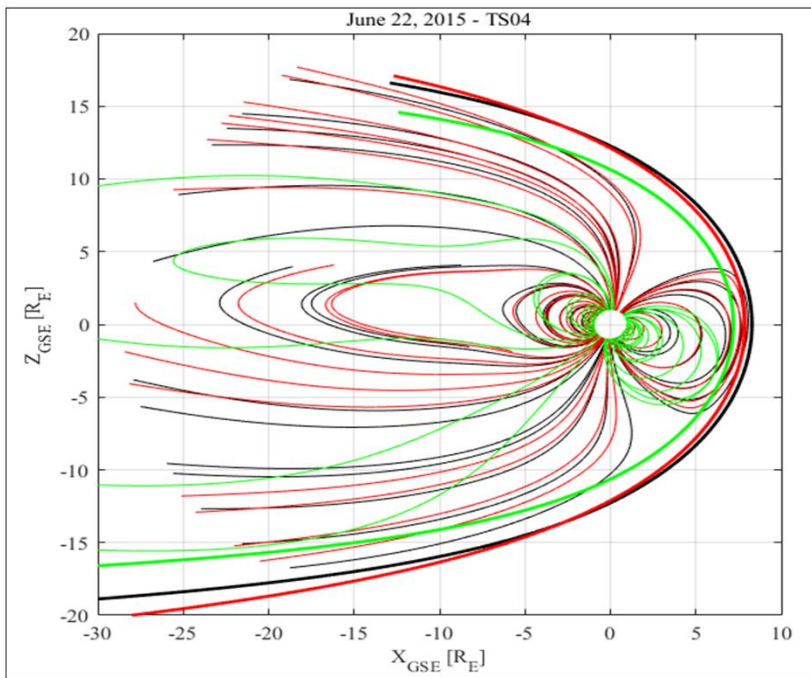


FIGURE 29: Magnetospheric field configuration before (black) and after the first (red) and the second (green) shock on June 22. Black, red and green thick lines identify, respectively, the magnetopause before and after the shock arrivals.

Figure 30 shows polar-view maps of the FACs density in the northern (top maps) and the southern (bottom maps) hemisphere between 05:30 UT and 05:50 UT on 2015 June 22 from IRIDIUM satellites observations. The time range includes ten minutes before and after the first IPs impact onto the magnetopause. These maps show that before the IPs arrival (05:30 UT), the current density in the northern hemisphere (top map on the left) was higher than the southern hemisphere (bottom map on the left). This result is in accordance with Coxon et al. (2016) and references therein claiming that the FACs system experiences seasonal variations, with more current flowing in the northern (southern) hemisphere during Bartels rotations (which is the apparent rotations of the Sun as viewed from Earth that has a length of exactly 27 days) in northern (southern) summer. Starting from 05:40 UT (IPs impact time), an intensification of the cusp currents (between 70° and 80° MLat) was observed in both hemispheres, although it was more visible at 05:50 UT. This was due to the fact that the first IPs hits the Earth’s magnetopause at 05:45 UT, but the current density in these maps is averaged over ten minutes. Hence, maps at 05:50 take into account also the pre-shock conditions. In addition, after the IPs arrival, currents flowing out the ionosphere (red currents) appeared more

intense than the currents flowing toward the ionosphere, especially in the southern hemisphere (middle and right bottom maps). This is in agreement with the positive values of $B_{z,IMF}$ observed at the IPs arrival (see panel d in Figure 28), which, causing a compression of the magnetosphere, led the plasma to escape from the ionosphere. The results agree with the first shock parameters (Table 2a), locating the impact point slightly lower than the ecliptic plane in the southern hemisphere.

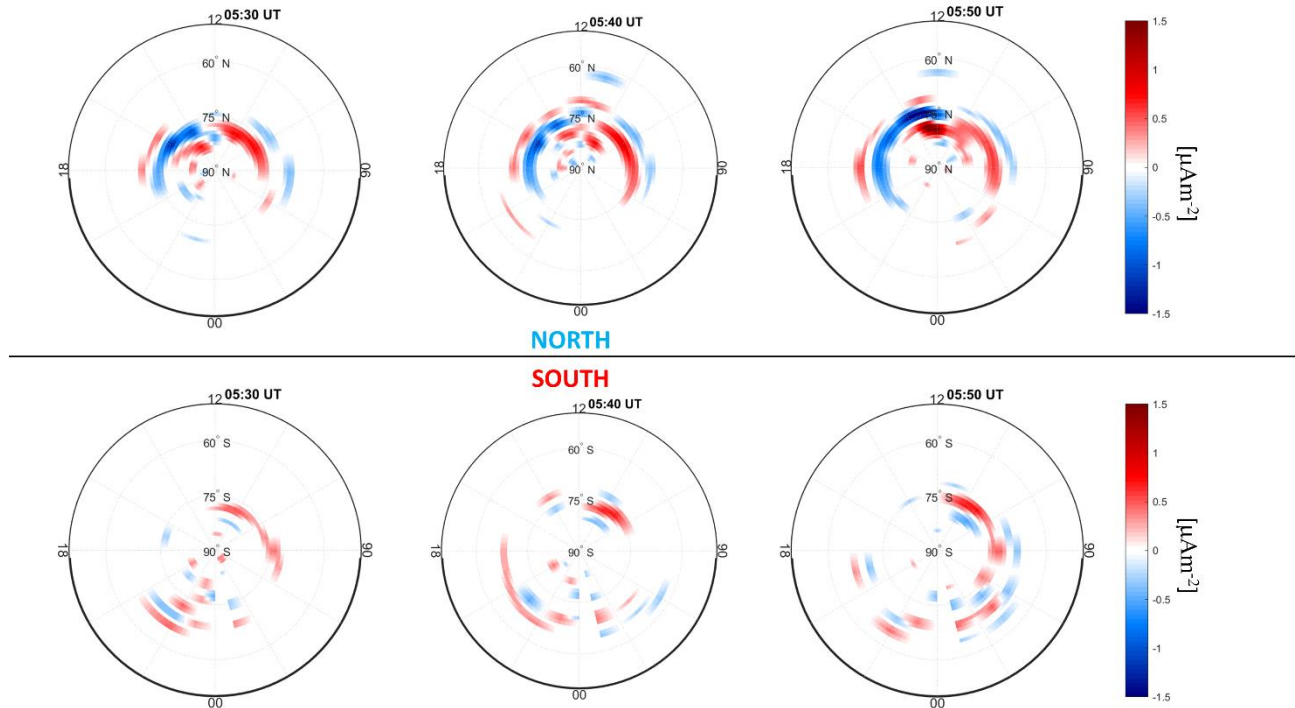


FIGURE 30: Polar-view maps of the current density of the FACs system in northern (top) and southern (bottom) hemispheres between 05:30 UT and 05:50 UT on 2015 June 22.

Figure 31 shows polar-view maps of the FACs density in the northern (top) and the southern (bottom) hemisphere between 18:20 UT and 18:40 UT on 2015 June 22 derived from IRIDIUM satellites observations. The time range includes ten minutes before and after the time of the second IPs impact on the magnetopause. The maps show an activity of FACs system before the shock impact on the magnetopause in both hemispheres (left maps at 18:20 UT), although, according to the seasonal variations of such current system, it is more pronounced in the northern hemisphere compared with the southern. This activity is consistent with the negative values of $B_{z,IMF}$ observed just before the IPs arrival (see panel d in Figure 28). In correspondence with the shock impact (18:30 UT), an enhancement of currents flowing into (blue currents) and out (red currents) of the ionosphere was observed in both hemispheres. This is in agreement with the negative values of $B_{z,IMF}$ observed at the IPs arrival (see panel d in Figure 28). Such enhancement had roughly the same intensity in both hemispheres.

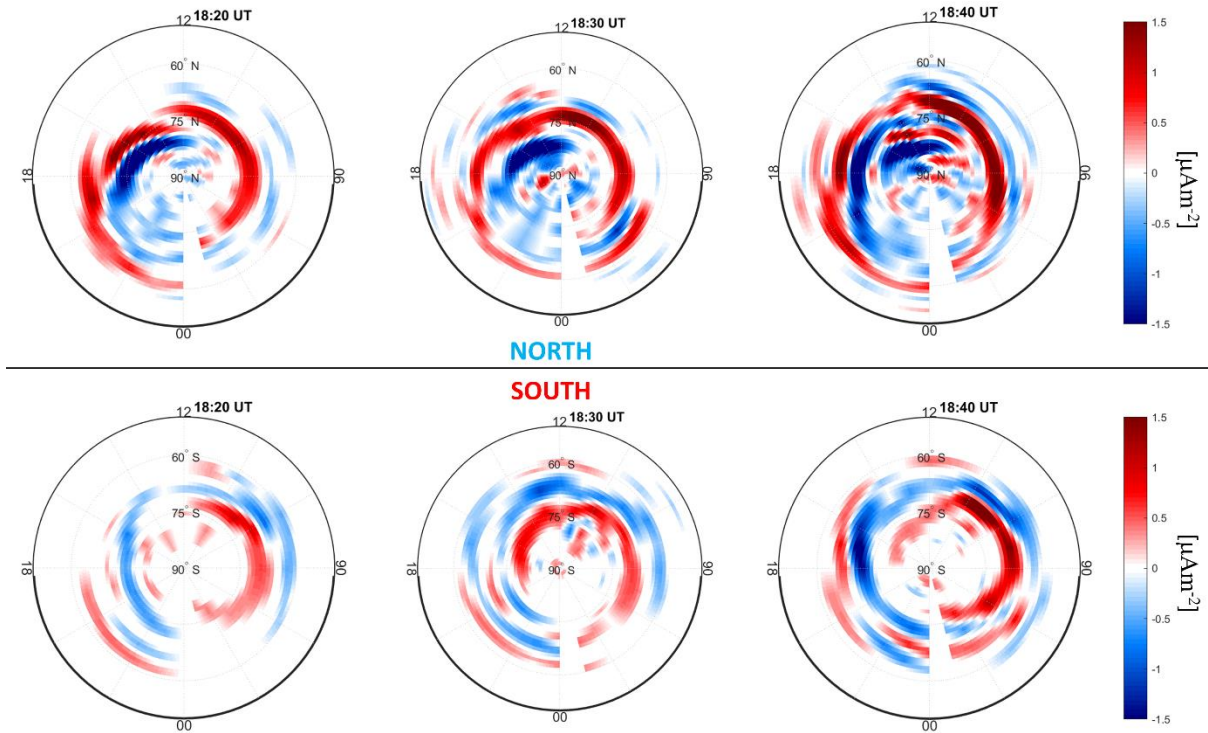


FIGURE 31: Polar-view maps displaying the current density of the FACs system in northern (top) and southern (bottom) hemisphere between 18:20 UT and 18:40 UT on 2015 June 22.

Figure 32 shows the time profile of σ_ϕ recorded at EURC and DMC0 (panel a), RESC (panel b), NYA0 and ZSGN (panel c) on 2015 June 22. Panels a and c show the comparison between northern and southern GNSS observations recorded at ground receivers, which look, under quiet geomagnetic conditions, roughly conjugated (in the Earth's magnetic field reference frame) ionospheric regions. The black horizontal lines indicate the 0.25 radians σ_ϕ threshold. The dashed vertical lines mark the arrival at the Earth's magnetopause of the first (red) and the second interplanetary shocks (green) on June 22. Different colours refer to different satellites in view. TEC and scintillation parameters provided by the BTN0 receiver were not available for this case study.

All the scintillation events were recorded after the arrival of both the interplanetary shocks and appeared longer lasting in the southern hemisphere. In addition, the EURC receiver did not record significant scintillation events during the day, while the RESC receiver, although located at few magnetic latitude degrees southward than EURC (Table 1 in section 2.2), recorded three scintillation events at $\sim 20:45$ UT, $\sim 22:00$ UT and $\sim 23:30$ UT with mean intensities of ~ 0.50 radians, of ~ 0.60 radians and of ~ 0.42 radians, respectively. The DMC0 receiver recorded two scintillation series between $\sim 08:00$ UT and 10:00 UT and between $\sim 19:00$ UT and 23:00 UT, with mean intensities of ~ 0.45 radians and of ~ 0.57 radians, respectively. The NYA0 and ZSGN σ_ϕ time profiles showed similar behaviours during the entire day, even if the receiver at ZSGN recorded more intense scintillation events than NYA0.

Figure 33 shows the ROT time profiles for the same stations and in the same time interval as in the previous figure. Also in this case, the dashed vertical lines mark the arrival at the magnetopause of the first (red) and second (green) interplanetary shocks and different colours refer to different satellites in view. The most intense and sudden ROT excursions were recorded after the arrival of the two interplanetary shocks, as visible in all panels of Figure 33. Such excursions appear longer lasting

and more intense in the southern hemisphere and after the arrival of the second interplanetary shock. They also occurred mainly in correspondence with the scintillation events shown in Figure 32.

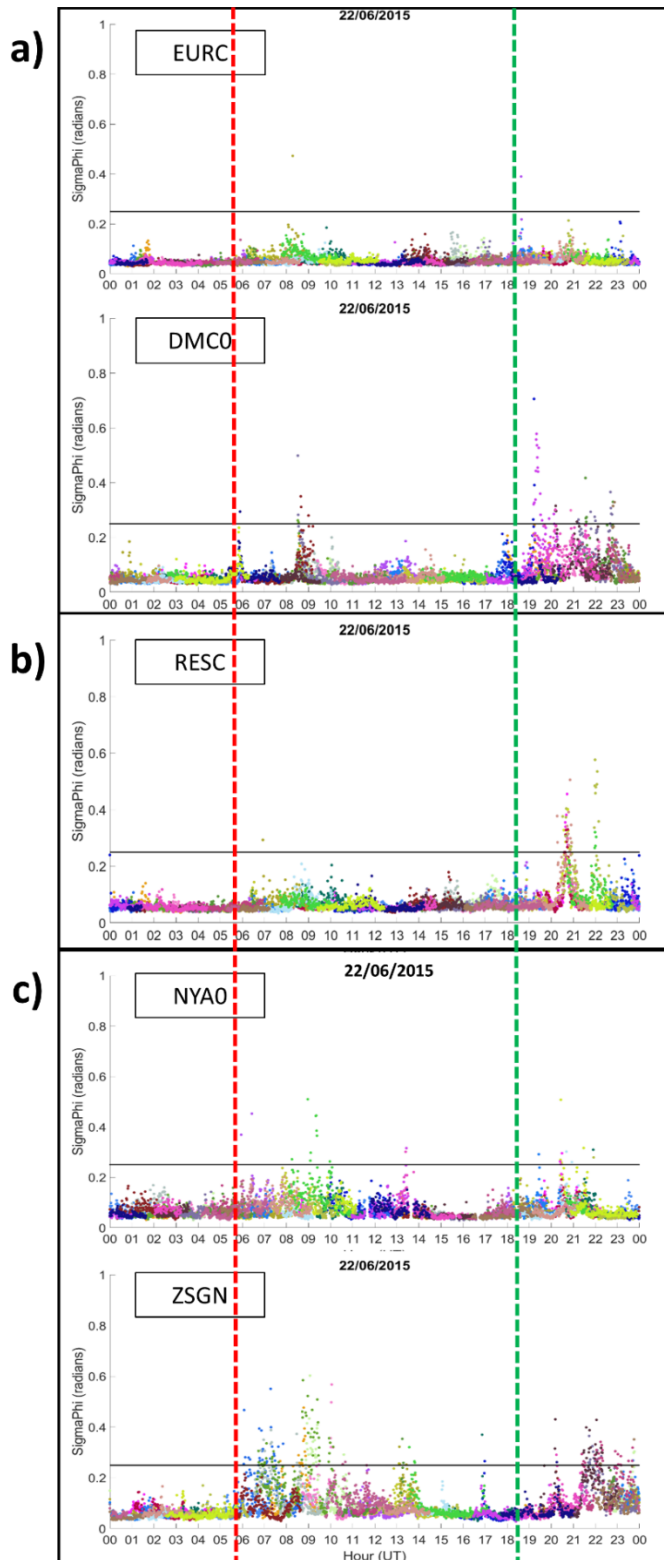


FIGURE 32: Time profiles of σ_{ϕ} recorded at EURC and DMC0 (a), RESC (b), NYA0 and ZSGN (c) receivers during 2015 June 22. Different colours refer to different satellites in view. The dashed vertical lines mark the arrival at the magnetopause of the first (red) and the second interplanetary shocks (green). The black horizontal lines characterize the 0.25 radians threshold, which defines the transition from weak (below the line) to strong (above the line) phase scintillation levels.

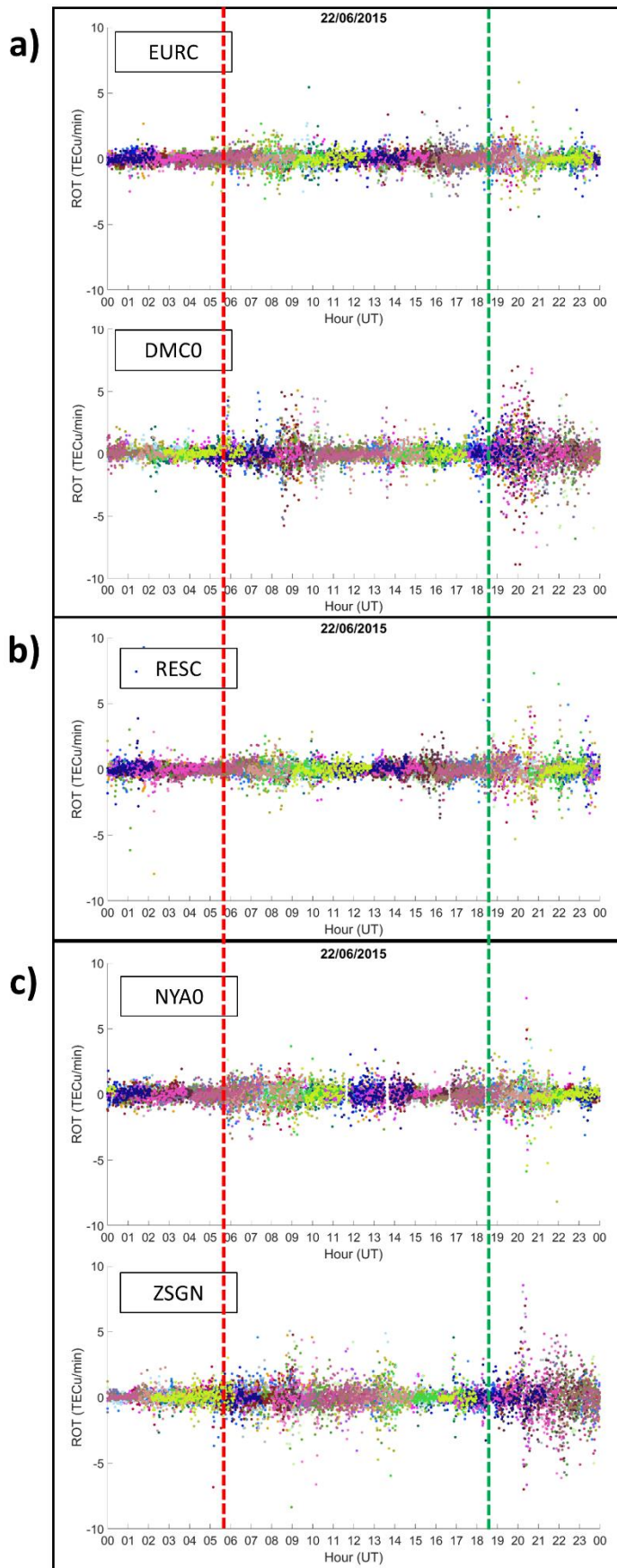


FIGURE 33: Time profiles of ROT, recorded at EURC and DMC0 (a), RESC (b), NYA0 and ZSGN (c) receivers, during 2015 June 22. Different colours refer to different satellites in view. The dashed vertical lines mark the arrival at the magnetopause of the first (red) and the second interplanetary shocks (green).

Figure 34 shows polar view maps, covering the $|50^\circ|$ – $|90^\circ|$ MLat sector and the interval 00:00–24:00 MLT for the northern (top) and the southern (bottom) hemispheres. Each map displays an overview of the ionospheric convection patterns in the time interval 07:00–10:00 UT, corresponding to the first significant scintillation peak recorded on June 22 (Figure 32). The intensity profile of the electron density (black line, whose thickness indicates the electron density variation) recorded by Swarm A (SWA) or B (SWB); the projection of ionospheric scintillation (colour dots), simultaneously recorded by Eureka, Resolute Bay and Ny-Ålesund stations in the northern hemisphere (top panels) and by Concordia, Mario Zucchelli (Terra Nova Bay) and Zhongshan stations in the southern hemisphere (bottom panels) and all SuperDARN observations of spectral widths with values greater than 200 m/s are plotted as blue squares and values less than 200 m/s are shown by black squares are shown in each map. As for the previous case study (see section 7) spectral width values larger than 200 m/s is identified as a threshold to distinguish between different plasma regimes in the ionosphere.

Figure 34 confirms that scintillation originated in the cusp region of both hemispheres. Moreover, large spectral width values (blue squares) were recorded, in the northern hemisphere, mainly in the early pre-dawn sector of the auroral oval (around 3 MLT, panels a and e), while, in the southern hemisphere, they were recorded mainly in the cusp and between the two convection cells (panels b and d). The overall convection patterns, both in the northern and in the southern hemispheres, are consistent with a scenario dominated by $B_{z,IMF}$ predominantly negative, with convection cells tilted towards dawn by the effect of a mainly positive $B_{y,IMF}$ (panels c and d in Figure 28).

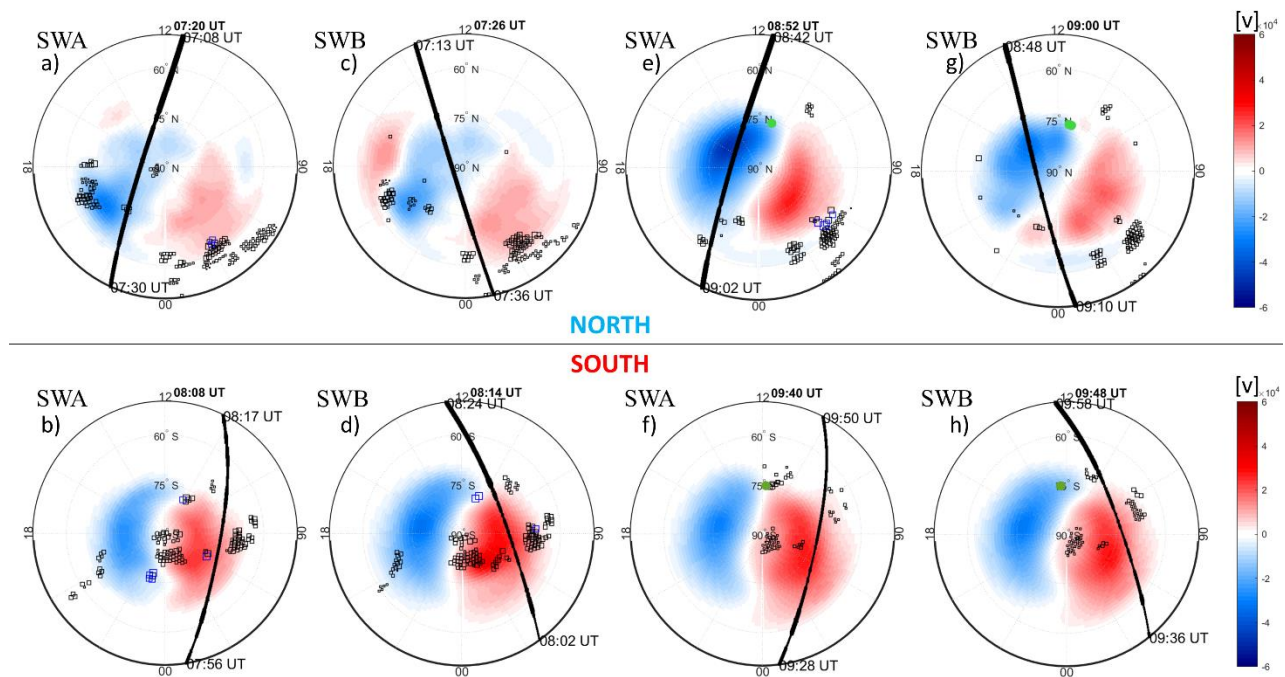


FIGURE 34: Polar-view maps in AACGM coordinates for the northern (top) and southern hemispheres (bottom) between 07:00–10:00 UT of 2015 June 22. Each map shows: isocontours of the ionospheric potential (red=positive, blue=negative potential), in the two minutes following the time shown at the top of each map; SuperDARN measurements of spectral widths less than 200 m/s (black squares) and larger than 200 m/s (blue squares); electron density (black line) recorded along the orbits of Swarm A (SWA) and B (SWB) satellites; phase scintillations greater than 0.25 radians (coloured dots) recorded simultaneously along the Swarm tracks. In each map, which covers 00:00–24:00 MLT and $|50^\circ|$ – $|90^\circ|$ MLat, the magnetic noon/midnight is at the top/bottom.

Figure 35 shows the polar maps for the northern (top) and the southern (bottom) hemispheres in the time interval 19:00 to 23:00 UT (i.e. when the second significant scintillation peak occurs, see Figure

32). Scintillations mainly occurred in the southern hemisphere between the two convection cells. Several authors (see, e.g., De Franceschi et al 2008; Mitchell et al 2005; Moen et al. 2013) identified the region between the two convection cells as the best candidate to host the ionospheric irregularities causing scintillations. Scintillations occurred close to the region in which Swarm observed a clear increase in electron density (evidenced by an enhanced thickness of the Swarm track, Figure 35 bottom panels). Concerning the spectral width, in the northern hemisphere, the higher values are mainly concentrated in the cusp and in the early morning sector of the auroral oval. In the southern hemisphere, they are almost missing. The comparison between northern and southern maps in Figure 35 shows that the low/null number of spectral width observations above threshold (blue squares) were recorded in the southern hemisphere. This scenario could be associated with ionospheric absorption, reported as a Polar Cap Absorption from 22 to 24 June by the IPS Radio and Space Services bulletin, which blinded the HF radars. In fact, in the southern hemisphere the number of spectral width observations < 200 m/s is small (black squares). The overall convection symmetry was very similar with respect to the earlier interval considered above (Figure 34), with $B_{z,IMF}$ fluctuating around zero between 19:30 and 21:00 UT, with a strongly positive $B_{y,IMF}$ (see Figure 28, panels c, d). After about 21 UT, $B_{z,IMF}$ showed a more stable trend, with positive values: this is consistent with the shrinking of the polar cap, particularly evident in the northern hemisphere (Figure 35, panels p and r). The southern hemisphere seems to retain the usual symmetry of the convection patterns, even after 21 UT, but this could be an artefact of the convection model, being the actual SuperDARN measurements very sparse in the southern hemisphere during this interval.

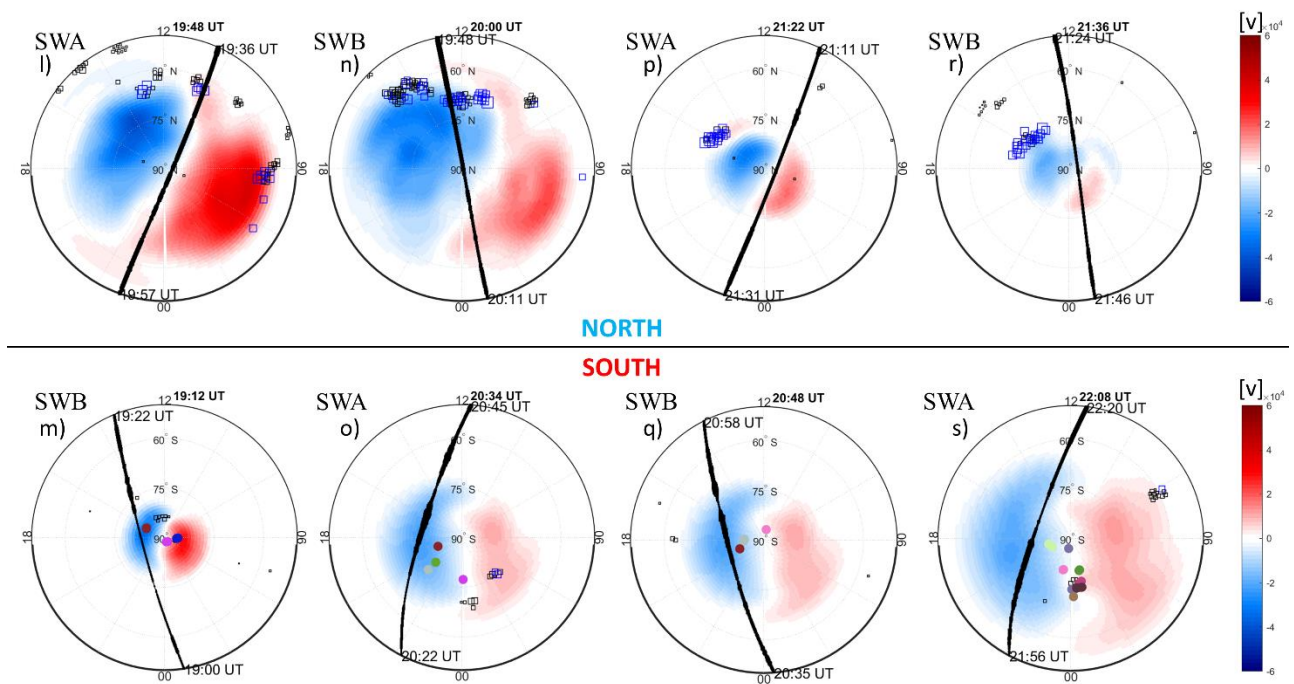


FIGURE 35: Polar-view maps in AACGM coordinates for the northern (top) and southern hemispheres (bottom) between 19:00-23:00 UT of 2015 June 22. Each map shows isocontours of the ionospheric potential (red=positive, blue=negative potential), recorded in the two minutes following the time shown at the top of each map; SuperDARN measurements of spectral widths less than 200 m/s (black squares) and larger than 200 m/s (blue squares); electron density (black line) recorded along the orbits of Swarm A (SWA) and B (SWB) satellites; phase scintillations greater than 0.25 radians (coloured dots) recorded simultaneously along the Swarm tracks. In each map, which covers 00:00-24:00 MLT and $|50^\circ|$ - $|90^\circ|$ MLat, the magnetic noon/midnight is at the top/bottom.

For this case study, as for that previously described (see section 4.1), the auroral radiance as measured by DMSP satellites in the time intervals between 07:00-10:00 UT and between 19:00-23:00 UT was compared with the phase scintillations both greater than 0.25 radians and less than 0.25 radians, recorded simultaneously along the DMSP tracks for June 22. The aim is to understand whether the particles precipitating in the auroral oval may have caused the observed scintillations. Since, as in the previous case study, the fields of view of the selected GNSS receivers did not cover the auroral region in both hemispheres (see Figure 25 and Figure 26) during the investigated time intervals, the polar-view maps displaying such comparison are not reported here.

Figure 36 shows the time profile of the *rms* of the ionospheric *in-situ* electron density measured by Swarm A (SWA, circles) and Swarm B (SWB, stars) during June 22, in both polar regions to 50° magnetic latitude. Dashed vertical lines mark the arrival at the magnetopause of the first (red) and second (green) interplanetary shock. Until ~18:30 UT, the *rms* in the southern hemisphere (red) is three times smaller than in the northern hemisphere (blue). At the same time, in the southern hemisphere the SWA *rms* (red circles) is roughly comparable with SWB *rms* (red stars). Conversely, in the northern hemisphere, *rms* appears greater (blue circles) for SWA than for SWB (blue stars). After the shock arrival at the Earth’s magnetopause (red and green dashed lines), the two satellites observed a higher electron density *rms* in both hemispheres. After the arrival of the second shock (green line), the *rms* in southern hemisphere (red) becomes greater than in the northern hemisphere (blue). In addition, the *rms* of SWA (blue circles) becomes comparable with those of SWB (blue stars), in the northern hemisphere.

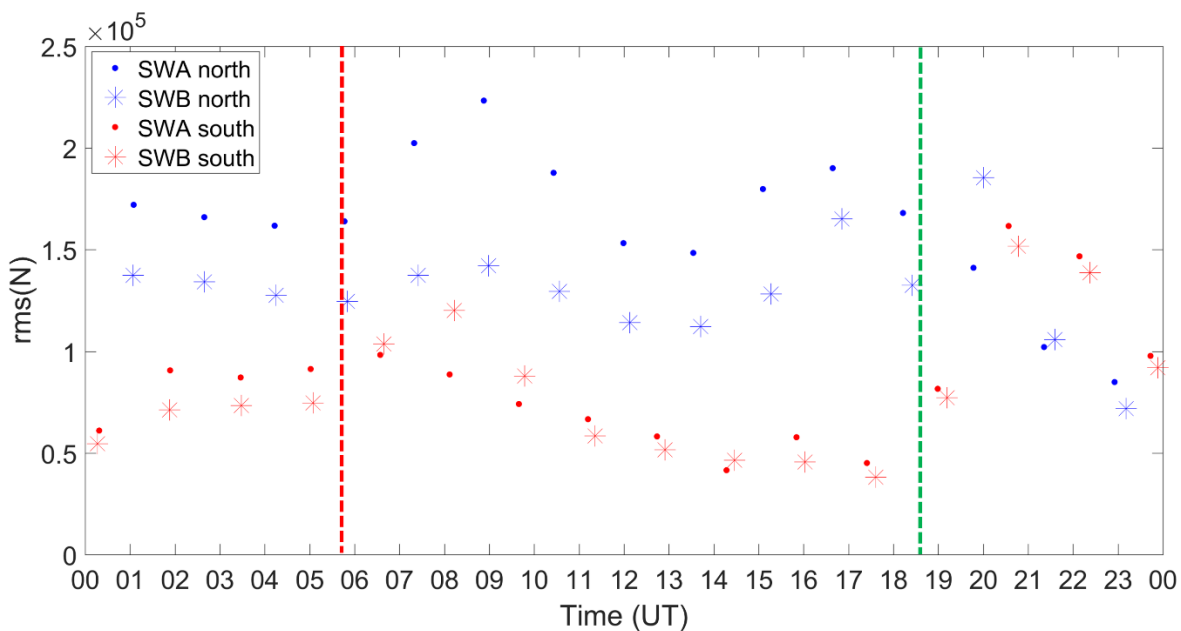


FIGURE 36: Electron density root mean square (*rms*) calculated starting from measurements acquired by Swarm A (circles) and Swarm B (stars) during 2015 June 22. Blue series refers to measurements in the northern hemisphere, while red series refers to measurements in the southern hemisphere. The Magnetic Latitude ranges between $[50^\circ]$ and $[90^\circ]$. The dashed vertical lines mark the arrival at the magnetopause of the first (red) and second (green) IPs.

4.3 THE 2017 SEPTEMBER STORM

The extreme solar activity at minimum of the solar cycle 24 occurred between 2017 September 4-10. The main source of the storm was the Active Region AR2673 (Catania sunspot group 46), which produced four X-class eruptions including the strongest of Solar Cycle 24 on 2017 September 6, with

a flare intensity of X9.3. A CME was observed to start on September 6, and triggered a class G4 storm (severe geomagnetic storm - NOAA Kp 8, $A_p = 106$) whose main phase was on 2017 September 7-8 (Tassev et al., 2017, Vanlommel and Van der Linden, 2017). In addition, between September 5 and 15:00 UT of September 8, increased values of the protons flux with energy > 10 MeV were recorded, resulting in several proton events (Vanlommel and Van der Linden, 2017).

The peculiarity of this storm is the capability to trigger small-scale irregularities resulting in amplitude scintillation events. The amplitude scintillation is biased by the irregularity probing size (on L band) of hundreds of meters (Aarons, 1997; Hunsucker and Hargreaves, 2002), related to the radius of the first Fresnel's zone. As shown in the case studies and as also known from the recent literature (see, e.g., Doherty et al., 2003; Jin et al., 2015; Prikryl et al., 2011, 2013; Spogli et al., 2009; Alfonsi et al., 2011), the formation of irregularities of such a scale is less probable, resulting in rare amplitude scintillation events at high-latitude. As a consequence, studies of signatures of amplitude scintillation in the polar regions are very few in the literature. Thus, this storm offers the opportunity to study such phenomenon that occurred during the main phase of the storm and recorded on sole receivers in the southern hemisphere. This is the reason why, despite the same methodological approach to the 2015 March and June storms has been adopted for the 2017 September storm, this latter event was analysed to focus the amplitude scintillations occurred over the southern hemisphere.

4.3.1 RESULTS

The period under investigation includes the geomagnetic storm triggered by enhanced solar activity that occurred between 4 and 10 September 2017. Specifically, the focus is on the main phase of this storm that began at the end of 2017 September 7, persisting until the end of 2017 September 8.

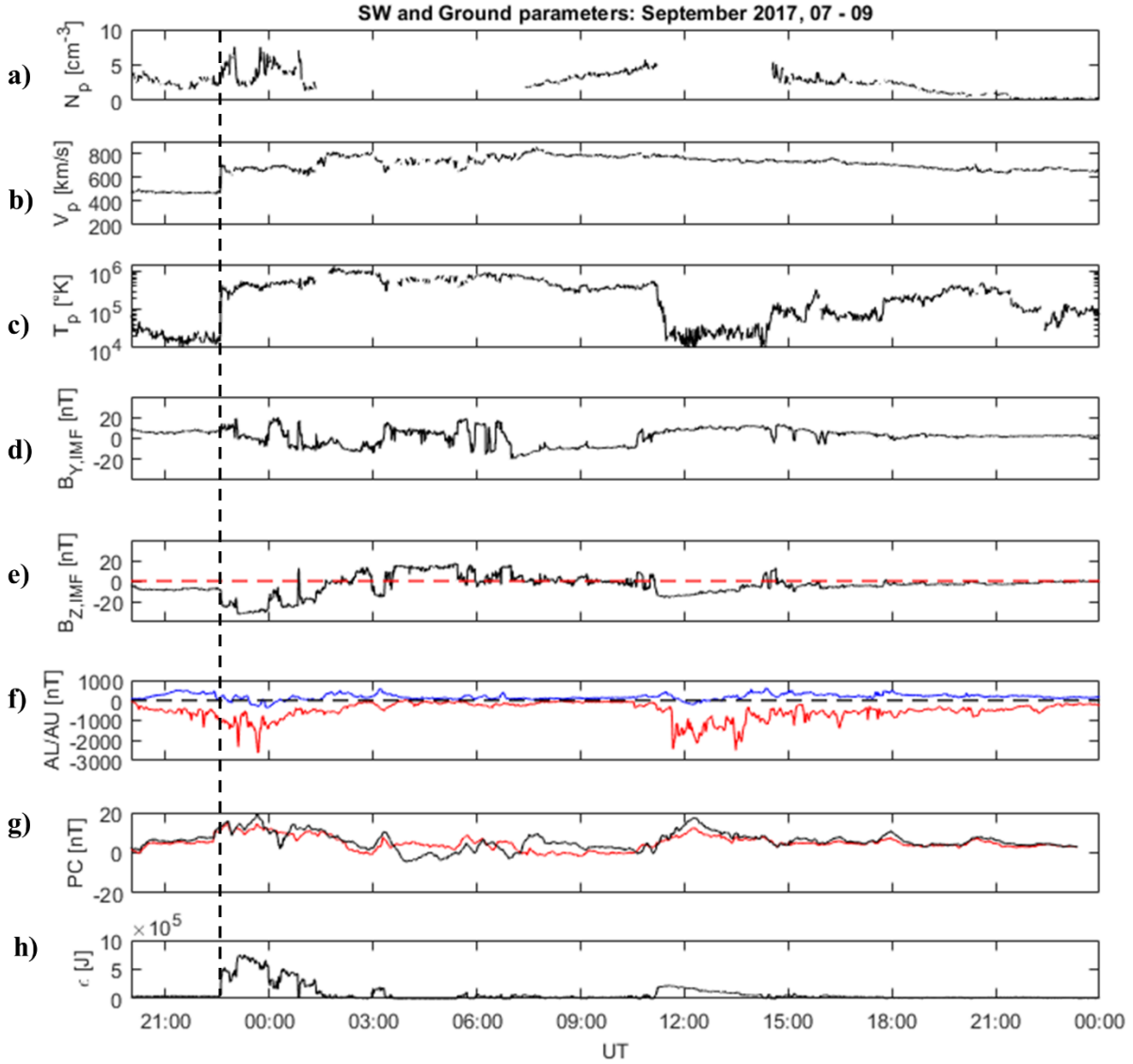


FIGURE 37: The solar wind (SW) observations (ACE spacecraft), the geomagnetic response at high latitudes and the Akasofu parameter from the end of 2017 September 7 until the end of 2017 September 8. From top to bottom: (a) SW density N_p ; (b) SW velocity V_p ; (c) SW proton temperature T_p ; (d) IMF $B_{y,IMF}$ component; (e) IMF $B_{z,IMF}$ component; (f) AU (blue line) and AL (red line) indices; (g) northern (red line) and southern (black line) Polar Cap indices; (h) Akasofu parameter. The black dashed vertical line marks the shock arrival at the earth's magnetosphere.

Figure 37 shows the variations of the main SW and IMF parameters measured by the ACE spacecraft and propagated to the Earth's magnetosphere, the auroral and polar activity indices and of the Akasofu parameter (Akasofu, 1979) recorded during the investigated time interval. The Akasofu parameter is defined as $\varepsilon = VB^2 l_0^2 \sin^4(\theta/2)$, where V is the plasma speed, B is the IMF intensity, θ is the IMF clock angle in the plane perpendicular to the Sun–Earth line and l_0 is the magnetopause standoff distance. Hence, the Akasofu parameter can be considered as a measure of the magnetospheric energy budget under solar wind forcing (Perreault and Akasofu, 1978; Akasofu, 1979, 1981). The black dashed vertical line marks the shock arrival at the Earth's magnetosphere identified by the clear jump in the SW density (N_p , panel a), SW proton temperature (T_p , panel c) and SW velocity (V_p , panel b). From Figure 37, the shock hit the magnetosphere at 22:29 UT on September 7. According to panel b, concurrent with the shock arrival, the SW velocity (V_p) jumped to over 620 km/s and increased further afterwards to speeds between 700–800 km/s. The IMF $B_{z,IMF}$

component (panel e) was strongly and persistently negative for the 3 hours following the shock, with a minimum at -33nT . Furthermore, from around 11:15 UT on September 8, a new period of pronounced negative $B_{z,\text{IMF}}$ (starting at -17nT) set in. During such negative excursions of the $B_{z,\text{IMF}}$ component, a marked increase in intensity of the Akasofu parameter was observed.

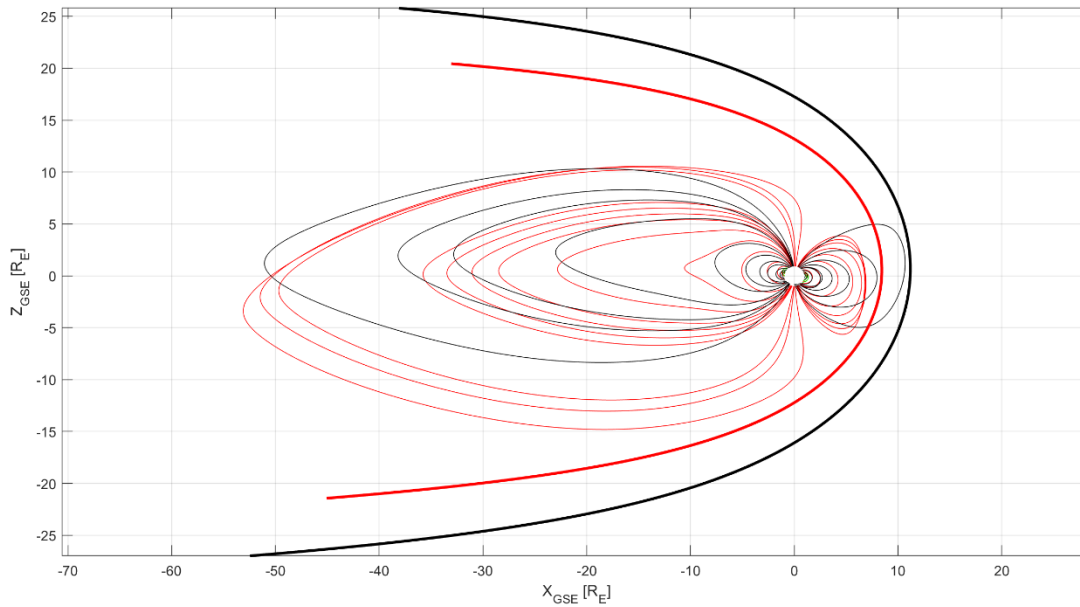


FIGURE 38: Magnetospheric field lines configuration before (black) and after (red) the IPs arrival. Black and red thick lines identify, respectively, the magnetopause before and after the IPs arrival on 2017 September 7.

In order to reconstruct the shape of the Earth's magnetosphere after the shock arrival, the direction of the IPs normal was estimated by applying the coplanarity theorem (see e.g. Kallenrode, 2013) to solar wind data. The resulting IPs parameters are $\theta=68.3^\circ$, $\phi=-178^\circ$, where θ and ϕ are the shock normal latitude and longitude in the Geocentric Solar Ecliptic (GSE) plane respectively. According to these parameters, the shock impacts the magnetopause mainly in the southern hemisphere. To confirm this hypothesis, the configuration of the magnetospheric field lines before and after the IPs impact on the magnetopause is evaluated by using the TS04 model. The results are shown in Figure 38 in which the configuration of the magnetospheric field lines before and after the shock are shown in black, and in red, respectively. From the figure, the IPs impact caused a compression of field lines on the dayside and stretching on the nightside, with a significant southward lowering of both tail lobes.

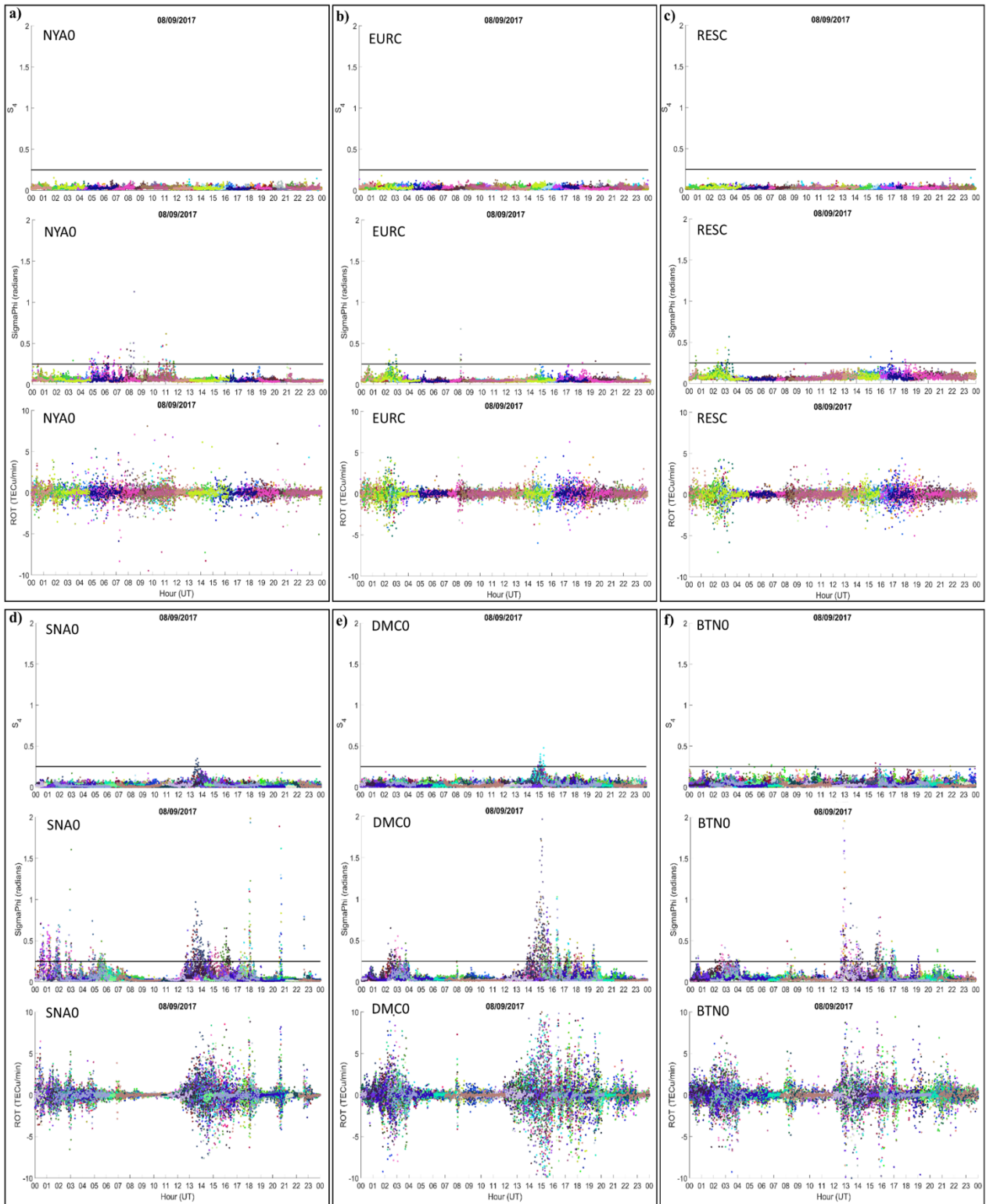


FIGURE 39: Time profiles of S_4 (top), σ_ϕ (middle) and ROT (bottom) recorded by NYA0 (a), EURC (b), RESC (c), SNA0 (d), DMC0 (e) and BTN0 (f) receivers on 2017 September 8. Different colours refer to different satellites in view. The black horizontal lines on σ_ϕ and S_4 variations indicate the 0.25 (radians) threshold, which defines the transition from weak (below the line) to moderate/strong (above the line) scintillation levels.

Figure 39 shows the time profiles of S_4 (top), σ_ϕ (middle) and ROT (bottom) recorded by NYA0 (a), EURC (b), RESC (c), SNA0 (d), DMC0 (e) and BTN0 (f) receivers on 2017 September 8. Different

colours refer to different satellites in view. Note that a different colour palette has been used to plot scintillation recorded in the southern hemisphere because scintillations were detected by special multi-constellation receivers for scintillation studies, able to provide access not only to GPS signals, but also to GLONASS and Galileo data (see section 2.2). Hence, additional colours are necessary to indicate GLONASS and Galileo satellites. The black horizontal lines on the σ_ϕ and S_4 variations characterize the 0.25 (radian) threshold, which defines the transition from weak (below the line) to moderate/strong (above the line) phase scintillation levels.

As from Figure 39, the σ_ϕ variations recorded by all stations (middle panels) show phase scintillation events coincided mainly with the strong auroral activity resulting from the negative excursions of $B_{z,IMF}$ (see panels e and f in Figure 37). The only exception is NYA0 (panel a) that shows scintillations starting from 05:00 UT until about 12:00 UT, in correspondence with the numerous oscillations of $B_{z,IMF}$ (panel e in Figure 37). The phase scintillations appear longer lasting and more intense in the southern hemisphere (d, e and f middle panels). By observing the ROT variations recorded by all stations (bottom panels), ROT excursions occurred mainly together with phase scintillation events in all the investigated ionospheric regions. In addition, southern receivers (d, e and f bottom panels) recorded the most intense and the longest lasting ROT excursions.

As already introduced at beginning of section 4.3, this investigation focuses on the amplitude scintillation, to study the formation of the small-scale irregularities. The S_4 variations recorded by all stations (top panels in Figure 39) show that only the southern receivers (SNA0, panel d; DMC0, panel e; BTN0, panel f) detected amplitude scintillations over the moderate/strong threshold for several satellites. Amplitude scintillation peaks occurred in concomitance with strong phase scintillations (middle d, e and f panels) and very intense ROT excursions (bottom d, e and f panels). This event occurred during the second negative excursions of the $B_{z,IMF}$ (panel e in Figure 37). The SNA0 receiver first recorded the amplitude scintillation event, with a maximum intensity of ~ 0.35 at $\sim 13:30$ UT. Then, the DMC0 and BTN0S receivers recorded amplitude scintillations with a maximum intensity of ~ 0.50 at $\sim 15:00$ UT and of ~ 0.28 at $\sim 15:40$ UT, respectively.

To trace back the observed amplitude scintillations to the physical mechanism triggering their occurrence, a geomagnetic characterization of the GNSS sites was performed. Specifically, the horizontal component (H) of the geomagnetic field (see section 1.4.3), recorded at the ground by magnetometers co-located with the southern GNSS receivers (SNA0, DMC0 and BTN0, respectively), was investigated in order to support the description of the ionospheric area entering in the field of view of such receivers.

Figure 40 shows the variations of the H component of the geomagnetic field recorded at the ground by magnetometers co-located with the SNA0 (top left panel), DMC0 (top middle panel) and BTN0 (top right panel) GNSS receivers, on 2017 September 8 and the corresponding S_4 variations (bottom panels) simultaneously recorded by such receivers.

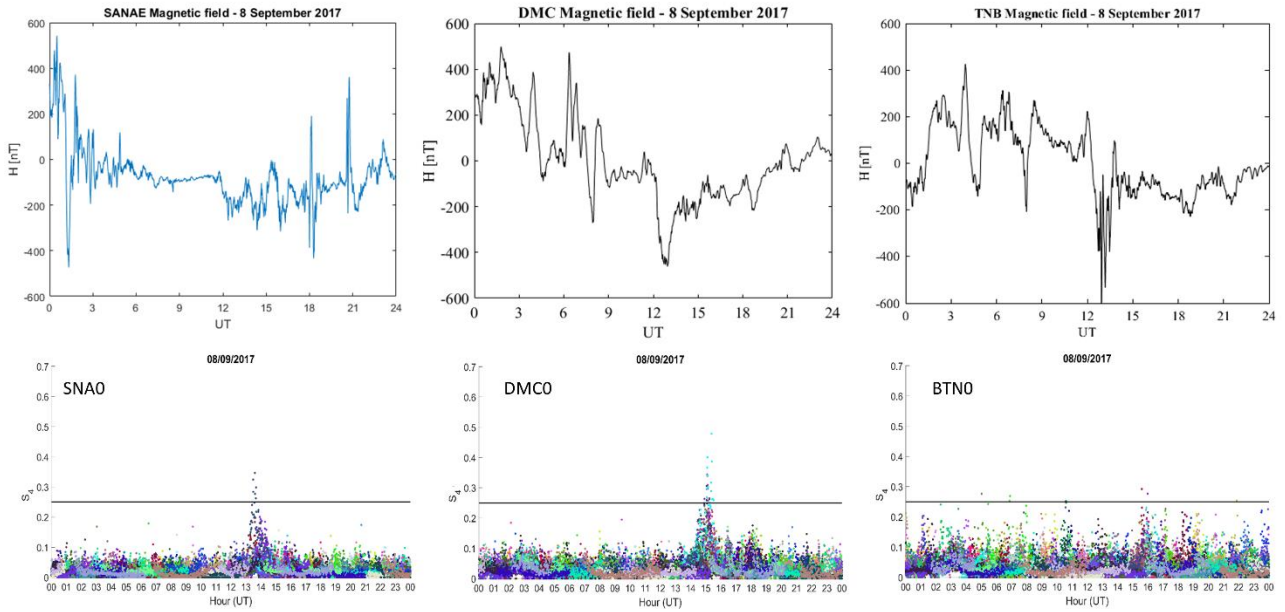


FIGURE 40: Variations of the H component of the geomagnetic field recorded at the ground by magnetometers co-located with the SNAO (top left panel), DMC0 (top middle panel) and BTNO (top right panel) GNSS receivers, on 2017 September 8. Bottom panels show the S_4 variations recorded by SNAO (bottom left panel), DMC0 (bottom middle panel) and BTNO (bottom right panel) GNSS receivers during the same day. The black horizontal lines on S_4 variations (bottom panels) characterize the 0.25 threshold, which defines the transition from weak (below the line) to moderate/strong (above the line) phase scintillation levels.

As visible in the top panels, between about 11:00-15:00 UT, DMC (middle) and TNB (right) observed the second main phase associated with the second negative excursion of $B_{z,IMF}$ (panel e in Figure 37). On the other hand, the SNAE magnetometer (left top panel) was unable to observe it. The data from this station between 07:00-12:00 UT, observed a steady state suggesting that this station became a cusp station (Piersanti and Villante 2016; Villante and Piersanti 2009).

To check this, the complete magnetopause model by Shue et al., (1998) was applied to the solar wind and IMF parameters (in particular to the solar wind dynamic pressure and to the $B_{z,IMF}$) at the shock arrival, giving a magnetopause standoff distance of $5.6 R_E$. Consequently, the coordinates of the last field line on the dayside are $\pm 63.5^\circ$ MLat and 272.4° MLon. This magnetospheric erosion placed the SNAE station, located at subauroral latitude during quiet times, in the cusp/auroral during 8 September 2017 (see Table 1). It is important to specify that the TS04 model gave a magnetopause stand-off distance of $7-8R_E$ (Figure 38), because it does not consider the contribution of $B_{z,IMF}$.

Polar-view maps showing *in-situ* and ground based measurements provide details of the ionospheric conditions above the GNSS sites during the occurrence of the amplitude scintillation events. As for the previous cases study (see section 4.1 and 4.2), spectral width larger than 200 m/s is selected as a threshold to distinguish between different plasma regimes in the ionosphere. In each map, which covers the interval 00:00-24:00 MLT and the $|50^\circ|-|90^\circ|$ MLat sector, the magnetic noon/midnight is at the top/bottom.

The maps in Figure 41 show that the overall convection pattern in the southern hemisphere is consistent with a scenario dominated by $B_{z,IMF}$ predominantly negative, with convection cells tilted towards dawn by the effect of a mainly positive $B_{y,IMF}$ (panels d and e in Figure 37). Amplitude scintillations occurred in regions well known to be characterised by irregularities causing scintillation, as the cusp (see bottom left panel) and the region between two convection cells (right bottom panel).

Such scintillations occurred close to the ionospheric regions in which Swarm satellites observed sudden electron density variations (left panel) and SuperDARN recorded large spectral widths values (blue squares in right panel).

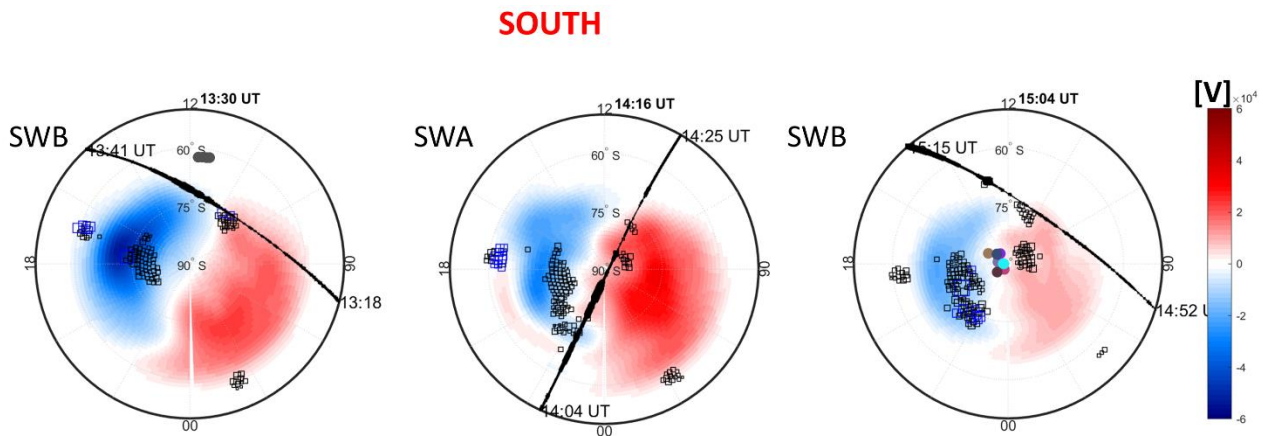


FIGURE 41: Polar-view maps in AACGM coordinates for the southern hemispheres (bottom) between 13:00-16:00 UT of 2017 September 8. Each map shows: isocontours of the ionospheric potential (red=positive, blue=negative potential), recorded in the two minutes following the time shown at the top of each map; SuperDARN measurements of spectral widths less than 200 m/s (black squares) and greater than 200 m/s (blue squares); electron density (black line) recorded along the orbits of Swarm A (SWA) and B (SWB) satellites; amplitude scintillations greater than 0.25 (coloured dots) recorded simultaneously along the Swarm tracks. In each map, which covers 00:00-24:00 MLT and $|50^\circ|$ - $|90^\circ|$ MLat, the magnetic noon/midnight is at the top/bottom.

Figure 42 shows the time profile of the *rms* of the ionospheric *in-situ* electron density measured by Swarm A (SWA, circles) and Swarm B (SWB, stars) during September 8, in both Polar regions within 50° of magnetic latitude.

Until $\sim 07:00$ UT and between 20:00-24:00 UT, *rms* values in the southern (red) and in the northern hemisphere (blue) are comparable. Between 07:00-13:00 UT, larger *rms* values occur in the northern hemisphere (blue) compared with the southern hemisphere (red). During this interval in both hemispheres Swarm A measured *rms* values (circles) larger than those measured by Swarm B (stars). Between 13:00-20:00 UT, the two satellites observed a larger electron density *rms* in both hemispheres even if, starting from 14:00 UT, *rms* values were larger in the southern hemisphere (red) than in the northern hemisphere (blue).

Figure 43 shows the ionogram series recorded between 13:00-16:00 UT on 2017 September 8 by the Jang Bogo VIPIR co-located with the BTN0 GNSS station. Both sporadic E-layer and spread-F (see section 1.3) are recorded by the VIPIR in correspondence with the amplitude scintillation events. It is worth noticing the presence of severe ionospheric absorption events, appearing as the lack of reflected echoes.

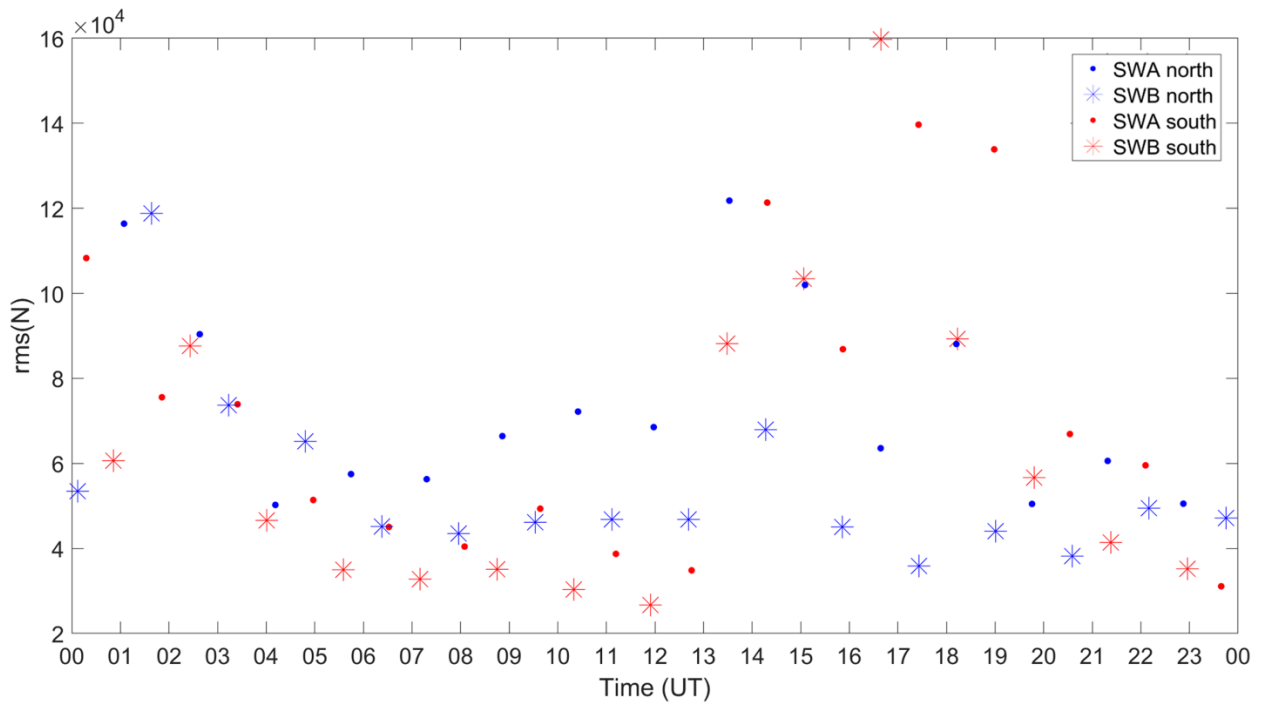


FIGURE 42: Electron density root mean square (rms) calculated from measurements acquired by Swarm A (circles) and Swarm B (stars) during 2017 September 8. Blue series refers to measurements in the northern hemisphere, while red series refers to measurements in the southern hemisphere. The magnetic latitude ranges between $|50^\circ|$ and $|90^\circ|$.

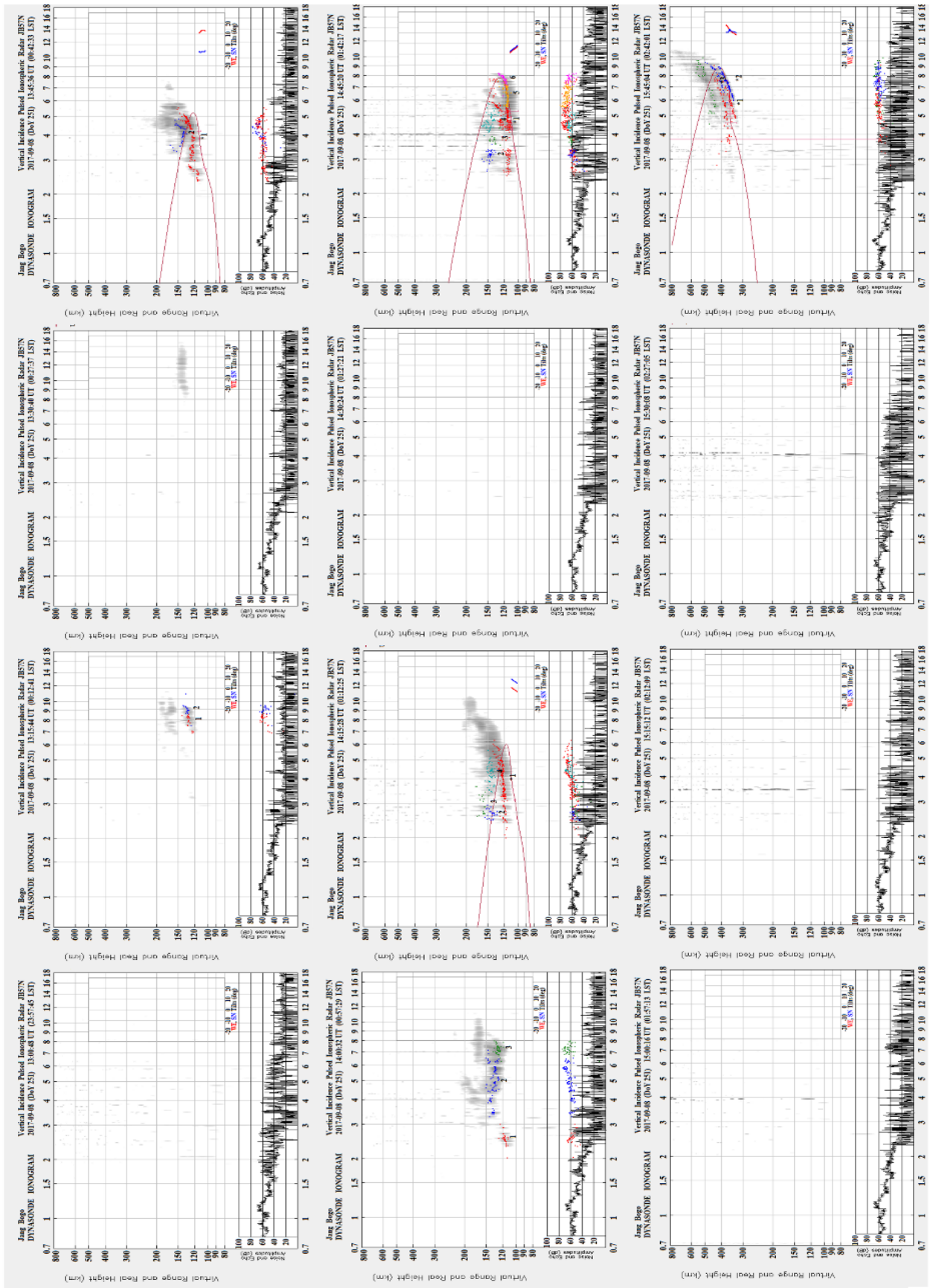


FIGURE 43: Ionogram series recorded by Jang Bogo Vertical Incidence Pulsed Ionospheric Radar (VIPIR) co-located with Mario Zucchelli (Terra Nova Bay) GNSS station between 13:00-16:00 UT on 2017 September 8.

INTRODUCTION

This chapter discusses the main findings achieved through the investigation of the three case studies and draws the conclusions of the work conducted throughout this thesis.

The discussions are provided for each case study and comparing the three events to understand what is new, what can be learnt and what is already reported in the literature. The discussions include also a critical analysis of the limitations of each data set that can affect the results and interpretations.

The conclusions highlight the goodness of the adopted method and the contribution to the progress of the scientific understanding beyond the state of the art. In such a frame, the scientific and the applicative value of this work is underlined in the space weather context. The results can contribute, indeed, to the development of new models able to predict and mitigate the space weather effects induced on GNSS systems at ground. Finally, some proposed solutions that could be adopted in future studies are suggested.

DISCUSSION

5.1 2015 MARCH STORM

During 2015 March 17, the selected GNSS receivers (EURC, RESC, NYA0, DMC0, BTN0 and ZSGN) show the occurrence of strong and long lasting phase scintillation events. They occur mainly in correspondence with the first and the second ICME time travel (shaded regions in Figure 21). The north-south component of the IMF ($B_{z,IMF}$) was consistently southward (Figure 17d), except between 09:00 and 11:00 UT. These conditions led to particle precipitation and to an enhancement of the substorm activity, as visible from the auroral indices variations, shown in Figure 17, panel 1. In particular, the large variation of the AL index (panel 1, red line) suggests that a large number of particles came into the ionosphere from the magnetospheric tail (Feldstein et al., 1996; Turner et al., 2000; Kallio et al., 2000; Lui, 2011). In such an environment, ionospheric irregularities formed and accelerated, inducing the observed phase fluctuations on the GNSS signals received at the ground. The ROT time profiles, recorded by the GNSS receivers, showed intense and highly variable ROT gradients (Figure 22), in correspondence with the observed scintillations (Figure 21). According to Wernik et al. (2004) and Alfonsi et al. (2011) this means that the investigated regions were populated by irregularities of largely varying scale-sizes, spanning the range of kilometres. As described in section 2.2.2, in fact, the relation between the ROT and Nyquist period, allows the retrieving of the irregularities scale length involved in scintillations, which, at high latitude (where plasma convection velocities span a range between 100 m/s and 1 km/s), varies from few to tens of kilometres. In L-band scintillations, these sizes identify large-scale irregularities respect to the small-scales associated to the first Fresnel radius (of the order of hundreds of meters) (Chapter 2). The presence of large scale-size irregularities on 2015 March 17, is confirmed by Cherniak et al. (2015), who reported their occurrence from middle to high latitudes over both hemispheres. In addition, the absence of amplitude scintillations suggests that the scale-size of the irregularities causing scintillations were far from the first Fresnel radius (Yeh and Liu, 1982; Kintner et al., 2007). The scenario in which the observed irregularities were formed, characterized by consistently southward $B_{z,IMF}$ (Figure 17d), suggests the

formation of patches (Weber et al., 1984, 1985, 1986). Figure 23 and Figure 24, indeed, show that scintillations mainly occurred at cusps and in ionospheric region between the two convection cells in both hemispheres. According to the climatology conducted by Spogli et al. (2009) and Moen et al. (2013), the scintillations occurring inside the polar cap may be attributed to the polar cap patches. These works also show that even under extremely disturbed conditions moderate/strong amplitude scintillations, which occur in the polar cap, are much less frequently observed than the phase scintillations. According to Moen et al. (2013), this indicates that, on average, the fragmentation of the tongue of ionization (TOI, see e.g. Sato, 1959; Foster, 1984 and 1989) around noon does not result in amplitude scintillations exceeding the threshold of $S_4 > 0.25$. The higher occurrence rate of phase scintillations into the polar cap with respect to the amplitude scintillations may be attributed also to the typical velocities of the anti-sunward drift of patches. Such velocities, which are about 300–1000 m/s (see section 1.4.5) well correlate the scintillation with refractive effects. As described in Chapter 2, indeed, when a radio frequency signal in the form of a plane wave enters a medium of either increased or decreased phase velocity, it remains a plane wave but the received phase changes (see e.g. Wernik et al., 2003; Kintner et al., 2007). The refractive nature of the observed phase scintillation is supported by SuperDARN spectral width observations. In Figure 23 and Figure 24, it is visible that scintillations appear together with highly variable spectral width values (recognizable in the variable size of both black and blue squares). The latter, implying the presence of different plasma regimes in the high latitude ionosphere (see e.g. Woodfield et al. 2002, Chisham and Freeman, 2004, Ponomarenko and Water 2006, Ponomarenko et al., 2007), may justify the refractive nature of the observed scintillation and thus the absence of amplitude scintillation, which is diffractive in nature and caused by irregularities near the First Fresnel zone (see chapter 2). Further experimental evidence that supports the hypothesis of the refractive nature of the observed scintillation derives from the comparison between the variations of scintillation parameters shown in Figure 21 and Figure 22 and electron density *rms* variation shown in Figure 27. The comparison between the scintillation (Figure 21) and electron density *rms* (Figure 27) shows that the observed scintillations occurred in correspondence with sharp and sudden variations of the *rms* measurements. Since *rms* is an estimation of the mean value of the electron density (calculated for each time series related to a polar crossing of each Swarm satellite over an area spanning $|50^\circ|$ magnetic latitude (see section 3.2)) sharp and sudden increases/decreases in *rms* values between two consecutive orbits suggest a high variability of plasma dynamics. This hypothesis is supported by the comparison between the ROT (Figure 22) and electron density *rms* (Figure 27) variations. Since sharp and sudden increases/decreases in *rms* occurred simultaneously with the greatest ROT excursions recorded during the day, it is possible to support the hypothesis that the observed scintillation is linked to changes in plasma dynamics and therefore is refractive in nature. In fact, according to equation (2.9) in section 2.2.2, ROT is defined as the first derivative of TEC. This means that it is possible to consider ROT as an indicator of the plasma speed. Therefore, its variations are associated to the variability of plasma dynamics. It is important to notice that, since most of the steep gradients of electron density were recorded in the same ionospheric regions affected by scintillation (see maps in Figure 23 and Figure 24), it is possible to suppose that the variations of plasma density highlighted by the *rms* increases/decreases (measured *in-situ*) coincide with variations in plasma dynamics observed in ROT variations (measured at ground). It is also interesting to note that by comparing the phase scintillation measurements (measured at ground) and the Swarm electron density measurements (measured *in-situ*) at different heights it is possible to determine the altitudes of the irregularities causing scintillations.

The intensity of the ionospheric response, as shown by the scintillations (Figure 21), appears closely related to different geomagnetic sectors included in the field of view of the GNSS receivers and characterized by a marked hemispheric asymmetry, especially in the polar caps. A more intense and longer lasting scintillation activity affected the Antarctic polar cap, as compared with the Arctic one. Such asymmetry might be related to the different amount of particles precipitating in the two hemispheres, as reported by Cherniak et al. (2015) and Cherniak and Zakharenkova (2016). In order to confirm the different amount of particles precipitating in the two hemispheres on March 17, the total atmospheric integral energy flux has been estimated by summing the electron and proton atmospheric energy fluxes, provided by POES and MetOp satellites integrated at 120 km from the Earth's surface (see section 3.2). The results (Figure 44) show a more intense particle precipitation in the southern hemisphere. In fact, only the MetOp2 satellite measured a higher particle precipitation flux in the northern hemisphere, while all the other satellites observed a larger amount of particles entering the southern hemisphere. It is worth noticing that a large amount of particle precipitation was also recorded at latitudes $>75^\circ$ MLat. This supports the hypothesis that the observed scintillation was also caused by particles precipitating in the polar caps following those magnetic field lines that, reconnecting on dayside, move towards the magnetotail crossing the polar caps. As the fields of view of the selected receivers were unable to cover the auroral region in both hemispheres, as showed in Figure 25 and in Figure 26, it is not possible to confirm whether the observed particles precipitating into the auroral oval caused scintillations. The choice to use the energy fluxes measured by POES and MetOp is justified by the work conducted by Laundal et al. (2017). The authors report that the characteristics of particle precipitation can be quite different at conjugate points from both statistical studies and studies of conjugate images. They also report that the differences are mainly related to seasonal variations, and to asymmetric solar wind forcing on the magnetosphere, when the IMF has a significant GSM y (and to a lesser degree x) component. However, in this case study neither seasonal variations nor asymmetric solar wind forcing on the magnetosphere due to $B_{y,IMF}$ are able to explain the observed asymmetries in particle precipitation. In fact, as the St. Patrick's Day storm of March 2015 occurred close to the spring equinox, any physical interpretation of the observed asymmetries based on pronounced seasonal (summer/winter) effects would be unlikely (see e.g., Emery et al. 2008). In addition, since the north-south component of the IMF ($B_{z,IMF}$) was consistently southward (Figure 17d) during the day it is possible to neglect contributions of the $B_{y,IMF}$ in generating the interhemispheric differences.

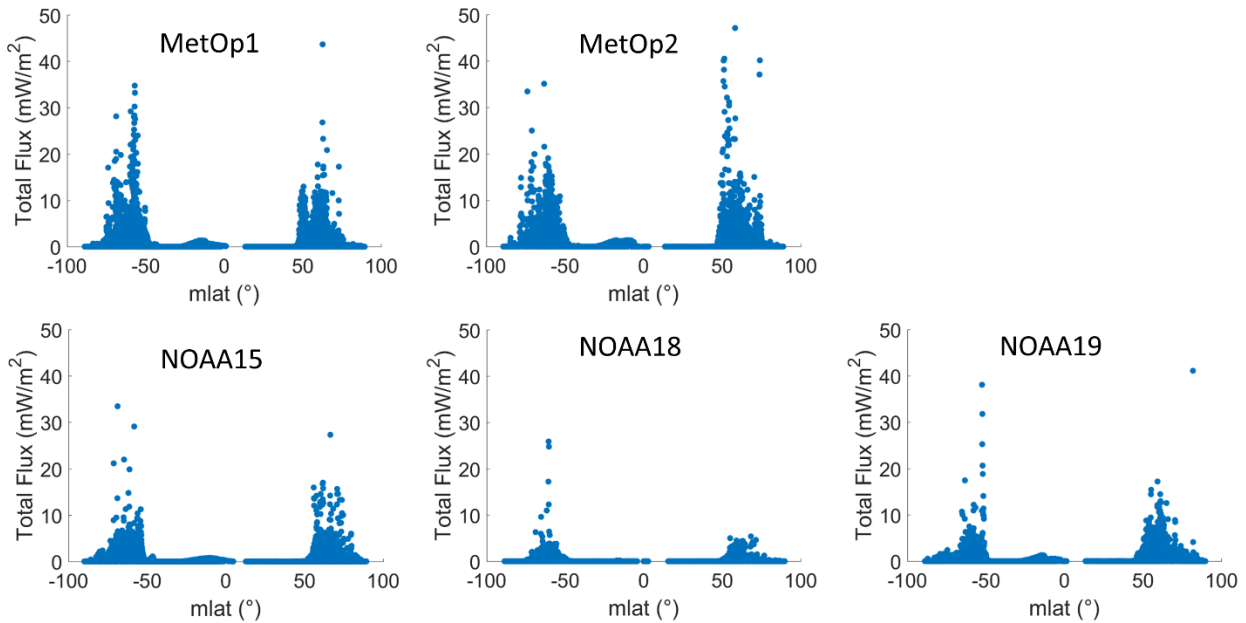


FIGURE 44: The total atmospheric integral energy flux at 120 km as a function of magnetic latitude as provided by POES and MetOp satellites on 2015 March 17.

A possible explanation for the observed hemispheric asymmetry in particle precipitation (Figure 44) can be ascribed to the peculiar reconfiguration of magnetospheric field lines caused by the impact of the interplanetary shock. In fact, as shown in Figure 18 and Figure 19, the IP geometry coupled with the particular configuration assumed by the night-side magnetosphere at the ICME arrival and the negative value of the dipole tilt angle ($\sim -6.19^\circ$) suggests the southern hemisphere to be more exposed to the solar perturbations. According to Villante and Piersanti (2014), IPs characterized by speed between ~ 430 and ~ 630 km/s propagate along the straight path. Since, the 2015 March 17 IP shock travelled at ~ 520 km/s, it is possible to correlate the greater exposure of the southern hemisphere with the shock impact point.

A further confirmation of the interhemispheric asymmetry due to the reconfiguration of magnetospheric field lines caused by the IPs impact geometry comes from the variation of the Polar Cap indices (PC) shown in Figure 17m. The PCS index (red line in panel m) shows a greater intensification of the magnetic activity in the southern hemisphere following the IPs arrival, which, according to the index definition (see section 1.4.4), means that the southern hemisphere was characterized by a larger perturbations than the northern hemisphere. Moreover, the polar-view maps of the current density of the FACs system (Figure 20) show, in correspondence with the IPs impact at the magnetopause and in the following ten minutes, an intensification of the cusp currents more pronounced in the southern hemisphere (see bottom maps at 04:50 UT and 05:00 UT), confirming definitely a southernmost impact of the IPs.

Another corroboration of the asymmetry in the response of both polar ionospheric regions to the storm comes from the *rms* variation of the electron density measured by the Swarm satellites (Figure 27). In fact, the measurements over the two hemispheres were comparable before the arrival of the solar perturbations and in conjunction with the positive switch of the z component of the IMF ($B_{z,IMF}$ Figure 17d). The differences between the two hemispheres occurred at the arrival of the solar perturbations, when the *rms* variation of the electron density showed a higher variability of the plasma density in

the south. It is possible to exclude a significant role of any seasonal effect in the observed asymmetry because the overall scenario derived by *in-situ* and ground-based records appear symmetric until the arrival of the solar perturbations.

The different exposure of the two hemispheres to the storm drivers may explain the response of the ionosphere in terms of hemispheric asymmetries in phase scintillations.

5.2 2015 JUNE STORM

Although the geomagnetic storm occurring during June 2015 was one of the most intense storms of the 24th solar cycle (Astafyeva et al., 2017; Piersanti et al., 2017), the observed scintillation was not as intense (Figure 32) as during the 2015 St. Patrick's day storm (D'Angelo et al., 2018). This unexpected behaviour might be due to two possible reasons. The first is the peculiar conditions of the north-south component of the IMF ($B_{z,IMF}$) recorded on 2015 June 22. In fact, $B_{z,IMF}$ first showed fluctuations around zero until the arrival of the second shock, and then a large brief negative excursion (see panel d in Figure 28). Such condition seems to be less effective in producing moderate/intense scintillation events than a negative, long lasting $B_{z,IMF}$ condition (D'Angelo et al., 2018). The second reason is the insufficient geomagnetic sector coverage of the GNSS receivers used in this analysis. In fact, according to Cherniak and Zakharenkova, (2017), a large number of plasma density fluctuations occurred in both auroral regions that are not in the field of view of the selected GNSS network. Nevertheless, our analysis retrieved the maximum available information considering the scarce coverage of GNSS receivers monitoring ionospheric scintillations at high latitudes.

In order to investigate how the observed scintillation is related to particle precipitation, the total atmospheric integral energy flux, calculated summing the electron and proton atmospheric energy fluxes, provided by POES and MetOp satellites integrated at 120 km from the Earth's surface, was studied (Figure 45). As seen in panel a, the particle precipitating flux in the time interval between the impact of the first and the second shock, was slightly more intense in the southern compared with the northern hemisphere. Correspondingly, DMC0 and ZSGN showed longer lasting phase scintillations (Figure 32), with respect to the northern receivers. Also in this case, neither seasonal variations nor asymmetric solar wind forcing on the magnetosphere due to $B_{y,IMF}$ are able to explain the observed asymmetries in particle precipitation. In fact, as this storm occurred during the summer solstice a more intense particle precipitating flux is expected to occur in northern hemisphere due to the combination of a more favourable geometry during summer for direct particle entry the ionosphere and stronger field-aligned currents during Bartels rotations in summer (see e.g. Green et al., 2009 and Coxon et al., 2016). In addition, since in the time interval between the impact of the first and the second shock $B_{y,IMF}$ showed fluctuations around zero (Figure 29c) it is possible to neglect contributions of the $B_{y,IMF}$ in generating interhemispheric differences. In this case, the different path of the particles that travel from the tail to the poles can explain the behaviour observed in Figure 45a. According to the shape assumed by the Earth's magnetosphere soon after the first shock (see red lines in Figure 29), it seems that such a path was shorter for the southern than for the northern hemisphere. Furthermore, the more intense particles precipitating flux recorded in the southern hemisphere is in agreement with an impact point located slightly lower than the ecliptic plane in the southern hemisphere (Table 2a). In fact, by assuming an IPs propagation along a straight path, according to Villante and Piersanti (2014), it is possible to correlate the greater exposure of the southern hemisphere with the shock impact point. Hence, the observed hemispheric asymmetry in particle precipitation shown in Figure 45a can be ascribed to the reconfiguration of magnetospheric field lines caused by the impact geometry of the interplanetary shock.

Figure 45b shows that at the arrival of the second shock the intensity of the particle precipitating fluxes is about the same in both hemispheres. At the same time, Figure 32 shows scintillations in all the investigated ionospheric regions of both hemispheres having almost the same intensity, with the exception of the northern polar cap. This behaviour is in agreement with the second shock parameters (Table 2b) that place the IPs impact point closest to the ecliptic plane. In fact, the IPs hit the Earth magnetopause with a speed of ~ 767 km/s (Table 2b) that support the hypothesis of a shock propagation along a straight path and with a negative $B_{z,IMF}$ value (Figure 28 d), which allows neglecting contributions of the $B_{y,IMF}$ in generating interhemispheric differences.

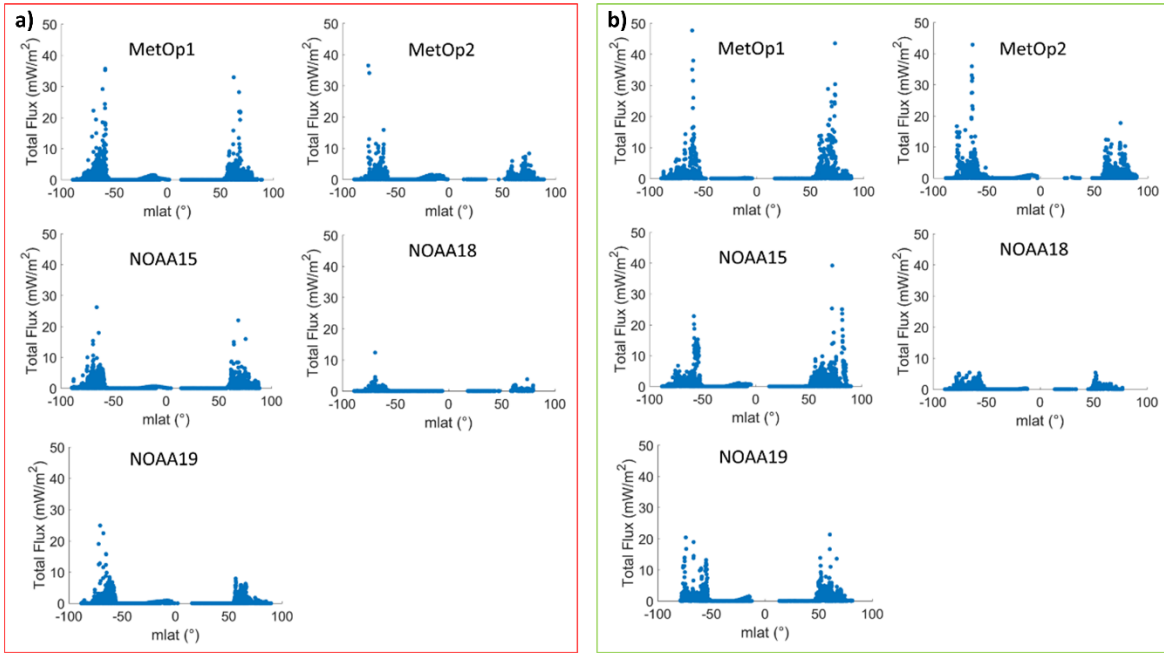


FIGURE 45: The total atmospheric integral energy flux at 120 km as a function of magnetic latitude as provided by POES and MetOp satellites for 2015 June 22. Panel a) shows fluxes measured in the time interval between the arrival of the first and second shock. Panel b) shows fluxes measured in the time interval from the arrival of the second shock and the end of the day.

According to the impact geometry of both shocks, the *rms* variations (Figure 36) show a similar behaviour in both hemispheres during June 22, despite the offset between northern and southern *rms*. Such an offset can be associated with seasonal effects. In fact, the different ionospheric background in terms of ionization resulted, in this case, in a larger *rms* in the summer (northern) hemisphere. The consequence of the different exposure of the two hemispheres to solar radiation, coupled with a southern impact of the first shock on the magnetopause (Table 2a) and with a more intense particle precipitation flux recorded in the southern hemisphere (Figure 45a), might be responsible of the larger *rms* of the SWA electron density in the northern hemisphere (blue circles in Figure 36). This suggests a highly variable dynamics at lower altitudes, possibly due to the dominance of ionospheric horizontal currents with respect to the vertical plasma circulation along the field lines. In addition, the impact of the second shock on the magnetopause slightly in the southern hemisphere (Table 2b), coupled with the large negative $B_{z,IMF}$ values (Figure 28 d), may have produced the enhancement of the southern *rms*, at this time comparable to the northern one.

Finally, following the analysis proposed by Alfonsi et al., (2011) and Wernik et al., (2004), the ROT time profiles (Figure 33) were compared with the σ_ϕ variations (Figure 32), recorded by all GNSS receivers. The absence of amplitude scintillation events suggests the presence of irregularities of

largely varying scale-size but with dimensions larger than the first Fresnel radius. This result suggests that the observed scintillation is refractive in nature. Such hypothesis agrees either with Cherniak and Zakharenkova, (2017), who showed the presence of a large number of plasma density fluctuations over both hemispheres during the day, and with Swarm electron density observations, which showed the presence of electron density enhancements in both polar regions (Figure 34, Figure 35). In addition, as the field of view of the selected GNSS receivers cover mainly the polar cap in both hemispheres, it is possible to suppose that the observed scintillation was due to patches (see e.g. Spogli et al., 2009 and Moen et al., 2013). The high speed that characterizes the motion of these irregularities (as described in the previous section 5.1) supports the hypothesis of the refractive nature of the observed scintillation.

Further experimental evidence that supports the hypothesis of the refractive nature of the observed scintillation derives from the comparison between the variations of scintillation parameters shown in Figure 32 and Figure 33 and the electron density *rms* variation shown in Figure 36. The comparison between the scintillation (Figure 32) and electron density *rms* (Figure 36) shows that the observed scintillations occurred in correspondence with sharp variations of the *rms* measurements suggesting the presence of plasma dynamics variability. This hypothesis is further supported by the comparison between the ROT (Figure 33) and electron density *rms* (Figure 36) variations. As described in the previous section (5.1), since sharp increases in *rms* occurred simultaneously with the greatest ROT excursions recorded during the day, it is possible to support the hypothesis that the observed scintillation is linked to changes in plasma dynamics and therefore is refractive in nature. It is important to notice that since most of the steep gradients of electron density were recorded in the same ionospheric regions affected by scintillation (see maps in Figure 34 and Figure 35) it is possible to suppose that the variations of plasma dynamics that caused the *rms* increases coincide with those observed in ROT excursions. It is also interesting to note that by comparing the phase scintillation measurements and the Swarm electron density measurements at different heights it is possible to determine the altitudes of the irregularities causing scintillations.

5.3 2017 SEPTEMBER STORM

The extreme solar activity at the minimum of solar cycle 24 triggered the occurrence of strong and long lasting phase scintillation events in the polar regions of both hemispheres on September 8 (Figure 39). Such scintillations mainly occur together with negative excursions of the $B_{z,IMF}$ (panel e in Figure 37), which caused the transmission of a large amount of energy by the solar wind to the magnetosphere/ionosphere system. In fact, during such excursions, notable enhancements of the Akasofu parameter occurred (panel h in Figure 37). All these conditions led to remarkable particle precipitation and to an enhancement in polar and auroral activity, as visible in panels f and g of Figure 37. The large variation of the AL index (red line) suggests that a large number of particles came into the ionosphere from the magnetospheric tail (Feldstein et al., 1996; Turner et al., 2000; Kallio et al., 2000; Lui, 2011). According to Cherniak and Zakharenkova (2015), this suggests the presence of favourable conditions to the formation of ionospheric plasma irregularities causing scintillation on the GNSS signals. The selected GNSS receivers (EURC, RESC, NYA0, DMC0, BTN0 and SNA0) detected several scintillation events on September 8, all characterized by a marked interhemispheric asymmetry. More intense and long lasting phase scintillation activity affected the Antarctic ionosphere as compared with the Arctic (middle panels in Figure 39). In addition, the GNSS receivers located in the southern hemisphere (DMC0, BTN0 and SNA0) detected significant amplitude

scintillation events (top d, e and f panels in Figure 39), that suggests small-scale irregularities were triggered by the storm.

Such interhemispheric asymmetry in the scintillation response might be related to the different amount of particles precipitating into the two hemispheres, as shown in Figure 46. This figure shows the total atmospheric integral energy flux at 120 km as a function of magnetic latitude as provided by POES and METOP satellites on 2017 September 8. During that day, more intense particle precipitation occurred in the southern hemisphere. In fact, all the satellites observed a larger amount of particles entering the southern hemisphere compared with the northern. The sole exception is the NOAA 15 satellite that measured a higher particle precipitation flux in the northern hemisphere. Also in this case, neither seasonal variations nor asymmetric solar wind forcing on the magnetosphere due to $B_{y,IMF}$ are able to explain the observed asymmetries in particle precipitation Laundal et al. (2017). In fact, as this storm occurred close to the fall equinox, any physical interpretation of the observed asymmetries based on pronounced seasonal (summer/winter) effects would be unlikely (see e.g., Emery et al. 2008). In addition, since scintillations mainly occur simultaneously with negative excursions of the $B_{z,IMF}$ (panel e in Figure 37), it is possible to neglect contributions of the $B_{y,IMF}$ in generating the interhemispheric differences. Here, the observed interhemispheric asymmetry in particle precipitation (Figure 46) can be supported by the reconstruction of the shape of the Earth's magnetosphere at the arrivals of the interplanetary perturbations. In fact, the TS04 model predictions (Figure 38) allow deducing that the IPs geometry, coupled with the particular configuration assumed by the night-side magnetosphere, caused the southern hemisphere to be more exposed to the impact of solar perturbations than the northern one. In fact, since the IPs hit the magnetopause with a speed of ~ 700 km/s it is possible to suppose an IPs propagation along a straight path (Villante and Piersanti 2014). This hypothesis is supported by the fact that, soon after the shock arrival and together with the second large negative excursion of $B_{z,IMF}$ (panel e in Figure 37), the southern PC index (black line in panel g of Figure 37) shows magnetic activity in the southern polar cap stronger than in the north. Such indices are comparable during the rest of the day. A further confirmation of the asymmetry in the response of both polar regions to the storm comes from the *rms* variation of the electron density measured by the Swarm satellites in both hemispheres (Figure 42). In fact, the measurements over the two hemispheres are comparable before the arrival of the second large negative excursion of $B_{z,IMF}$ (panel e in Figure 37). The differences between the two hemispheres begin at the arrival of the solar perturbations, when the *rms* variation of the electron density shows a larger variability of the plasma density in the south. Such behaviour agrees with the arrival of a solar wind plasma structure with high density, low temperature and negative values of $B_{z,IMF}$ (panels a, c, e in Figure 37). This results in a significant particle precipitation triggering both an exacerbation of the pre-existent interhemispheric asymmetries due to the shock geometry and a significant enhancement of the ionospheric electron density (Figure 42).

The different exposure of the two hemispheres to the storm drivers may explain the response of the ionosphere over Antarctica in terms of scintillations. In such an asymmetric scenario, it is possible to suppose that the presence of those conditions triggering amplitude scintillation occurred only in the southern hemisphere.

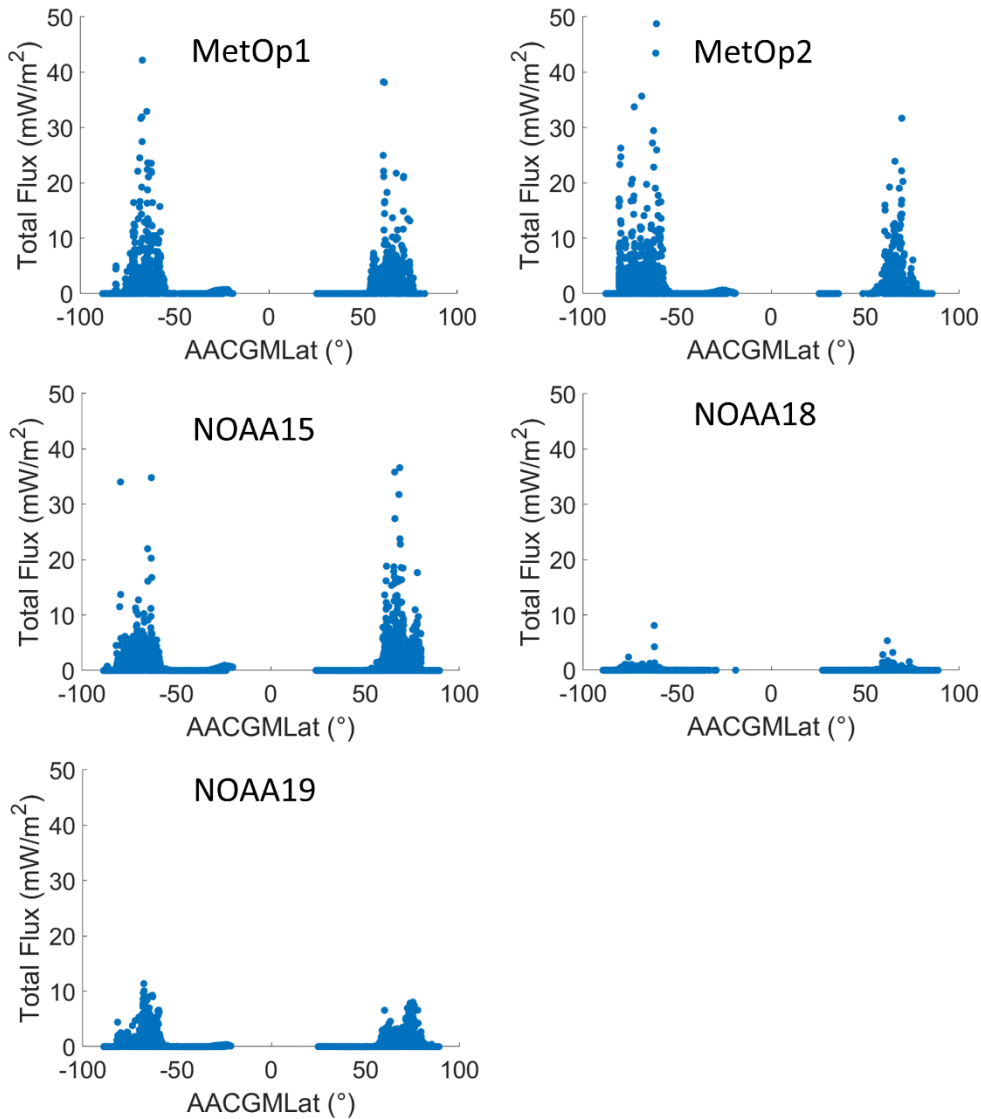


FIGURE 46: The total atmospheric integral energy flux at 120 km as a function of the magnetic latitude as provided by POES and MetOp satellites on 2017 September 8.

The occurrence of amplitude scintillations testifies a configuration of the magnetosphere-ionosphere system leading to the formation of ionospheric irregularities having scale size up to the first Fresnel's radius. As described in Chapter 2, this radius is about 365 m for the L1 signal encountering irregularities located in a single layer ionosphere at an altitude of 350 km. Even if rare, amplitude and phase fluctuations induced by the signal diffraction due to small-scale irregularities at high latitudes is of great interest, as they are stochastic in nature and cannot be corrected with standard techniques (see section 2.3). For this reason, it is fundamental to understand the physical mechanism triggering such events in order to define mitigation techniques.

The multi-observational reconstruction used to investigate this storm allows collocating the observed amplitude scintillations in an ionospheric scenario characterised by highly fragmented plasma in which irregularities of the order of the first Fresnel's radius can form. The top, middle and bottom d, e and f panels in Figure 39 show that amplitude scintillations occurred together with strong phase scintillations and intense ROT excursions. According to Wernik et al. (2004) and Alfonsi et al. (2011), it is possible to infer that the investigated regions were populated by irregularities of largely varying scale-sizes. From Figure 41 such events occurred close to ionospheric regions in which the Swarm

satellites observed sudden electron density variations (left panel) and SuperDARN recorded high spectral width values (blue squares in right panel). Such reconstruction suggest the presence of an irregular plasma density distribution, possibly caused by the particle precipitation event associated to the negative excursion of the $B_{z,IMF}$. This hypothesis is supported by the Swarm electron density *rms* variation. In fact, between 13:00-20:00 UT, the Swarm satellites observed an enhancement of the *rms* values in both hemispheres even if, starting from 14:00 UT, larger *rms* values occurred in the southern hemisphere (red) than in the northern hemisphere (blue). In addition, the ionogram series recorded by Jang Bogo VIPIR between 13:00-16:00 UT suggest the presence of irregularities at different heights (Figure 43). Such ionograms, indeed, show the presence of both sporadic-E layer and spread-F (see par. 1.3). They also show the occurrence of a severe ionospheric absorption, due to a 10 MeV proton event causing a PCA (see section 1.3.1) event between September 5 and 15:00 UT of September 8. The additional ionization triggered by such proton event coupled with the rapid variations of the Earth's magnetic field (Figure 40) is likely the cause of the plasma fragmentation, forming irregularities of scale sizes till the order of the first Fresnel's radius and even below.

5.4 COMPARATIVE ANALYSIS OF THE THREE STORMS

The main objective of this work was to understand how different configurations of the IMF-magnetosphere-ionosphere coupling are translated into different structuring and dynamics of the ionosphere. In this context, the objective of this work was the identification of those physical properties that if properly reproduced, can support forecasting, from few minutes to few hours before the event, of the disturbance effects induced by the polar ionosphere on GNSS systems. In detail, starting from the scintillations recorded by selected GNSS receivers at ground, this project investigated the origin of irregularities: by evaluating the ionospheric background under different interplanetary conditions; by studying the magnetosphere configuration during the main phase of intense geomagnetic storms; by reconstructing the ionospheric scenarios resulting in the observed scintillations. The work focused on the study of three among the major storms of the 24th solar cycle and in particular on their main phase that occurred on 2015 March 17th, 2015 June 22nd and 2017 September 08th, respectively. The choice of such case studies has been motivated not only by their intensity (that ensured a strong perturbation of the polar ionosphere), but also because they have been caused by different solar phenomena, occurring in different seasons. Hence, the selected events have been investigated to provide an in-depth characterization of the ionospheric irregularities under different helio-geophysical conditions.

The open issues addressed in this work have concerned:

1. Determination of the ionosphere's response time due to magnetosphere's perturbation events.
2. Quantification of the ionospheric disturbance intensity in comparison with the intensity of the solar disturbance.
3. Identification of the polar regions most exposed to the disturbance.
4. Identification and quantification of the ionospheric response in term of asymmetry level between the two hemispheres.
5. Study of the evolution of ionospheric irregularity dynamics in comparison with solar driver evolution.

The method followed a novel multi-instrumental and multi-parametric approach that combined information derived from ground-based measurements with those derived from space-based stations. Such approach allowed the reconstruction of the spatial-temporal environment in which the selected events occurred. This method has implied the integration of a broad spectrum of information necessary to characterize the ionospheric disturbances at different time scales (from milliseconds to days) and spatial scales (from millimetres to hundreds meters/kilometres), in accordance with the evolution of the storms drivers. The results achieved so far are related to effects observed within the field of views of the selected GNSS receivers. Nevertheless, as the paucity of scintillation monitors at high latitudes, they constitute an actual contribution to the advancement of knowledge in the field.

What learnt is here briefly summarized with respect to the points listed above.

1. Observations provided by satellites orbiting the first Lagrangian point (L1), by geostationary satellites, by GNSS constellation, by satellites flying in the magnetosphere and in the ionosphere and by ground-based devices were analysed and interpreted. This original multi-instrumental and multi-parametric approach inherits what suggested by recent studies, in which measurements acquired from different instruments have been analysed in order to determine the ionospheric response times during disturbed conditions (see e.g. De Franceschi et al., 2008; Burston et al., 2009; Astafyeva et al., 2015; Cherniak and Zakharenkova, 2016). The level of detail with which such approach was applied is completely new in the study of the ionospheric scintillations. In this work, the characterization of the ionospheric response times was evaluated in terms of scintillation on L-band signals. Therefore, the triggering times of scintillation and of electron density gradients associated with it were compared with ionospheric and magnetospheric currents triggering times.

The variations of scintillation parameters recorded during the 2015 St. Patrick's Day storm (Figure 21 and Figure 22) show that at the IPs arrival (black dashed vertical line) the only two stations that observed scintillations and moderate ROT excursions were the cusp/auroral stations (NYA0 and ZSGN). These variations are in agreement with the sudden increase in SYM-H index shown in panel i of Figure 17, which occurred at ~04:48 UT, the simultaneous sudden variations of AU and AL indices (panel m) and the intensification of the cusp currents recorded by the IRIDIUM satellites starting from 04:50 UT (Figure 20 middle panels). The southern polar cap GNSS stations DMC0 and BTN0 recorded weak scintillations and moderate/intense ROT excursions starting from 06:00 UT. These variations are in agreement with the intensification of the southern polar cap activity, which can be deduced from the increase of PCS polar cap index (red line in panel m of Figure 17). All other changes in scintillation parameters recorded during the day by all stations of the GNSS network (Figure 21 and Figure 22) seem to follow the evolution of changes in auroral and polar activity indices (panels l and m in Figure 17). In addition, the triggering times of electron density gradients resulted in the rms variations (Figure 27) seem to agree with the variation of polar cap indices shown in Figure 17m.

As for the 2015 March storm, the variations of scintillation parameters recorded during 2015 June 22 (Figure 32 and Figure 33) show that at the arrival of the first shock (red dashed vertical line) the only two stations that observed scintillations and moderate ROT excursions were the cusp/auroral stations NYA0 and ZSGN. These variations are in agreement with the sudden increase in SYM-H index shown in panel i of Figure 28, which occurred at ~05:49 UT and

intensification of the cusp currents recorded by the IRIDIUM satellites starting from 05:40 UT (Figure 30 middle panels). The triggering times of scintillations recorded by polar cap GNSS stations (EURC, RESC and DMC0) do not seem to show a direct correlation with the triggering times of the ionospheric and magnetospheric currents. Also in this case study, the triggering times of electron density gradients resulted in the rms variations (Figure 36) seem to agree with the variation of polar cap indices shown in Figure 28m. It was not possible to evaluate the triggering times of scintillation and of electron density gradients associated with the arrival of the second shock on June 22 because the ionospheric-magnetospheric dynamics triggered by the arrival of this shock overlaps the dynamics triggered by the arrival of the previous shock.

The set-up of a similar condition does not allow evaluating the triggering times of scintillation and of electron density gradients taking place on September 2017 event. In fact, the IPs causing the 2017 September storm hit the magnetopause on September 7th around 22:30 UT. However, the investigation of the ionospheric response in terms of scintillations on the L-band signals, described in section 5.3, is limited to September 8th. For this reason, it was impossible correlate the triggering times of scintillation and of electron density gradients with the arrival of the shock.

2. The comparative study of three cases makes possible to infer the role played by the orientation of the north-south IMF component (B_z, IMF) in producing irregularities causing scintillation. In particular the B_z, IMF southward condition seems to be the most favourable to trigger scintillations, even of great intensity. This condition can cause an increase in the electron density irregularities due to the increase in ionization associated with the particle precipitation. The latter, however, by determining the increase in ionospheric conductivity, can give rise to scintillations of a refractive nature caused by the consequent intensification of the plasma dynamics. In fact, scintillations recorded on March 2015 (Figure 21) and on September 2017 (Figure 39) were more intense and longer lasting than those recorded during the storm occurred on June 2015 (Figure 32). In June 22, B_z, IMF first showed fluctuations around zero until the arrival of the second shock, and then a large brief negative excursion (see panel d in Figure 28). According to D'Angelo et al. (2018) such condition seems to be less effective in producing moderate/intense scintillation events than a negative, long lasting B_z, IMF condition.

This result is obviously limited to the field of view of the selected GNSS receivers that cannot observe the auroral sector where the bulk of particle precipitation took place.

3. The comparison among the variations of the scintillation parameters measured at ground and of the electron density observations provided by Swarm satellites in-situ measurements allowed the identification of the polar cap as the region most exposed to the perturbations coming from the Sun, especially during B_z, IMF southward conditions. The investigation of the total atmospheric integral energy flux as provided by POES and METOP satellites allowed to support the hypothesis that the large exposition of polar cap regions is caused by particles precipitating in the polar caps following those magnetic field lines that, reconnecting on dayside, move towards the magnetotail crossing the polar caps.

In addition, the comparison between the variations of scintillation parameters and the horizontal component (H) of the geomagnetic field recorded at ground by magnetometers co-

located with the GNSS receivers, showed that during strong stormy conditions also the sub-auroral ionospheric region can be affected by strong scintillation events.

4. The multi-instrument investigation adopted in this work, covering both polar regions, allowed an improved understanding of the response of the two hemispheres to the same interplanetary perturbation. The comparison among the three cases showed that the ionospheric response to the storm in terms of symmetries/asymmetries in the observed scintillation is related to the different amount of particles precipitating into the two hemispheres. This is due to the reconfiguration of magnetospheric field lines caused by the impact geometry of the interplanetary shock. The recent literature relates the interhemispheric symmetries/asymmetries to seasonal variations and to asymmetric solar wind forcing on the magnetosphere when the IMF has a significant GSM y component (see Laundal et al., 2017 and references therein). However, the occurrence of the 2015 March and 2017 September storm close to the spring equinox suggest that any physical interpretation of the observed asymmetries based on pronounced seasonal (summer/winter) effects would be unlikely (see e.g., Emery et al. 2008). In fact, near the equinoxes it is possible to suppose the same ionospheric background in both hemispheres in terms of ionization. In addition, since in both the storms, the north-south component of the IMF (B_z, IMF) was consistently southward in correspondence with the observed scintillation, it is possible to neglect contributions of the B_y, IMF in generating the interhemispheric differences. Also in the case of 2015 June storm neither seasonal variations, nor asymmetric solar wind forcing on the magnetosphere due to B_y, IMF are able to explain the observed asymmetries in particle precipitation. In fact, as this storm occurred during the summer solstice a more intense particle precipitating flux is expected to occur in northern hemisphere due to the combination of a more favourable geometry during summer for direct particle entry the ionosphere and stronger field-aligned currents during Bartels rotations in summer (see e.g. Green et al., 2009 and Coxon et al., 2016). In addition, since in the time interval between the impact of the first and the second shock B_y, IMF showed fluctuations around zero (Figure 28c), it is possible to neglect contributions of the B_y, IMF in generating interhemispheric differences. The second shock carried negative values of B_z, IMF allowing neglecting contributions of the B_y, IMF in generating interhemispheric differences. The role played by the reconfiguration of the magnetospheric field lines in determining symmetries/asymmetries in the ionospheric response is supported both by the high velocities of shocks and by the multi-observational reconstruction of the ionospheric scenario in which irregularities causing scintillations formed and moved. The high velocities of shocks ensured their propagation along a straight path in magnetosphere (Villante and Piersanti 2014) while the reconstruction of the ionospheric scenario showed that the bulk of the intense and long lasting ionospheric perturbations occurred in the hemisphere most exposed to the interplanetary perturbation.
5. The multi-observational reconstruction of the ionospheric scenario caused by the interplanetary perturbations revealed the size of the irregularities causing scintillation and allowed speculating on the diffractive/refractive nature of the observed scintillation. The reconstruction of the ionospheric scenario of the 2015 March (section 5.1) and June (section 5.2) storms, in which only phase scintillations were observed, allowed to deduce the presence of electron density irregularities characterized by large dimensions (greater than hundreds of meters) and moving at high speeds (hundreds/thousands m/s). The presence of these

irregularities, together with the absence of amplitude scintillations indicated the observed scintillations as due to purely refractive effects.

The reconstruction of the ionospheric scenario characterized by the occurrence of both amplitude and phase scintillations allowed to speculate on the possible triggering mechanisms of diffractive scintillations at very high latitude. In the case of the September 2017 storm (section 5.3), these events result to have been triggered by the plasma fragmentation into scales till the first Fresnel's radius (or even below). The analysis suggested that the plasma fragmentation was caused by rapid changes in the geomagnetic field in a "super-ionized" ionosphere, in turn due to the effect of particle precipitation and of Polar Cap Absorption.

5.5 SUMMARY AND CONCLUSIONS

This work presents an interhemispheric, multi-instrument study of the response of the high latitude ionosphere during the main phases of three intense geomagnetic storms, occurred during the solar cycle 24. The ionospheric response has been evaluated in terms of scintillation on L-band signals. To investigate the origin and the evolution of the ionospheric irregularities causing scintillations, information from scintillation indices and ROT (derived from GNSS receivers) are combined with *in-situ* and ground-based measurements.

The results draw the following conclusions:

- Strong (or weak) solar perturbations do not necessarily correspond to strong (or weak) ionospheric perturbations. This confirms the non-linear relationship between geo-spatial disturbances and the response of the circumterrestrial environment.
- The reconfiguration of the magnetospheric field lines, following interplanetary shocks, identifies the main cause of the interhemispheric asymmetry in the ionospheric response in terms of scintillation on L-band signals.
- The scintillations recorded at high latitude result to be associated with strong polar and auroral geomagnetic activity.
- The multi-instrumental approach results a successful tool to characterize the high latitudes ionosphere dynamics both locally and globally, supporting the identification of the regions most affected by the scintillation on GNSS signals.
- The comparison between the *in-situ* (satellite) electron density measurements and the GNSS (ground-based) observations reveals a clear correlation between scintillations and electron density variations.
- The comparison between the *in-situ* (Swarm satellites) electron density measurements, the GNSS observations (at ground) and the solar wind parameters (at L1 Lagrangian point) enables to detect the arrival of the interplanetary perturbations in correlation with the plasma density variations and scintillations occurrence.
- Consistently with the $B_{z,IMF}$ southward condition, the scintillation results to be more intense in the polar cap of the hemisphere more exposed to the solar perturbation. This condition results also to be responsible for the formation of irregularities at all ionospheric heights.
- Consistently with the $B_{z,IMF}$ southward condition, the sub-auroral ionosphere results to exhibit perturbed behaviour due to the magnetospheric erosion.
- The comparison between ROT, phase scintillation parameters and Swarm observations allows to identify the presence of fast-moving electron density gradients, of several scale-sizes causing scintillation events.

- The comparison between the spectral width measurements and the phase scintillations provides insights about the link between the GNSS phase scintillation and different plasma regimes in the ionosphere. In particular, this comparison suggests that the ionospheric regions characterized by high spectral width are more likely to give rise to phase scintillation.
- The study of amplitude scintillation at high latitudes broadens the comprehension of the diffractive and refractive nature of the scintillation.
- The comparative analysis of the case studies confirms that different solar perturbations correspond to a different ionospheric response, in terms of scintillations.
- The comparative study of three different geomagnetic storms highlights the role played by the IMF in triggering the ionospheric scintillations. In particular, during $B_{z,IMF}$ southward condition, it is possible to observe irregularities enhancement due to both ionization increase and conductivity increase. The latter, indeed, leads to changes in ionospheric plasma dynamics favouring plasma aggregation/fragmentation. Differently, $B_{z,IMF}$ northward condition leads to a lower occurrence of scintillations.
- The comparative study of different geomagnetic storms suggests that irregularities having scale size up to the radius of the first Fresnel's zone form in a highly ionized ionosphere exposed to rapid variations of the geomagnetic field induced by interplanetary perturbation.

These results show how the combined use of data from *in-situ* and ground-based sensors permits a detailed characterization of ionospheric dynamics during a geomagnetic storm. Given that ionospheric scintillations are difficult to predict, the study of the ionosphere at different heights and with different sampling frequencies can provide information useful to better characterize the high latitude ionospheric scintillation, thus advancing the current understanding in the field. In the space weather context, this can pave the way to new approaches to develop predictive scintillation models.

This study has demonstrated, with an unprecedented detail, the power of a multi-instruments approach to describe the ionospheric conditions triggering scintillations on GNSS signals at high latitude. The results, even though achieved with a limited number of cases, clearly identify for the first time the direct link between the magnetospheric field configuration and the formation of irregularities causing scintillations at high latitudes of both hemispheres.

FUTURE STEPS

The analysis proposed during this thesis could be the input for further developments. The main actions to be undertaken in the future are identified as follows:

- Extend the analysis to additional case studies in order to better understand the role played by each magnetospheric current systems in modifying the field line geometry linked to the hemispheric asymmetry of scintillation events;
- Perform an investigation of the possible link between solar wind parameters and scintillation events at high latitudes in relationship to the magnetospheric field configuration assumed according to different solar wind conditions;
- Extend the analysis to middle and low latitudes in order to have a global view of the response of the ionosphere to the solar disturbances in terms of irregularities causing scintillation;
- Analyse the GNSS phase and amplitude raw data to deeper investigate the diffractive and refractive nature of the scintillation.

BIBLIOGRAPHY

- Aarons J., (1982). Global morphology of ionospheric scintillations. *Proceedings of the IEEE*, 70(4), 360-378.
- Aarons J., (1991). The role of the ring current in the generation or inhibition of equatorial F layer irregularities during magnetic storms. *Radio Science*, 26(4), 1131-1149.
- Aarons J., (1993). The longitudinal morphology of equatorial F-layer irregularities relevant to their occurrence. *Space Science Reviews*, 63(3-4), 209-243.
- Aarons, J., and Basu, S. (1994). Ionospheric amplitude and phase fluctuations at the GPS frequencies. In *ION GPS-94* (pp. 1569-1578).
- Aarons, J. (1997). Global positioning system phase fluctuations at auroral latitudes. *Journal of Geophysical Research: Space Physics*, 102(A8), 17219-17231.
- Achilli, T. (2015). Statistical Study Of The Earth's Magnetopause Boundary Layer Particle Populations.
- Akasofu, S. I., and Chapman, S. (1972). Solar-terrestrial physics. Oxford (International Series of Monographs on Physics) (Clarendon Press). *Quarterly Journal of the Royal Meteorological Society*, 99, 422, 793.
- Akasofu, S. I. (1979). Interplanetary energy flux associated with magnetospheric substorms. *Planetary and Space Science*, 27(4), 425-431.
- Akasofu, S. I. (1981). Energy coupling between the solar wind and the magnetosphere. *Space Sci. Rev.*, 28, 121.
- Alberti, T., Piersanti, M., Vecchio, A., De Michelis, P., Lepreti, F., Carbone, V., and Primavera, L. (2016), Identification of the different magnetic field contributions during a geomagnetic storm in magnetospheric and ground observations, *Ann. Geophys.*, DOI: 10.5194/angeo-34-1069-2016.
- Alfonsi, L., De Franceschi, G., & Perrone, L. (2001). Long term trend in the high latitude ionosphere. *Physics and Chemistry of the Earth, Part C: Solar, Terrestrial & Planetary Science*, 26(5), 303-307.
- Alfonsi, L., De Franceschi, G., Perrone, L., & Materassi, M. (2002). Long-term trends of the critical frequency of the F2 layer at northern and southern high latitude regions. *Physics and Chemistry of the Earth, Parts A/B/C*, 27(6-8), 607-612.
- Alfonsi L., C. N. Mitchell, G. De Franceschi, M. Lester, V. Romano, P. Spalla, P. Yin, (2005). A network for upper atmosphere monitoring at high latitudes of the northern hemisphere. *Memorie della Società Astronomica Italiana*, 76, 4.
- Alfonsi, L., Spogli, L., De Franceschi, G., Romano, V., Aquino, M., Dodson, A., & Mitchell, C. N. (2011). Bipolar climatology of GPS ionospheric scintillation at solar minimum. *Radio Science*, 46(3).

- Alfonsi, L., P. J. Cilliers, V. Romano, I. Hunstad, E. Correia, N. Linty, F. Dovis, O. Terzo, P. Ruiu, J. Ward, and P. Riley (2016), First observations of GNSS ionospheric scintillations from DemoGRAPE project, *Space Weather*, 14(10), pp.704-709 doi:10.1002/2016SW001488.
- Anderson, D. N., J. Buchau, and R. A. Heelis (1988). Origin of density enhancements in the winter polar cap ionosphere. *Radio Science* 23 (4), 513–519.
- Anderson, B. J., Takahashi, K., & Toth, B. A. (2000). Sensing global Birkeland currents with Iridium® engineering magnetometer data. *Geophysical Research Letters*, 27(24), 4045-4048.
- Apatenkov, S. V., V. A. Sergeev, M. V. Kubyshkina, R. Nakamura, W. Baumjohann, A. Runov, I. Alexeev, A. Fazakerley, H. Frey, S. Muhlbacher, P. W. Daly, J.-A. Sauvaud, N. Ganushkina, T. Pulkkinen, G. D. Reeves, and Y. Khotyaintsev (2007), Multi-spacecraft observation of plasma dipolarization/injection in the inner magnetosphere, *Annales Geophysicae*, 25, 801–814, doi:10.5194/angeo-25-801-2007.
- Astafyeva, E., Zakharenkova, I., and Förster, M. (2015). Ionospheric response to the 2015 St. Patrick's Day storm: A global multi-instrumental overview. *Journal of Geophysical Research: Space Physics*, 120(10), 9023-9037.
- Astafyeva, E., Zakharenkova, I., and Alken, P. (2016). Prompt penetration electric fields and the extreme topside ionospheric response to the June 22–23, 2015 geomagnetic storm as seen by the Swarm constellation. *Earth, Planets and Space*, 68(1), 152.
- Astafyeva, E., Zakharenkova, I., Huba, J. D., Doornbos, E., and IJssel, J. (2017). Global Ionospheric and Thermospheric Effects of the June 2015 Geomagnetic Disturbances: Multi-Instrumental Observations and Modeling. *Journal of Geophysical Research: Space Physics*, 122(11).
- Axford, W. I. and C. O. Hines (1961). A unifying theory of high-latitude geophysical phenomena and geomagnetic storms. *Canadian Journal of Physics* 39 (10), 1433–1464.
- Baker, D. N. (1998). What is space weather?. *Advances in Space Research*, 22(1), 7-16.
- Baker, K. B., and Wing, S. (1989). A new magnetic coordinate system for conjugate studies at high latitudes. *J. Geophys. Res.*, 94, 9139–9143, 1989.
- Basu, S., Basu, S., Mullen, J. P., & Bushby, A. (1980). Long-term 1.5 GHz amplitude scintillation measurements at the magnetic equator. *Geophysical Research Letters*, 7(4), 259-262.
- Basu S., and S. Basu, (1985). Equatorial scintillations: Advances since ISEA-6. *Journal of atmospheric and terrestrial physics*, 47(8), 753-768.
- Basu S., E. MacKenzie and S. Basu, (1988). Ionospheric constraints on VHF/UHF communications links during solar maximum and minimum periods. *Radio Science*, 23(3), 363-378.
- Basu S., S. Basu, E. J. Weber and G. J. Bishop, (1990). Plasma structuring in the polar cap. *Journal of geomagnetism and geoelectricity*, 42(6), 763-776.
- Basu Sa. and Su. Basu (1993), Ionospheric structures and scintillation spectra, in *Wave Propagation in Random Media (Scintillation)*, eds. V. I. Tatarski, A. Ishimaru, and V. U. Zavorotny, pp. 139-153, The International Society for Optical Engineering, Bellingham, WA, USA.

- Basu, S., K. M. Groves, J. M. Quinn, and P. Doherty (1999), A comparison of TEC fluctuations and scintillations at Ascension Island, *Journal of Atmospheric and Solar-Terrestrial Physics*, 61(16), 1219-1226, doi:10.1016/S1364-6826(99)00052-8.
- Bhattacharyya, A., K. C. Yeh, and S. J. Franke (1992). Deducing turbulence parameters from trans-ionospheric scintillation measurements, *Space Sci. Rev.*, 61, 335-386.
- Baumjohann, W. (1982). Ionospheric and field-aligned current systems in the auroral zone: A concise review. *Advances in Space Research*, 2(10), 55-62.
- Baumjohann W., R. A. Treumann, (1996). *Basic space plasma physics*. Imperial College Press, Cambridge, Singapore.
- Beach, T. L. (2006). Perils of the GPS phase scintillation index (σ_ϕ). *Radio science*, 41(5).
- Beniguel, Y., Orus-Perez, R., Prieto-Cerdeira, R., Schlueter, S., Scortan, S., & Grosu, A. (2015). MONITOR 2: ionospheric monitoring network in support to SBAS and other GNSS and scientific purposes. In *IES Conference*, Alexandria (Va) (pp. 05-22).
- Birkeland, K. (1908). *The Norwegian aurora polaris expedition 1902-1903* (Vol. 1). H. Aschelhoug & Company.
- Board, S. S. (2008). Committee on the Societal and Economic Impacts of Severe Space Weather Events: A Workshop.
- Booker, H. G., Ratcliffe, J. A., & Shinn, D. H. (1950). Diffraction from an irregular screen with applications to ionospheric problems. *Phil. Trans. R. Soc. Lond. A*, 242(856), 579-607.
- Bougard, B., Sleewaegen, J. M., Spogli, L., Veetil, S. V., & Monico, J. F. (2011, December). CIGALA: Challenging the solar maximum in Brazil with PolaRxS. In 24th International Technical Meeting of the Satellite Division of the Institute of Navigation 2011, *ION GNSS 2011* (pp. 2572-2579).
- Bremer, J. Ü. R. G. E. N., Alfonsi, L., Bencze, P., Lastovicka, J., Mikhailov, A. V., & Rogers, N. E. I. L. (2004). Long-term trends in the ionosphere and upper atmosphere parameters. *Annals of Geophysics*, 47(2-3 Sup.).
- Bramley, E. N. (1977). The accuracy of computing ionospheric radio-wave scintillation by the thin-phase-screen approximation. *Journal of Atmospheric and Terrestrial Physics*, 39(3), 367-373.
- Brekke A., (2012). *Physics of the upper polar atmosphere*. Springer Science & Business Media, Heidelberg, New York, Dordrecht, London.
- Bullett, T., Jee, G., Livingston, R., Kim, J. H., Zaboltn, N., Lee, C. S., ... & Kwon, H. J. (2016). Jang Bogo Antarctic Ionosonde. In *EGU General Assembly Conference Abstracts*(Vol. 18, p. 10776).
- Burston R., I. Astin, C.N. Mitchell, L. Alfonsi, T. Pedersen, S. Skone, (2009). Turbulent Times in the Northern Polar Ionosphere?, *J. Geophysical Research*, doi:10.1029/2009JA014813.
- Carlson, H. C. (2012). Sharpening our thinking about polar cap ionospheric patch morphology, research, and mitigation techniques. *Radio Science* 47, RS0L21.
- Carrano, C. S., Groves, K. M., & Caton, R. G. (2012). The effect of phase scintillations on the accuracy of phase screen simulation using deterministic screens derived from GPS and ALTAIR measurements. *Radio Science*, 47(04), 1-16.

- Cesaroni, C., Spogli, L., Alfonsi, L., De Franceschi, G., Ciraolo, L., Monico, J. F. G., ... & Bougard, B. (2015). L-band scintillations and calibrated total electron content gradients over Brazil during the last solar maximum. *Journal of Space Weather and Space Climate*, 5, A36.
- Chaggara R., Papparini C., Ngayap-Youmbi U., Duparc B. (2017). In depth characterization of EGNOS ground stations response to space weather disturbances. *International Technical Symposium on Navigation and Timing (ITSNT)*, ENAC, Toulouse, France.
- Cherniak, I., and I. Zakharenkova (2015), Dependence of the high-latitude plasma irregularities on the auroral activity indices: a case study of 17 March 2015 geomagnetic storm. *Earth, Planets and Space*, 67(1), 151.
- Cherniak, I., I. Zakharenkova, and R. J. Redmon (2015), Dynamics of the high-latitude ionospheric irregularities during the 17 March 2015 St. Patrick's Day storm: Ground-based GPS measurements. *Space Weather*, 13(9), 585-597, doi: 10.1002/2015SW001237.
- Cherniak, I., and Zakharenkova, I. (2016). High-latitude ionospheric irregularities: differences between ground-and space-based GPS measurements during the 2015 St. Patrick's Day storm. *Earth, Planets and Space*, 68(1), 136.
- Cherniak, I., and Zakharenkova, I. (2017). New advantages of the combined GPS and GLONASS observations for high-latitude ionospheric irregularities monitoring: case study of June 2015 geomagnetic storm. *Earth, Planets and Space*, 69(1), 66.
- Chisham, G., and Freeman, M. P. (2004). An investigation of latitudinal transition in the SuperDARN Doppler spectral width parameter at different magnetic local times. *Annales Geophysicae*, 22, 1187 – 1202.
- Chisham, G., M. P. Freeman, I. J. Coleman, M. Pinnock, M. R. Hairston, M. Lester, and G. Sofko (2004). Measuring the Dayside Reconnection Rate During an Interval of Due Northward Interplanetary Magnetic Field. *Annales Geophysicae* 22 (12), 4243–4258.
- Ciraolo, L., Azpilicueta, F., Brunini, C., Meza, A., & Radicella, S. M. (2007). Calibration errors on experimental slant total electron content (TEC) determined with GPS. *Journal of Geodesy*, 81(2), 111-120.
- Conker, R. S., El-Arini, M. B., Hegarty, C. J., & Hsiao, T. (2003). Modeling the effects of ionospheric scintillation on GPS/Satellite-Based Augmentation System availability. *Radio Science*, 38(1), 1-1.
- Cousins, E. D. P., and Shepherd, S. G. (2010). A dynamical model of high latitude convection derived from SuperDARN plasma drift measurements. *J. Geophys. Res., Space* 115. doi: 10.1029/2010JA016017.
- Coxon, J. C., S. E. Milan, J. A. Carter, L. B. N. Clausen, B. J. Anderson, and H. Korth (2016), Seasonal and diurnal variations in AMPERE observations of the Birkeland currents compared to modeled results, *J. Geophys. Res. Space Physics*, 121, 4027–4040, doi:10.1002/2015JA022050.
- Crooker, N. U. (1992). Reverse Convection. *Journal of Geophysical Research-Space Physics* 97 (A12), 19363–19372.
- Crowley, G. (1996). Critical review of ionospheric patches and blobs. *Review of Radio Science 1993–1996*, 619-648.

- D'Angelo, G., Spogli, L., Cesaroni, C., Sgrigna, V., Alfonsi, L., & Aquino, M. H. O. (2015). GNSS data filtering optimization for ionospheric observation. *Advances in Space Research*, 56(11), 2552-2562.
- D'Angelo, G., Piersanti, M., Alfonsi, L., Spogli, L., Clausen, L.B.N, Coco, I., Li, G., Baiqi, N. (2018). The response of high latitude ionosphere to the 2015 St. Patrick's Day storm from in situ and ground based observations. *Advances in Space Research*, 62(3), 638-650.
- D'Angelo, G., Piersanti, M., Alfonsi, L., Spogli, L., Coco, I., Li, G., & Baiqi, N. (2018). The response of high latitude ionosphere to the 2015 June 22 storm. *Annals of Geophysics*, 61, 44.
- Davis, T. N., & Sugiura, M. (1966). Auroral electrojet activity index AE and its universal time variations. *Journal of Geophysical Research*, 71(3), 785-801.
- De Franceschi, G., Alfonsi, L., & Romano, V. (2006). ISACCO: an Italian project to monitor the high latitudes ionosphere by means of GPS receivers. *GPS Solutions*, 10(4), 263-267.
- De Franceschi G., L. Alfonsi, V. Romano, M. Aquino, A. Dodson, C. N. Mitchell, P. Spencer, and A. W. Wernik, (2008). Dynamics of high-latitude patches and associated small-scale irregularities during the October and November 2003 storms. *Journal of Atmospheric and Solar-Terrestrial Physics*, 70(6), 879-888.
- Dehel, T., Lorge, F., Warburton, J., & Nelthropp, D. (2001). Satellite Navigation vs. the Ionosphere: Where Are We, and Where Are We Going?. In *Proceedings of the 17th International Technical Meeting of the Satellite Division of The Institute of Navigation (ION GNSS 2004)* (pp. 375-386).
- Didebulidze, G. G., Dalakishvili, G., Lomidze, L., & Matiashvili, G. (2015). Formation of sporadic-E (Es) layers under the influence of AGWs evolving in a horizontal shear flow. *Journal of Atmospheric and Solar-Terrestrial Physics*, 136, 163-173.
- Doherty, P. H., Delay, S. H., Valladares, C. E., & Klobuchar, J. A. (2003). Ionospheric scintillation effects on GPS in the equatorial and auroral regions. *Navigation*, 50(4), 235-245.
- Doxas, I., W.Horton, W. Lin, S. Seibert and M. Mithaiwala (2004), A dynamical model for the coupled inner magnetosphere and tail. *IEEE transactions on plasma science*, 32(4), 1443-1448, doi: [10.1109/TPS.2004.833388](https://doi.org/10.1109/TPS.2004.833388).
- Dungey, J. W. (1961). Interplanetary Magnetic Field and the Auroral Zones. *Phys. Rev. Lett.* 6, 47-48.
- Dyson, P. L., J. P. McClure, and W. B. Hanson (1974). In Situ Measurements of the Spectral Characteristics of F Region Ionospheric Irregularities. *Journal of Geophysical Research* 79 (10), 1497-1502.
- Eastman, T. E., Hones, E. W., Bame, S. J., & Asbridge, J. R. (1976). The magnetospheric boundary layer: Site of plasma, momentum and energy transfer from the magnetosheath into the magnetosphere. *Geophysical research letters*, 3(11), 685-688.
- Emery, B. A., V. Coumans, D. S. Evans, G. A. Germany, M. S. Greer, E. Holeman, K. Kadinsky-Cade, F. J. Rich, and W. Xu (2008), Seasonal, Kp, solar wind, and solar flux variations in long-term single-pass satellite estimates of electron and ion auroral hemispheric power, *J. Geophys. Res.*, 113, A06311, doi:10.1029/2007JA012866.

- Evans, D., and Greer, M. (2004). Polar Orbiting Environmental Satellite Space Environment Monitor-2: Instrument Descriptions and Archive Data Documentation. Technical Memorandum 93, NOAA, Boulder, Colorado OAR SEC 93, Version 1.4. January.
- Feldstein, Y. I., L. I. Gromova, A. E. Levitin, L. G. Blomberg, G. T. Marklund and P. A. Lindqvist (1996), To directly driven and loading-unloading processes during substorm. In *International Conference on Substorms*. Vol. 389, p. 69.
- Fejer B. G., M. C. Kelley, (1980). Ionospheric irregularities. *Reviews of Geophysics*, 18(2), 401-454.
- Fisher, G. and Kunches, J. (2011). Building resilience of the Global Positioning System to space weather. *Space Weather*, 9(12).
- Forte, B., and Radicella, S. M. (2002). Problems in data treatment for ionospheric scintillation measurements. *Radio Science*, 37(6).
- Foster, J. C. (1984), Ionospheric signatures of magnetospheric convection, *J. Geophys. Res.*, **89**, 855.
- Foster, J. C. (1989), Plasma transport through the dayside cleft: A source of ionization patches in the polar cap, in *Electromagnetic Coupling in the Polar Clefts and Caps*, edited by P. Sandholt, and A. Egeland, pp. 343–354, Kluwer Acad., Norwell, Mass.
- Fremouw, E. J., Leadabrand, R. L., Livingston, R. C., Cousins, M. D., Rino, C. L., Fair, B. C., & Long, R. A. (1978). Early results from the DNA Wideband satellite experiment—Complex-signal scintillation. *Radio Science*, 13(1), 167-187.
- Friis-Christensen, E., Lühr, H., & Hulot, G. (2006). Swarm: A constellation to study the Earth's magnetic field. *Earth, planets and space*, 58(4), 351-358.
- Ganushkina, N.Y., M.W. Liemohn, S. Dubyagin, I.A. Daglis, I. Dandouras, D.L. De Zeeuw, Y. Ebihara, R. Ilie, R. Katus, M. Kubyshkina, S.E. Milan, S. Ohtani, N. Ostgaard, J.P. Reistad, P. Tenfjord, F. Toffoletto, S. Zaharia, O. Amariutei (2015), Defining and resolving current systems in geospace. *Ann. Geophys.* 33, 1369–1402. doi: 10.5194/angeo-33-1369-2015
- Garner, T. W., R. B. Harris, J. A. York, C. S. Herbst, C. F. Minter III, and D. L. Hampton (2011), An auroral scintillation observation using precise, collocated GPS receivers, *Radio Sci.*, 46, RS1018, doi:10.1029/2010RS004412.
- Green, D. L., Waters, C. L., Anderson, B. J., & Korth, H. (2009). Seasonal and interplanetary magnetic field dependence of the field-aligned currents for both Northern and Southern Hemispheres. In *Annales Geophysicae* (Vol. 27, No. 4, pp. 1701-1715). Copernicus GmbH.
- Greenwald, R. A., Baker, K. B., Dudeney, J. R., Pinnock, M., Jones, T. B., Thomas, E. C., Villain, J. P., Cerisier, J. C., Senior, C., Hanuise, C., Hunsucker, R. D., Sofko, G., Koehler, J., Nielsen, E., Pellinen, R., Walker, A. D. M., Sato, N., and Yamagishi, H. (1995). Darn/superdarn. *Space Science Reviews*, 71(1-4), 761-796.
- Haaland, S. E., Paschmann, G., Förster, M., Quinn, J. M., Torbert, R. B., McIlwain, C. E., ... & Kletzing, C. A. (2007, February). High-latitude plasma convection from Cluster EDI measurements: method and IMF-dependence. In *Annales Geophysicae* (Vol. 25, No. 1, pp. 239-253).
- Hargreaves, J. K. (1992). *The solar-terrestrial environment: an introduction to geospace-the science of the terrestrial upper atmosphere, ionosphere, and magnetosphere*. Cambridge University Press, Cambridge, UK.

- Heppner, J. P., & Maynard, N. C. (1987). Empirical high-latitude electric field models. *Journal of Geophysical Research: Space Physics*, 92(A5), 4467-4489.
- Huang, C. S., J. C Foster, and M. C. Kelley, (2005). Long-duration penetration of the interplanetary electric field to the low-latitude ionosphere during the main phase of magnetic storms. *Journal of Geophysical Research: Space Physics*, 110(A11).
- Huang C. S., J. C. Foster, L. P. Goncharenko, P. J. Erickson, W. Rideout, and J. Coster, (2005). A strong positive phase of ionospheric storms observed by the Millstone Hill incoherent scatter radar and global GPS network. *J. Geophys. Res.* 110, A06303, doi:10.1029/2004JA010865.
- Hunsucker, R. D., and Hargreaves, J. K. (2002). *The High-Latitude Ionosphere and its Effects on Radio Propagation*. Cambridge, UK: Cambridge University Press, December 2002. 638.
- Iijima, T. (2000). Field-aligned currents in geospace: Substance and significance. *Magnetospheric Current Systems, Geophys. Monogr. Ser.*, 118, 107-129.
- Iijima, T., & Potemra, T. A. (1976a). The amplitude distribution of field-aligned currents at northern high latitudes observed by Triad. *Journal of Geophysical Research*, 81(13), 2165-2174.
- Iijima, T., & Potemra, T. A. (1976b). Field-aligned currents in the dayside cusp observed by Triad. *Journal of Geophysical Research*, 81(34), 5971-5979.
- Iijima, T., & Potemra, T. A. (1978). Large-scale characteristics of field-aligned currents associated with substorms. *Journal of Geophysical Research: Space Physics*, 83(A2), 599-615.
- Jakowski, N., Mayer, C., Hoque, M. M., & Wilken, V. (2011). Total electron content models and their use in ionosphere monitoring. *Radio Science*, 46(6).
- Jayachandran, P. T., Langley, R. B., MacDougall, J. W., Mushini, S. C., Pokhotelov, D., Hamza, A. M., Mann, I. R., Milling, D. K, Kale, Z. C., Chadwick, R., Kelly, T., Danskin, D. W., and Carrano, C. S. (2009). Canadian high arctic ionospheric network (CHAIN). *Radio Science*, 44(1), doi: 10.1029/2008RS004046.
- Jayachandran, P. T., Hamza, A. M., Hosokawa, K., Mezaoui, H., & Shiokawa, K. (2017). GPS amplitude and phase scintillation associated with polar cap auroral forms. *Journal of Atmospheric and Solar-Terrestrial Physics*, 164, 185-191.
- Jin, Y., J. I. Moen, and W. J. Miloch, (2015). On the collocation of the cusp aurora and the GPS phase scintillation: A statistical study. *Journal of Geophysical Research*, 120, 9176–9191. <https://doi.org/10.1002/2015JA021449>
- Kallenrode, M. B. (2013). Space physics: an introduction to plasmas and particles in the heliosphere and magnetospheres. *Springer Science & Business Media*.
- Kallio, E. I., T. I. Pulkkinen, H. E. J. Koskinen, A. Viljanen, J. A. Slavin, and K. Ogilvie (2000). Loading-unloading processes in the nightside ionosphere. *Geophysical Research Letters*, 27(11), 1627-1630.
- Kamide, Y. (1982). The relationship between field-aligned currents and the auroral electrojets: A review. *Space Science Reviews*, 31(2), 127-243.
- Kamide, Y., and Chian, A. C. L. (2007). *Handbook of the solar-terrestrial environment*. Springer Science & Business Media.

- Kamide, Y., and K. Kusano (2015), No major solar flares but the largest geomagnetic storm in the present solar cycle. *Space Weather*, 13 (6), 365–367, doi: [10.1002/2015SW001213](https://doi.org/10.1002/2015SW001213).
- Kelley, M. C., K. D. Baker, J. C. Ulwick, C. L. Rino, and M. J. Baron (1980). Simultaneous Rocket Probe, Scintillation, and Incoherent Scatter Radar Observations of Irregularities in the Auroral zone Ionosphere. *Radio Science* 15 (3), 491–505.
- Kelley, M. C. (1989). The Earth's Ionosphere, Int. *Geophys. Ser.*, 43, 71.
- Kelley, M. C. (2009). *The Earth's ionosphere: plasma physics and electrodynamics* (Vol. 96). Academic press.
- Kersley L., S. E. Pryse, and N. S. Wheadon (1988), Amplitude and phase scintillation at high latitudes over northern Europe, *Radio Sci.*, 23, 320–330, doi:10.1029/RS023i003p00320.
- Kikuchi, T., K. K. Hashimoto, and K. Nozaki, (2008). Penetration of magnetospheric electric fields to the equator during a geomagnetic storm. *Journal of Geophysical Research: Space Physics*, 113(A6).
- Kintner, P. M., Ledvina, B. M., & De Paula, E. R. (2007). GPS and ionospheric scintillations. *Space weather*, 5(9).
- Kintner, P. M., Humphreys, T., & Hinks, J. (2009). GNSS and ionospheric scintillation. *Inside GNSS*, 4(4), 22-30.
- Kivelson, M. G. and Russell, C. T., editors (1998). *Introduction to Space Physics*. Cambridge University Press, Cambridge, UK.
- Laundal, K. M., Cnossen, I., Milan, S. E., Haaland, S. E., Coxon, J., Pedatella, N. M., & Reistad, J. P. (2017). North–south asymmetries in earth's magnetic field. *Space Science Reviews*, 206(1-4), 225-257.
- Lastovicka J., (2002). Monitoring and forecasting of ionospheric space weather—effects of geomagnetic storms, *Journal of Atmospheric and Solar-Terrestrial Physics*, 64, Issues 5–6, 697-705, ISSN 1364-6826.
- Lepping, R. P., Acuña, M. H., Burlaga, L. F., Farrell, W. M., Slavin, J. A., Schatten, K. H., & Byrnes, J. B. (1995). The WIND magnetic field investigation. *Space Science Reviews*, 71(1-4), 207-229.
- Lepping, R. P., D. B. Berdichevsky, and C. C. Wu (2003). Sun-Earth Electrodynamics: The Solar Wind Connection. *Recent Res. Devel. Astrophys., Research Signpost*, 1, 139–171.
- Li, S.S., J. Liu, V. Angelopoulos, A. Runov, S. A. Kiehas (2014), Anti-Dipolarization Fronts Observed by ARTEMIS, *Journal of Geophysical Research: Space Phys*, 119, 7181–7198, doi:10.1002/2014JA020062.
- Liu, Y. D., H. Hu, R. Wang, Z. Yang, B. Zhu, Y. A. Liu, J. G. Luhmann and J. D. Richardson, (2015). Plasma and magnetic field characteristics of solar coronal mass ejections in relation to geomagnetic storm intensity and variability. *The Astrophysical Journal Letters*, 809(2), L34.
- Liu, J., W. Wang, A. Burns, X. Yue, S. Zhang, Y. Zhang, and C. Huang (2016), Profiles of ionospheric storm-enhanced density during the 17 March 2015 great storm. *Journal of Geophysical Research: Space Physics*, 121(1), 727-744, doi: [10.1002/2015JA021832](https://doi.org/10.1002/2015JA021832).

- Lockwood, M. and H. C. Carlson (1992). Production of polar cap electron density patches by transient magnetopause reconnection. *Geophysical Research Letters* 19 (17), 1731–1734.
- Low, B. C. (2001). Coronal Mass Ejections, Magnetic Flux Ropes, and Solar Magnetism. *Journal of Geophysical Research-Space Physics* 106 (A11), 25141–25163.
- Lui, A. T. Y. (1993), Inferring global characteristics of current sheet from local measurements. *Journal of Geophysical Research: Space Physics*, 98(A8), 13423-13427, doi: 10.1029/93JA01436.
- Lui, A. T. Y. (1996). Current disruption in the Earth's magnetosphere: Observations and models. *Journal of Geophysical Research: Space Physics*, 101(A6), 13067-13088.
- Lui, A. T. Y. and C. Z. Cheng (2001), Resonance frequency of stretched magnetic field lines based on a self-consistent equilibrium magnetosphere model. *Journal of Geophysical Research: Space Physics* 106.A11: 25793-25802.
- Lui, A. T. Y. (2011). Reduction of the cross-tail current during near-Earth dipolarization with multisatellite observations. *Journal of Geophysical Research: Space Physics*, 116(A12).
- Lysak, R. L. (1990). Electrodynamics coupling of the magnetosphere and ionosphere. *Space Science Reviews*, 52(1-2), 33-87.
- MacDougall J. W. (1990a). Distribution of irregularities in the northern polar region determined from HILAT observations, *Radio Sci.*, 25, 115–124, doi:10.1029/RS025i002p00115.
- MacDougall J. W. (1990b). The polar cap scintillation zone, *J. Geomag. Geoelectr.*, 42, 777–788.
- MacDougall, J. W., & Jayachandran, P. T. (2001). Polar cap convection relationships with solar wind. *Radio Science*, 36(6), 1869-1880.
- Mannucci, A. J., B. D. Wilson, and C. D. Edwards (1993), A new method for monitoring the Earth ionosphere total electron content using the GPS global network, paper presented at ION GPS-93, Inst. of Navig., Salt Lake City, Utah.
- Mansilla, G. A. (2018). Ionospheric Response to the Magnetic Storm of 22 June 2015. *Pure and Applied Geophysics*, 175(3), 1139-1153.
- Mathews, J. D. (1998). Sporadic E: current views and recent progress. *Journal of atmospheric and solar-terrestrial physics*, 60(4), 413-435.
- Mayaud, P. N. (1993). Derivation, meaning, and use of geomagnetic indices. *Geophysical Monograph, American Geophysical union*, 77, 22-22.
- McComas, D. J., Bame, S. J., Barker, P., Feldman, W. C., Phillips, J. L., Riley, P., & Griffee, J. W. (1998). Solar wind electron proton alpha monitor (SWEPAM) for the Advanced Composition Explorer. In *The Advanced Composition Explorer Mission* (pp. 563-612). Springer, Dordrecht.
- Mendillo, M. (2006). Storms in the ionosphere: Patterns and processes for total electron content. *Reviews of Geophysics*, 44(4).
- Meng, C. I., Holzworth, R. H., & Akasofu, S. I. (1977). Auroral circle: Delineating the poleward boundary of the quiet auroral belt. *Journal of Geophysical Research*, 82(1), 164-172.

- Merrill R. T., M. W. McElhinny, P. L. McFadden, (1998). *The magnetic field of the earth: paleomagnetism, the core, and the deep mantle*. Academic Press. San Diego, London, Boston, New York, Sydney, Tokyo, Toronto.
- Mikhailov A. V., and L. Perrone, (2014). A method for foF2 short-term (1–24 h) forecast using both historical and real-time foF2 observations over European stations: EUROMAP model, *Radio Science*, 49(4), 253-270.
- Mitchell C. N., L. Alfonsi, G. De Franceschi, M. Lester, V. Romano and A. W. Wernik, (2005). GPS TEC and scintillation measurements from the polar ionosphere during the October 2003 storm. *Geophysical Research Letters*, 32(12).
- Moen, J., H. C. Carlson, K. Oksavik, C. P. Nielsen, S. E. Pryse, H. R. Middleton, I. W. McCrea, and P. Gallop (2006). Eiscat observations of plasma patches at sub-auroral cusp latitudes. *Annales Geophysicae* 24 (9), 2363–2374.
- Moen, J., H. C. Carlson, Y. Rinne, and A. Skjaeveland (2012). Multi-Scale Features of Solar Terrestrial Coupling in the Cusp Ionosphere. *Journal of Atmospheric and Solar-Terrestrial Physics* 87-88 (SI), 11–19.
- Moen, J., K. Oksavik, L. Alfonsi, Y. Daabakk, V. Romano, and L. Spogli (2013), Space weather challenges of the polar cap ionosphere, *J. Space Weather Space Clim.*, 3, A02, doi:10.1051/swsc/2013025.
- Mushini, S. C., Jayachandran, P. T., Langley, R. B., MacDougall, J. W., & Pokhotelov, D. (2012). Improved amplitude-and phase-scintillation indices derived from wavelet detrended high-latitude GPS data. *GPS solutions*, 16(3), 363-373.
- Nagatsuma T., K. T. Murata, K. Yamamoto, T. Tsugawa, H. Kitauchi, T. Kondo, H. Ishibashi, M. Nishioka, and M. Okada (2014). Operation of a Data Acquisition, Transfer, and Storage System for the Global Space-Weather Observation Network. *Data Science Journal*, 13(0), PDA51-PDA56.
- Ogilvie, K. W., Chornay, D. J., Fritzenreiter, R. J., Hunsaker, F., Keller, J., Lobell, J., ... & Bodet, D. (1995). SWE, a comprehensive plasma instrument for the Wind spacecraft. *Space Science Reviews*, 71(1-4), 55-77.
- Ohtani, S., and T. Uozumi (2014), Nightside magnetospheric current circuit: Time constants of the solar wind-magnetosphere coupling. *Journal of Geophysical Research: Space Physics*, 119, 3558 – 3572, doi:10.1002/2013JA019680.
- Parker, E. N. (2003). *Dynamic sun*. Cambridge University Press.
- Parks, G. K. (1991). *Physics of Space Plasmas. An Introduction*. Addison-Wesley Publishing Company.
- Paschmann, G. (1991). Geomagnetism. In Jacobs, J. A. (Ed.), *The Magnetopause*. New York: Academic Press.
- Paxton, L. J., Meng, C. I., Fountain, G. H., Ogorzalek, B. S., Darlington, E. H., Gary, S. A., ... & Maynard, J. J. (1992). Special sensor ultraviolet spectrographic imager: An instrument description. In *Instrumentation for Planetary and Terrestrial Atmospheric Remote Sensing* (Vol. 1745, pp. 2-16). International Society for Optics and Photonics.

- Perreault, P., and Akasofu S.I. (1978). A study of geomagnetic storms, *Geophys. J. R. Astron. Soc.*, 54, 547–573.
- Pettigrew, E. D., S. G. Shepherd, and J. M. Ruohoniemi, (2010). Climatological patterns of high-latitude convection in the Northern and Southern hemispheres: Dipole tilt dependencies and interhemispheric comparisons, *J. Geophys. Res.*, 115, A07305, doi: 10.1029/2009JA014956.
- Phelps, A. D. R. and R. C. Sagalyn (1976). Plasma-Density Irregularities in High Latitude Top Side Ionosphere. *Journal of Geophysical Research-Space Physics* 81 (4), 515–523.
- Perrone L., G. De Franceschi, (1998). Solar, ionospheric and geomagnetic indices. *Annali di geofisica*, 41(5-6), 843-855.
- Piersanti, M., U. Villante, C. Waters, I. Coco, (2012), The 8 June 2000 ULF wave activity: A case study, *Journal of Geophysical Research: Space Physics*, 117(A2), doi: 10.1029/2011JA016857.
- Piersanti M., U. Villante (2016). On the discrimination between magnetospheric and ionospheric contributions on the ground manifestation of Sudden Impulses, *Journal of Geophysical Research: Space Physics*, 121(7), 6674-6691, doi: 10.1002/2015JA021666.
- Piersanti, M., Alberti, T., Bemporad, A., Berrilli, F., Bruno, R., Capparelli, V., ... and Del Corpo, A. (2017). Comprehensive Analysis of the Geoeffective Solar Event of 21 June 2015: Effects on the Magnetosphere, Plasmasphere, and Ionosphere Systems. *Solar Physics*, 292(11), 169.
- Pietrella, M., & Bianchi, C. (2009). Occurrence of sporadic-E layer over the ionospheric station of Rome: analysis of data for thirty-two years. *Advances in space research*, 44(1), 72-81.
- Pizzicaroli, J. C. (1998). Launching and building the Iridium® constellation. In *Mission Design & Implementation of Satellite Constellations* (pp. 113-121). Springer, Dordrecht.
- Ponomarenko, P. V., & Waters, C. L. (2006). Spectral width of SuperDARN echoes: measurement, use and physical interpretation. In *Annales Geophysicae* (Vol. 24, No. 1, pp. 115-128).
- Ponomarenko, P. V., Waters, C. L., & Menk, F. W. (2007). Factors determining spectral width of HF echoes from high latitudes. In *Annales Geophysicae* (Vol. 25, No. 3, pp. 675-687).
- Prikryl P., P. T., Jayachandran, S. C. Mushini, and R. Chadwick, (2011). Climatology of GPS phase scintillation and HF radar backscatter for the high-latitude ionosphere under solar minimum conditions. *Annales Geophysicae*, 29(2), 377-392, Copernicus GmbH.
- Prikryl, P., Spogli, L., Jayachandran, P. T., Kinrade, J., Mitchell, C. N., Ning, B., ... and Opperman, B. D. L (2011). Interhemispheric comparison of GPS phase scintillation at high latitudes during the magnetic-cloud-induced geomagnetic storm of 5–7 April 2010. In *Annales Geophysicae*, 29, 2287–2304.
- Prikryl, P., P. T. Jayachandran, S. C. Mushini and I. G. Richardson, (2012). Toward the probabilistic forecasting of high-latitude GPS phase scintillation. *Space Weather*, 10(8).
- Prikryl, P., Zhang, Y., Ebihara, Y., Ghoddousi-Fard, R., Jayachandran, P. T., Kinrade, J., C. N. Mitchell, A. T. Weatherwax, G. Bust, P. J. Cilliers, L. Spogli, L. Alfonsi, V. Romano, B. Ning, G. Li, M. J. Jarvis, D. W. Danskin, E. Spanswick, E. Donovan and M. Terkildsen, (2013). An interhemispheric comparison of GPS phase scintillation with auroral emission observed at the South Pole and from the DMSP satellite. *Annals of Geophysics*, 56(2), R0216.

- Prikryl, P., Jayachandran, P. T., Mushini, S. C., & Richardson, I. G. (2014). High-latitude GPS phase scintillation and cycle slips during high-speed solar wind streams and interplanetary coronal mass ejections: a superposed epoch analysis. *Earth, Planets and Space*, 66(1), 62.
- Prikryl, P., Ghoddousi-Fard, R., Spogli, L., Mitchell, C. N., Li, G., Ning, B., ... and Weatherwax, A. T (2015). GPS phase scintillation at high latitudes during geomagnetic storms of 7–17 March 2012–Part 2: Interhemispheric comparison. In *Annales Geophysicae*, 33, 657–670.
- Proelss, G. (2004). *Physics of the Earth's Space Environment: an Introduction*. Berlin Heidelberg: Springer
- Richmond, A. (1987) *The ionosphere*. Chapter 7 in: S.-I. Akasofu and Y. Kamide (Eds.), *The Solar Wind and the Earth*, Terra Sci. Publ. Co., Tokyo, Japan, pp. 123-140.
- Rino, C. L., E. J. Fremouw (1977), The angle dependence of singly scattered wave fields, *J. Atmos. Terr. Phys.*, 39, 859.
- Rino, C. L. (1979a). A power law phase screen model for ionospheric scintillation: 1. Weak scatter. *Radio Science*, 14(6), 1135-1145.
- Rino, C. L. (1979b). A power law phase screen model for ionospheric scintillation: 2. Strong scatter. *Radio Science*, 14(6), 1147-1155.
- Rishbeth H. (1990): A greenhouse effect in the ionosphere?, *Planet. Space Sci.*, 38, 945-948.
- Rishbeth H. and R.G. Roble (1992): Cooling of the upper atmosphere by enhanced greenhouse gases–Modelling of the thermospheric and ionospheric effects, *Planet. Space Sci.*, 40, 1011-1026.
- Rodger, A. S., M. Pinnock, J. R. Dudeney, K. B. Baker, and R. A. Greenwald (1994). A New Mechanism for Polar Patch Formation. *Journal of Geophysical Research-Space Physics* 99 (A4), 6425–6436.
- Rostoker, G., and T. Eastman, (1987), A boundary layer model for magnetospheric substorms. *Journal of Geophysical Research: Space Physics*, 92.A11: 12187-12201.
- Ruohoniemi, J. M., and R. A. Greenwald, (2005), Dependencies of high-latitude plasma convection: Consideration of interplanetary magnetic field, seasonal, and universal time factors in statistical patterns. *Journal of Geophysical Research: Space Physics*, 110(A9).
- Russell C. T. (1986). *Solar wind control of magnetospheric configuration*. Solar Wind-Magnetosphere Coupling, **209**.
- Sandholt, P. E., H. C. Carlson, and A. Egeland (2002). *Dayside and Polar Cap Aurora*. Dordrecht: Kluwer Academic Publishers.
- Sato, T. (1959), Morphology of ionospheric F2 disturbances in the polar regions, A linkage between polar patches and plasmaspheric drainage plumes, *Rep. Ionos. Res. Space Res. Jpn.*, **131**, 91.
- Schmid, D., M. Volwerk, R. Nakamura, W. Baumjohann and M. Heyn (2011), A statistical and event study of magnetotail dipolarization fronts. In *Annales Geophysicae* (Vol. 29, No. 9, pp. 1537-1547). Copernicus GmbH.
- Schrijver, C. J., & Zwaan, C. (2008). *Solar and stellar magnetic activity* (Vol. 34). Cambridge University Press.

- Schunk, R. W. & Nagy A. F. (2009). *Ionospheres Physics, Plasma Physics, and Chemistry*. Second Edition. Cambridge: Cambridge University Press.
- Secan J. A., R. M. Bussey, E. J. Fremouw, and S. Basu (1997), Highlatitude upgrade to the Wideband ionospheric scintillation model, *Radio Sci.*, 32, 1567–1574, doi: 10.1029/97RS00453.
- Shue, J. H., Song, P., Russell, C. T., Steinberg, J. T., Chao, J. K., Zastenker, G., ... & Kawano, H. (1998). Magnetopause location under extreme solar wind conditions. *Journal of Geophysical Research: Space Physics*, 103(A8), 17691-17700.
- Sieradzki R., (2015). An analysis of selected aspects of irregularities oval monitoring using GNSS observations, *Journal of Atmospheric and Solar-Terrestrial Physics*, 129, 87-98, ISSN 1364-6826.
- Singer, H., Matheson, L., Grubb, R., Newman, A., & Bouwer, D. (1996). Monitoring space weather with the GOES magnetometers. In *GOES-8 and Beyond* (Vol. 2812, pp. 299-309). International Society for Optics and Photonics.
- Singh A. K., Devendraa Siingh, R. P. Singh, (2010). Space Weather: Physics, Effects and Predictability, *Surv Geophys*, 31, 581–638, doi: 10.1007/s10712-010-9103-1.
- Smith, C. W., L'Heureux, J., Ness, N. F., Acuna, M. H., Burlaga, L. F., & Scheifele, J. (1998). The ACE magnetic fields experiment. In *The Advanced Composition Explorer Mission* (pp. 613-632). Springer, Dordrecht.
- Smith, A. M., Mitchell, C. N., Watson, R. J., Meggs, R. W., Kintner, P. M., Kauristie, K., & Honary, F. (2008). GPS scintillation in the high arctic associated with an auroral arc. *Space Weather*, 6(3).
- Sojka J.J., M .D. Bowlin, R . W. Schunk, D. T. Decker, C. E. Valladares, R. Sheehan, D. N. Anderson and R . A. Heelis, (1993). Modeling Polar Cap F-Region Patches Using Time Varying Convection, *Geophysical Research Letters*, 20(17), 1783-1786.
- Sonnerup, B. U. O. (1985). Solar Wind Interaction with Planetary Magnetic Fields. *ESA Future Missions in Solar, Heliospheric and Plasma*, 53–64.
- Spogli, L., Alfonsi, L., De Franceschi, G., Romano, V., Aquino, M. H. O., & Dodson, A. (2009). Climatology of GPS ionospheric scintillations over high and mid-latitude European regions. In *Annales Geophysicae*. EGU.
- Spogli L., L. Alfonsi, P. J. Cilliers, E. Correia, G. De Franceschi, C. N. Mitchell, V. Romano, J. Kinrade, and M. A. Cabrera, (2013a). GPS scintillations and total electron content climatology in the southern low, middle and high latitude regions. *Annals of Geophysics*, 56(2), R0220.
- Spogli, L., Alfonsi, L., Romano, V., De Franceschi, G., Francisco, G. M. J., Shimabukuro, M. H., ... & Aquino, M. (2013b). Assessing the GNSS scintillation climate over Brazil under increasing solar activity. *Journal of Atmospheric and Solar-Terrestrial Physics*, 105, 199-206.
- Stix, M. (2004). *The Sun: An Introduction Second Edition*. Heidelberg: Springer.
- Svalgaard, L. (1977). *Geomagnetic Activity: Dependence on Solar Wind Parameters* (No. SU-IPR-699). STANFORD UNIV CALIF INST FOR PLASMA RESEARCH.
- Tassev Y., Velinov P.I.Y., Tomova D., Mateev L. (2017). Analysis of extreme solar activity in early September 2017: G4 – severe geomagnetic storm (07÷08.09) and GLE72 (10.09) in solar minimum. *Comptes rendus de l'Académie bulgare des Sciences*, Vol 70, No10, pp.1437-1444.

- Tidman, D. A., and Krall, N. A. (1971). *Shock waves in collisionless plasmas* (pp. 99-112). New York: Wiley-Interscience.
- Tiwari S., A. Jain, S. Sarkar, S. Jain and A. K. Gwal, (2012). Ionospheric irregularities at Antarctic using GPS measurements. *Journal of earth system science*, 121(2), 345-353.
- Troshichev, O. A., & Andrezen, V. G. (1985). The relationship between interplanetary quantities and magnetic activity in the southern polar cap. *Planetary and space science*, 33(4), 415-419.
- Tsagouri I., A. Belehaki, N. Bergeot, C. Cid, V. Delouille, T. Egorova, N. Jakowski, I. Kutiev, A. Mikhailov, M. Nùñez, M. Pietrella, A. Potapov, R. Qahwaji, Y. Tulunay, P. Velinov, and A. Viljanen, (2013). Progress in space weather modeling in an operational environment. *Journal of Space Weather and Space Climate*, 3, A17.
- Tsunoda, R. T. (1988). High-Latitude F-Region Irregularities - A Review and Synthesis. *Reviews of Geophysics* 26 (4), 719–760.
- Tsyganenko, N. A. and M. I. Sitnov (2005), Modeling the dynamics of the inner magnetosphere during strong geomagnetic storms. *Journal of Geophysical Research: Space Physics*, 110(A3), doi: 10.1029/2004JA010798.
- Turner, N. E., D. N. Baker, T. I. Pulkkinen and R. L. McPherron, (2000). Evaluation of the tail current contribution to dst. *Journal of Geophysical Research A: Space Physics*, 105(A3), 5431-5439. doi:10.1029/1999JA000248.
- Van Dierendonck, A. J., J. Klobuchar and Q. Hua, (1993). Ionospheric scintillation monitoring using commercial single frequency C/A code receivers. *In proceedings of ION GPS*, 93, 1333-1342.
- Vanlommel P., and R. Van der Linden (2017). STCE Newsletter 4 Sep 2017 – 10 Sep 2017, Published by the Solar-Terrestrial Centre of Excellence (STCE), issue: 15 Sep 2017. Available online at <http://www.stce.be/newsletter/>.
- Venkatesh Babu M. N., K. Lakshmi Narayana (2012). Implementation of the modernized GPS signals L2C, L5 and their tracking strategies. *International Journal of Engineering Research and Applications (IJERA)* ISSN: 2248-9622 www.ijera.com Vol. 2, Issue4, July-august 2012, pp.2148-2152.
- Villante U., M. Piersanti, P. Di Giuseppe, M. Vellante, T.L. Zhang, W. Magnes (2005), Sudden commencement event of 17 April 2002: Aspects of the geomagnetic response at low latitudes, *Journal of Geophysical Research: Space Physics*, 110, A12, doi: 10.1029/2004JA010978.
- Villante, U. and M. Piersanti (2008), An analysis of sudden impulses at geosynchronous orbit. *Journal of Geophysical Research: Space Physics*, 113(A8), doi: 10.1029/2008JA013028.
- Villante, U. and M. Piersanti (2009), An analysis of sudden impulses at low latitude. *Journal of Geophysical Research: Space Physics*, 114(A6), doi: 10.1029/2008JA013920.
- Villante, U., & Piersanti, M. (2014). On the propagation of sudden impulses through the magnetosphere. *Journal of Atmospheric and Solar-Terrestrial Physics*, 115, 2-6.
- Weber, E. J., J. Buchau, J. G. Moore, J. R. Sharber, R. C. Livingston, J. D. Winningham, and B. W. Reinisch (1984), F layer ionization patches in the polar cap, *J. Geophys. Res.*, 89(A3), 1683–1694, doi:10.1029/JA089iA03p01683.

- Weber, E. J., R. T. Tsunoda, J. Buchau, R. E. Sheehan, D. J. Strickland, W. Whiting, and J. G. Moore (1985), Coordinated measurements of auroral zone plasma enhancements, *J. Geophys. Res.*, *90*(A7), 6497–6513, doi:10.1029/JA090iA07p06497.
- Weber, E. J., J. A. Klobuchar, J. Buchau, H. C. Carlson, R. C. Livingston, O. Delabaujardiere, M. Mccready, J. G. Moore, and G. J. Bishop (1986), Polar cap F layer patches: Structure and dynamics, *J. Geophys. Res.*, *91*(A11), 12,121–12,129, doi:10.1029/JA091iA11p12121.
- Weimer, D. R. (1995). Models of high-latitude electric potentials derived with a least error fit of spherical harmonic coefficients. *Journal of Geophysical Research: Space Physics* *100* (A10), 19595–19607.
- Weimer, D. R. (2005). Improved ionospheric electrodynamic models and application to calculating Joule heating rates. *Journal of Geophysical Research: Space Physics*, *110*(A5)
- Wernik, A. W., Secan, J. A., & Fremouw, E. J. (2003). Ionospheric irregularities and scintillation. *Advances in Space Research*, *31*(4), 971-981.
- Wernik, A. W., Alfonsi, L., & Materassi, M. (2004). Ionospheric irregularities, scintillation and its effect on systems. *Acta geophysica polonica*, *52*(2), 237-249.
- Whitehead, J. D. (1961). The formation of the sporadic-E layer in the temperate zones. *Journal of Atmospheric and Terrestrial Physics*, *20*(1), 49-58.
- Whitney, H. E., & Basu, S. (1977). The effect of ionospheric scintillation on VHF/UHF satellite communications. *Radio Science*, *12*(1), 123-133.
- Woodfield, E. E., Hosokawa, K., Milan, S. E., Sato, N., and Lester, M. (2002). An interhemispheric, statistical study of nightside spectral width distributions from coherent HF scatter radars. *Annales Geophysicae*, *20*(12), 1921-1934.
- Wu, C. C., K. Liou, R. P. Lepping, L. Hutting, S. Plunkett, R. A. Howard and D. Socker, (2016), The first super geomagnetic storm of solar cycle 24: “The St. Patrick’s day event (17 March 2015)”. *Earth, Planets and Space*, *68*(1), 151.
- Yeh, K. C., and Liu, C. H. (1982). Radio wave scintillations in the ionosphere. *Proceedings of the IEEE*, *70*(4), 324-360.
- Yeh, K. C., and A. W. Wernik (1993), On ionospheric scintillation, in *Wave Propagation in Random Media (Scintillation)*, edited by V. I. Tatarski et al., pp. 34–49, Int. Soc. for Opt. Eng., Bellingham, Wash.
- Zhu, L., Schunk, R. W., Eccles, V., Scherliess, L., Sojka, J. J., & Gardner, L. (2017). Terminator field-aligned current system: Its dependencies on solar, seasonal, and geomagnetic conditions. *Journal of Atmospheric and Solar-Terrestrial Physics*, *164*, 10-17.
- Zou, Y. and D. Wang (2009), A study of GPS ionospheric scintillations observed at Guilin. *Journal of Atmospheric and Solar-Terrestrial Physics*, *71*(17), 1948-1958.